

WIRELESS POWER TRANSFER WITH BIDIRECTIONAL TELEMTRY FOR
ACTIVE IMPLANTABLE MEDICAL DEVICES

A THESIS SUBMITTED TO
THE GRADUATE SCHOOL OF NATURAL AND APPLIED SCIENCES
OF
MIDDLE EAST TECHNICAL UNIVERSITY

ONUR AVAN

IN PARTIAL FULFILLMENT OF THE REQUIREMENTS
FOR
THE DEGREE OF MASTER OF SCIENCE
IN
ELECTRICAL AND ELECTRONICS ENGINEERING

OCTOBER 2017

Approval of the thesis:

**WIRELESS POWER TRANSFER WITH BIDIRECTIONAL TELEMETRY FOR
ACTIVE IMPLANTABLE MEDICAL DEVICES**

submitted by **ONUR AVAN** in partial fulfillment of the requirements for the degree of
**Master of Science in Electrical and Electronics Engineering Department, Middle
East Technical University** by,

Prof. Dr. Gülbin Dural Ünver

Dean, Graduate School of **Natural and Applied Sciences**

Prof. Dr. Tolga Çiloğlu

Head of Department, **Electrical and Electronics Engineering**

Prof. Dr. Nevzat Güneri Gençer

Supervisor, **Electrical and Electronics Eng. Dept., METU**

Examining Committee Members:

Prof. Dr. Murat Eyüboğlu

Electrical and Electronics Engineering Department, METU

Prof. Dr. Nevzat Güneri Gençer

Electrical and Electronics Engineering Department, METU

Prof. Dr. Ahmet Hava

Electrical and Electronics Engineering Department, METU

Assoc. Prof. Dr. Yeşim Serinağaoğlu Doğrusöz

Electrical and Electronics Engineering Department, METU

Prof. Dr. Yusuf Ziya İder

Electrical and Electronics Eng. Dept., Bilkent University

Date:

02/10/2017

I hereby declare that all information in this document has been obtained and presented in accordance with academic rules and ethical conduct. I also declare that, as required by these rules and conduct, I have fully cited and referenced all material and results that are not original to this work.

Name, Last Name: ONUR AVAN

Signature :

ABSTRACT

WIRELESS POWER TRANSFER WITH BIDIRECTIONAL TELEMETRY FOR ACTIVE IMPLANTABLE MEDICAL DEVICES

AVAN, ONUR

M.S., Department of Electrical and Electronics Engineering

Supervisor : Prof. Dr. Nevzat Güneri Gençer

October 2017, 99 pages

This thesis presents a wireless power transfer (WPT) system for powering implantable medical devices (IMDs). In order to make IMDs smaller and longer life devices primary batteries are replaced with rechargeable ones for the last two decades. Consequently, WPT systems are implemented for IMD's. Electromagnetic induction is the most preferred and safety proven method among existing WPT methods. However, loose coupling inherent in these systems limits the implant depth and increases the battery recharge time. A multi-coil approach (Strongly Coupled Magnetic Resonance) using Litz wire is implemented in this work to increase the power transfer efficiency and to alter problems defined in the traditional methods. 1 MHz operation frequency is selected by analyzing AC resistance of Litz wire types to achieve high quality factor coils and also by analyzing dielectric and conductivity losses in tissue. To take control over WPT and communicate with the device, a half-duplex bidirectional telemetry system is designed. In the design procedure, first, WPT system is modeled analytically and then optimized in MATLAB platform. The results are veri-

fied numerically in COMSOL Multiphysics program. A frequency control method is demonstrated by using a switch capacitor array at the power amplifier side to adapt the system to different implant depths. In the telemetry part, ASK modulation is used for both forward and backward communication with low modulation depth without disturbing the received power at the implant side. Modulator and demodulator circuit designs are simulated using LT Spice software. PCB design for the hardware of both implantable device and the external charger device is performed in Altium CAD platform. 58 % (DC/DC) power transfer efficiency is achieved to transfer 485 mW power at 4 cm implant depth. A Manchester encoded half-duplex bidirectional telemetry system with 19200 baud rate is also established.

Keywords: Wireless Power Transfer, Near Field Communication, Medical Implants

ÖZ

VÜCÜT İÇERİSİNE YERLEŞTİRİLEBİLEN MEDİKAL CİHAZLAR İÇİN KABLOSUZ GÜÇ AKTARIMI VE ÇİFT YÖNLÜ HABERLEŞME

AVAN, ONUR

Yüksek Lisans, Elektrik ve Elektronik Mühendisliği Bölümü

Tez Yöneticisi : Prof. Dr. Nevzat Güneri Gençer

Ekim 2017 , 99 sayfa

Bu tezde vücut içerisine yerleştirilebilir medikal cihazlar için bir kablosuz güç aktarım sistemi sunulmuştur. Son 20 yıldır, daha küçük ve uzun ömürlü cihazlar yapmak amacıyla tekrar şarj edilemeyen bataryalar tekrar şarj edilebilir olanlar ile değiştirilmeye başlanmıştır. Bu değişimin bir sonucu olarak kablosuz güç aktarım sistemleri bu cihazlarda uygulanmıştır. Elektromanyetik indüksiyon yöntemi diğer yöntemler arasında en çok tercih edilen ve güvenliği kanıtlanmış olan yöntemdir. Ancak, bu sistemlerdeki düşük manyetik bağlanma katsayısı cihazların vücut içerisine yerleştirilme derinliğini sınırlandırmış ve bataryanın tekrar şarj edilme süresini uzatmıştır. Bu çalışmada, çoklu bobin kullanım yaklaşımı (Güçlü Bağlantılı Manyetik Resonans) Litz kablo tipi kullanılarak uygulanmıştır. Bu yaklaşımla hedeflenen güç aktarım verimliliğini arttırmak ve geleneksel methodlarda görülen problemleri çözmektir. Sistem maksimum çalışma frekansı olarak 1 MHz seçilmiştir. Frekans seçimi için yüksek kalite faktörüne sahip bobin tasarlamak için kullanılan Litz kablonun değişken akım-

daki resistansı analiz edilmiş ve seçilen frekansın doku üzerindeki iletkenlik ve yalıtkanlık güç kayıpları incelenmiştir. Kablosuz güç aktarımını kontrol etmek ve medikal cihaz ile haberleşebilmek amacıyla yarı çift yönlü bir telemetri sistemi tasarlanmıştır. Kablosuz güç aktarım sistemi tasarım sürecinde önce analitik sistem modellemesi yapılmış sonra model MATLAB platformu üzerinde optimize edilmiştir. Elde edilen sonuçlar daha sonra COMSOL programında doğrulanmıştır. Sistemin farklı vücut derinliklerinde aynı performansı göstermesi için frekans kontrolü uygulanmıştır. Verici kısımda kullanılan güç yükselticiyi yeni frekansa uyumlu hale getirmek için kondansatör anahtarlama metodu kullanılmıştır. Yakın mesafe haberleşmesinde genlik kaydırma yöntemi hem ileri hem de geri telemetride düşük sinyal geçişleri ile implement edilmiştir. Buradaki amaç, haberleşme sırasında alıcı voltaj seviyesinin düşmesini engellemektir. Telemetri için tasarlanan devre yapılarının simülasyonu LT Spice programında yapılmıştır. Vücut içerisine yerleştirilebilir medikal cihaz ve harici şarj cihazının elektronik kart tasarımı Altium CAD programında yapılmıştır. Medikal cihaza 4 cm mesafede 485 mW güç aktarılırken % 58 (DC/DC) verimliliğe ulaşılmıştır. Manchester kodlanmış yarı çift yönlü telemetri sisteminde ise 19200 veri iletim hızına erişilmiştir.

Anahtar Kelimeler: Kablosuz Güç Aktarımı, Yakın Mesafe Haberleşmesi, Vücut İçerisine Yerleştirilebilir Medikal Cihazlar

to Sinem and My Family

ACKNOWLEDGMENTS

First of all, I would like to express my gratitude to my supervisor Prof. Dr. Nevzat G. Gençer due to the entire support and invaluable help. It would be much harder for me to achieve desired results without his guidance, positive motivation and patience on my disordered working scheme.

I would like to express my special thanks to Mr. Balkar Erdoğan for his generous support and encouragement. He was there at any problem I faced during the work and spent lots of time with me to share his experience and overcome difficulties.

I would also like to thank to all Bioelectromagnetic Research Group Members for helping me at anything that I need during working on the laboratory.

The starting point of the thesis was the Medically Implantable Neurostimulator Project conducted by METU-EEE and Kardiosis Ltd. which is funded by the Scientific and Technological Research Council of Turkey (TUBITAK). Therefore I would like to thank to all the participants for giving me the chance of working at that project.

TABLE OF CONTENTS

ABSTRACT	v
ÖZ	vii
ACKNOWLEDGMENTS	x
TABLE OF CONTENTS	xi
LIST OF TABLES	xv
LIST OF FIGURES	xvi
LIST OF ABBREVIATIONS	xxii

CHAPTERS

1	INTRODUCTION	1
1.1	Scope of Thesis	2
1.2	Literature Review	2
1.2.1	Ultrasonic Energy Transfer	2
1.2.2	Capacitive Coupling	3
1.2.3	Magnetic Coupling	3
1.2.3.1	Mid-Field and Far-Field Electromagnetic Coupling	3
1.2.3.2	Near-Field Inductive Coupling	4

1.3	Thesis Organization	5
2	WIRELESS POWER TRANSFER VIA ELECTROMAGNETIC INDUCTION	7
2.1	Theory	7
2.1.1	Resonant Wireless Power Transfer	11
2.1.1.1	Resonant Structures	12
2.2	Strongly Coupled Magnetic Resonance	14
2.2.1	Frequency Splitting Phenomenon on SCMR	17
2.3	Coil Design	18
2.4	Coupling Between Coils	20
2.5	AC Resistance of a Coil	20
2.5.1	Litz Wire	21
2.5.1.1	Method 1	21
2.5.1.2	Method 2	22
2.5.1.3	Results of AC Resistance Modelling Methods	23
3	POWER AMPLIFIER AND RECTIFIER DESIGN	25
3.1	Power Amplifier Design	25
3.1.1	Class_E Power Amplifier	26
3.1.2	Class-E Amplifier Optimal Design	28
3.1.3	Class-E Amplifier Design Results	29
3.2	Rectifier Design	31

	3.2.1	Rectifier Design Result	33
4		WPT DESIGN	37
	4.1	Receiver Voltage and Current Requirement Analysis	42
	4.2	Adaptive System Operation	43
	4.2.1	Amplifier Feedback Design	47
	4.3	Numerical Analysis Results	52
5		NEAR FIELD COMMUNICATION	57
	5.1	Modulator Design	59
	5.2	Demodulator Design	60
6		EXPERIMENTAL RESULTS	67
	6.1	Experimental Setup	68
	6.2	Coil Parameters	69
	6.3	WPT Power Efficiency Results	70
	6.4	Near Field Communication Results	71
	6.4.1	Forward Telemetry Results	71
	6.4.2	Backward Telemetry Results	76
7		CONCLUSION	81
		REFERENCES	83
		APPENDICES	86
	A	LITZ WIRE POWER LOSS CALCULATION	87
	B	MAGNETIC FIELD CALCULATION ON COIL ITSELF	89

C	EXTERNAL CHARGER DEVICE SCHEMATICS	93
D	IMPLANTABLE MEDICAL DEVICE SCHEMATICS	97

LIST OF TABLES

TABLES

Table 3.1	Parameters of designed class-E amplifier	29
Table 4.1	Litz wire types and corresponding parameters	41
Table 4.2	Optimization parameters	41
Table 6.1	Inductance comparison of the coils	69
Table 6.2	AC Resistance comparison of the coils at 1 MHz frequency	70
Table 6.3	Efficiency of the system blocks expected by design results	70
Table 6.4	Experimental results of overall wireless power transfer efficiency	70

LIST OF FIGURES

FIGURES

Figure 1.1 System Blocks	5
Figure 2.1 Mutual inductance M_{21} by the coupling of two coils via a partial magnetic flow	8
Figure 2.2 Equivalent circuit for magnetically coupled coils. L_1 and L_2 refers to the inductance of transmitter and receiver coils respectively, R_2 is internal resistance of receiver coil, R_L is load resistance and v_2 is voltage on the load resistance.	9
Figure 2.3 Equivalent circuit diagram of transmitter under mutual coupling. L_1 is transmitter coil inductance, R_1 its internal resistance and Z_{ref} is reflected impedance from receiver, i_1 is current passing through the coil and v_1 is voltage across the coil.	10
Figure 2.4 Basic circuit structure for resonant wireless power transfer system. L_1, L_2 transmitter and receiver coil inductances respectively, C_1, C_2 corresponding series tuning capacitors, M mutual inductance between coils.	12
Figure 2.5 Circuit models : (a) series-series resonant , (b) series-parallel resonant , (c) parallel-parallel resonant , (d) parallel-series resonant	13
Figure 2.6 Strongly Coupled Magnetic Resonance System Architecture	14
Figure 2.7 S_{21} magnitude as a function of frequency and coupling coefficient k_{23} [1]	18

Figure 2.8 Geometric arrangement and notation for primary and secondary coils composed of concentric circular loops. a_i and b_i are coil radii of the corresponding turns, d is distance between coils, p is distance between axes, N_a and N_b are turn counts of the corresponding coils	19
Figure 2.9 External and Internal magnetic field on a single turn where r_c is conductor radius and r is position of the strand in conductor (Litz wire) [2]	21
Figure 2.10 AC Resistance vs Frequency for designed transmitter coil	23
Figure 2.11 AC Resistance vs Frequency for designed receiver coil	24
Figure 3.1 Ideal transistor voltage and current waveforms for class-E amplifier	26
Figure 3.2 Schematic of class-E power amplifier	27
Figure 3.3 Class-E amplifier V_{DS} , I_D graphs as a function of time for different load resistances [3]	29
Figure 3.4 Class-E amplifier schematic on LT Spice	30
Figure 3.5 Zero voltage/Zero current switching behaviour	30
Figure 3.6 Almost pure coil current with 1MHz frequency	31
Figure 3.7 ZVS Class-E rectifier	32
Figure 3.8 Class-D synchronous rectifier	32
Figure 3.9 Full bridge rectifier	33
Figure 3.10 Designed rectifier schematic	34
Figure 3.11 Rectifier diode current	35
Figure 3.12 Current on the load coil after rectification	35
Figure 4.1 Wireless power transfer design procedure	38
Figure 4.2 Tissue conductivities vs frequency	39

Figure 4.3	Tissue relative permittivity vs frequency	39
Figure 4.4	Coupling coefficient k for different coil radiuses at 4 cm distance	40
Figure 4.5	Efficiency with frequency and Z_{43}	42
Figure 4.6	Efficiency versus distance graph for the 4 coil system	43
Figure 4.7	Z_{21} versus distance graph for the 4 coil system	44
Figure 4.8	Z_{21} versus distance graph for 3-coil system	46
Figure 4.9	Efficiency versus distance graph for 3-coil system	46
Figure 4.10	Z_{21} versus distance graph for 3-coil system	47
Figure 4.11	3-Coil design results at 1 cm	48
Figure 4.12	3-Coil design results at 2 cm	49
Figure 4.13	3-Coil design results at 3 cm	50
Figure 4.14	Zero voltage switching detection	51
Figure 4.15	Circuit for estimating the transmitter coil current	52
Figure 4.16	Simulation model with air between coils	53
Figure 4.17	Magnetic Flux distribution with air between coils	53
Figure 4.18	Simulation model with tissue	54
Figure 4.19	Magnetic Flux distribution with tissue between coils	54
Figure 5.1	Binary Encoding and Manchester Encoding Schemes for the corresponding bit stream	58
Figure 5.2	Modulator design at the transmitter side	60
Figure 5.3	Modulator design at the receiver side	61
Figure 5.4	Demodulator circuit design	61

Figure 5.5 Schematic of the complete system designed in LT Spice	62
Figure 5.6 Modulated signals on external charger and implant side	63
Figure 5.7 Modulation signal from external charger and Demodulated signal at the Implant side	64
Figure 5.8 Modulation signal from Implant side and Demodulated signal at the external charger side	65
Figure 6.1 Wound coils of WPT system. On left side transmitter coil, on middle receiver coil and on right side load coil	67
Figure 6.2 Manufactured PCB's for the WPT system. External Charger is on the left and receiver electronics of IMD is on the right	68
Figure 6.3 Experimental Setup for the system at 4 cm transfer depth	69
Figure 6.4 Forward Telemetry at 2 cm depth: Yellow trace shows the data modulation signal sent from the external charger side. Green trace shows the variation of the demodulator input signal at the IMD side.	72
Figure 6.5 Forward Telemetry at 2 cm depth: Yellow trace shows the data modulation signal sent from the external charger side. Green trace shows the low pass filtered output of the peak detector at the IMD side.	72
Figure 6.6 Forward Telemetry at 2 cm depth: Yellow trace shows the data modulation signal sent from the external charger side. Green trace shows the high pass filtered signal before amplifier stage at the IMD side.	73
Figure 6.7 Forward Telemetry at 2 cm depth: Yellow trace shows the data modulation signal sent from the external charger side. Green trace shows the amplified signal before inverting comparator at the IMD side.	73
Figure 6.8 Forward Telemetry at 2 cm depth: Yellow trace shows the data modulation signal sent from the external charger side. Green trace shows the demodulated signal at the IMD side.	74

Figure 6.9 Forward Telemetry at 2 cm depth: Yellow trace shows the data modulation signal sent from the external charger side. Green trace shows the rectified voltage variation at the IMD side during data transfer.	74
Figure 6.10 Forward Telemetry at 1 cm depth: Yellow trace shows the data modulation signal sent from the external charger side. Green trace shows the variation of demodulator input signal at the IMD side.	75
Figure 6.11 Forward Telemetry at 4 cm depth: Yellow trace shows the data modulation signal sent from the external charger side. Green trace shows the variation of demodulator input signal at the IMD side.	75
Figure 6.12 Backward Telemetry at 2 cm depth: Green trace shows the data modulation signal sent from the IMD side. Green trace shows the variation of demodulator input signal at the external charger side.	76
Figure 6.13 Backward Telemetry at 2 cm depth: Green trace shows the data modulation signal sent from at the IMD side. Yellow trace shows the low pass filtered output of the peak detector at the external charger side.	77
Figure 6.14 Backward Telemetry at 2 cm depth: Green trace shows the data modulation signal sent from the IMD side. Yellow trace shows the amplified signal before inverting comparator at the external charger side.	77
Figure 6.15 Backward Telemetry at 2 cm depth: Green trace shows the data modulation signal sent from the IMD side. Yellow trace shows the demodulated signal at the external charger side.	78
Figure 6.16 Backward Telemetry at 2 cm depth: Green trace shows the data modulation signal sent from the IMD side. Yellow trace shows the rectified voltage variation at the IMD side during data transfer.	78
Figure 6.17 Backward Telemetry at 1 cm depth: Green trace shows the data modulation signal sent from the IMD side. Green trace shows the variation of demodulator input signal at the external charger side	79

Figure 6.18 Backward Telemetry at 1 cm depth: Green trace shows the data modulation signal sent from the IMD side. Green trace shows the variation of demodulator input signal at the external charger side	79
Figure B.1 Schematic diagram for the calculation of z-directed H-fields applied to target wire A by source wires B and C, I_0 is current on each wire, r_0 is conductor radius, α , β and γ are reference points [4]	89
Figure B.2 Schematic of coil configuration when calculating H-fields on the m-th wire in a system of N turns [4]	90
Figure C.1 External Charger Device: Schematic of Module Power Supply . . .	93
Figure C.2 External Charger Device: Schematic of ClassE Power Amplifier . .	94
Figure C.3 External Charger Device: Schematic of Demodulator Circuit	94
Figure C.4 External Charger Device: Schematic of MCU and User Interface . .	95
Figure C.5 PCB layout of the external charger	95
Figure D.1 Implantable Medical Device: Schematic of Power Harvester and Modulator	97
Figure D.2 Implantable Medical Device: Schematic of Demodulator Circuit . .	97
Figure D.3 Implantable Medical Device: Schematic of Battery Charger and LED Simulator	98
Figure D.4 Implantable Medical Device: Schematic of MCU	98
Figure D.5 PCB layout of implantable medical device	99

LIST OF ABBREVIATIONS

IMDs	Implantable Medical Devices
WPT	Wireless Power Transfer
SCMR	Strongly Coupled Magnetic Resonances
NFC	Near Field Communication
ZVZC	Zero Voltage/Zero Current
CCCV	Constant Current/Constant Voltage

CHAPTER 1

INTRODUCTION

Implantable medical devices (IMD) are utilized increasingly in a wide range of area to monitor or threat disorders in body. Cardiac, spinal, cortical implants have shown great improvement in functionality in the last decades. Traditional methods to power these devices usually employ implantable batteries and percutaneous links. Using a percutaneous link involves high risk for infection. On the other hand, implantable battery has limited operation time depending on its energy storage capacity. Due to long-term usage needs and patient safety, wireless power transfer (WPT) has become the preferred solution for IMDs [5].

IMDs can be either powered directly from a WPT system or using a rechargeable battery which is charged with WPT. The design of the WPT employed in these devices significantly depends on the implantable device's power and size requirements. However, the main problem of IMDs using WPT is the power transfer efficiency. Most of these devices are powered using magnetic induction methods. Because of the limited area on the implant side, weak coupling exists between the transmitter and receiver coils and this limits the implant depth of the implantable device. Secondly, devices requiring higher power for operation (neurostimulators, left ventricular assist devices, etc.) are placed in soft tissue due to the size of these devices. For such devices, the optimum implant depth can vary from within subjects and additional control mechanisms should be employed to account for the variable coupling problem.

1.1 Scope of Thesis

The primary intend of this thesis study is to realize a WPT system to supply wireless power for implantable medical devices that utilize a rechargeable battery. Specific goals are as follows,

- to improve the WPT efficiency at increased implant depths,
- to construct an adaptive efficiency improvement method for varying positions and orientations during WPT
- to perform a telemetry system to communicate with the IMD and control the WPT operation

In order to achieve these objectives for complete system design, in this thesis step by step design approach is applied. Analytical model of the WPT system is optimized by preparing a design flowchart and results are verified by numerical analysis. Hardware design for complete WPT performance is studied by performing circuit analysis. Finally experimental setup is prepared to validate proposed system.

1.2 Literature Review

Literature research on WPT for implantable medical devices is confined into 3 major approaches: magnetic coupling, capacitive coupling and ultrasonic transmission [6].

1.2.1 Ultrasonic Energy Transfer

For implantable medical devices ultrasound waves that have frequencies generally greater than 200 kHz are used. The waves propagate through tissue and carried energy is converted to electrical energy by using a piezoelectric transducer inside the device. Comparing with inductive coupling the effort shown in this area is quite less. There are some researches that transfer energy up to tens of mWatts effectively. In [7], 70mW power at 40 mm implant depth is transferred with % 27 efficiency.

Human body is composed of different organs with different densities. Therefore, acoustic impedance in the body changes significantly and this limits the use of ultrasonic power transfer in specific body locations, like soft tissue with no bone. Acoustic impedance of bone is so high, therefore almost all of the ultrasound wave is reflected back [8].

The second and main problem for this method is the long-term effects to tissue long term effects of vibrations caused by ultrasound are not investigated in detail yet.

1.2.2 Capacitive Coupling

Capacitive coupling is a near field wireless power transfer solution that utilizes the construction of an electric field between two conductive plates. As time-varying voltage excites the transmitter plate, wireless power transfer over tissue is established by the displacement currents [9].

For high power transfer capability, either the strength or the rate of change of the electric field should be high. Electric field strength could be increased by reducing implant depth and this limits the application range. High operating frequency on the other hand, decreases the DC rectification efficiency. Nevertheless, the method is suitable only for implantable devices with low power requirements (a few mWatts) and having implant depths less than 1 cm [10].

1.2.3 Magnetic Coupling

1.2.3.1 Mid-Field and Far-Field Electromagnetic Coupling

Mid-field wireless power transfer could be used for miniaturized implants with the receiver size being much smaller than the wavelength of the corresponding operation frequency. The distance between the transmitter and receiver is on the order of one wavelength. The weak coupling is compensated by high frequency but still the received power remains about a few mWatts and the transfer efficiency is too low [11].

Far-field coupling relies on the principle of electromagnetic radiation. The method is well investigated at free space but resources for biomedical application is still limited. That is mainly due to the of high operation frequency (GHz range). At very high frequencies, the tissue and rectifier losses become important. Therefore, low overall power transfer efficiency makes this method impractical for use in IMDs [12].

1.2.3.2 Near-Field Inductive Coupling

Near-Field inductive coupling is the traditional and safety proven WPT method. The method simply works on the principle of electromagnetic induction. A transmitter coil placed in close proximity with the IMD generates a time-varying magnetic field, which in turn, induces electromotive force (emf) in the receiver coil.

Researchers have proposed numerous near-field inductive coupling methods for IMDs. These methods differ from each other in terms of the resonance structure and the number of coils used in the models, which will be explained in detail in the next chapter.

In order to perform a quantitative comparison of these methods used in IMDs, a comprehensive literature survey is conducted. In all these studies, the transmitter side is driven by an AC source and there is no rectification at receiver side. Therefore, the power transfer efficiencies of these systems are AC to AC for voltage (or current) point of view.

Luo et. al. used a 4-coil resonant based WPT system for DBS devices at 4.07MHz [13]. Cylindrical coil with 14 mm diameter and 3 mm height was used at receiver side. Experiment accomplished when air was between coils and at 10cm distance. Results show 6.775 % efficiency to power 10 Ω load at receiver side.

Bhuyan et. al. used a 2-coil resonant based WPT system at 720 KHz [14]. Air core results of the study shows 32 % efficiency at 4 cm distance to power 20 Ω load.

Xue et. al used a 2-coil resonant based WPT system at ISM band (13,56MHz) [15]. The coils were fabricated on PCB. Receiver coil with dimensions 25 mm x 10mm was used to power 50 Ω load. At 2 cm distance 20,5 % efficiency was reached at air core and 18,3 % under pork tissue.

RamRakhyani et. al. used a 3-coil resonant based WPT system with 2 coils at transmitter side and a single coil at receiver side [16]. In this work, Litz wire was used at the receiver side with a coil diameter of 1,5 cm. Frequency of operation was 3,37 MHz and 55 % efficiency is obtained at air core to power 110 Ω load at 1 cm implant depth.

Hu et. al. used a 4-coil resonant based WPT with self-resonant coils [17]. In order to achieve self resonance at the receiver coil a 1,5 cm radius coil at a very high operation frequency (226 MHz) is used. Results demonstrates 46,7 % efficiency at 30 mm distance under tissue.

Chiao et. al. used a 4-coil resonant based WPT system at 700 KHz [18]. Receiver coil was composed of Litz wire with 22 mm in diameter and 2.5 mm in height. At 20 mm implant depth, system reaches 70 % efficiency under air core.

1.3 Thesis Organization

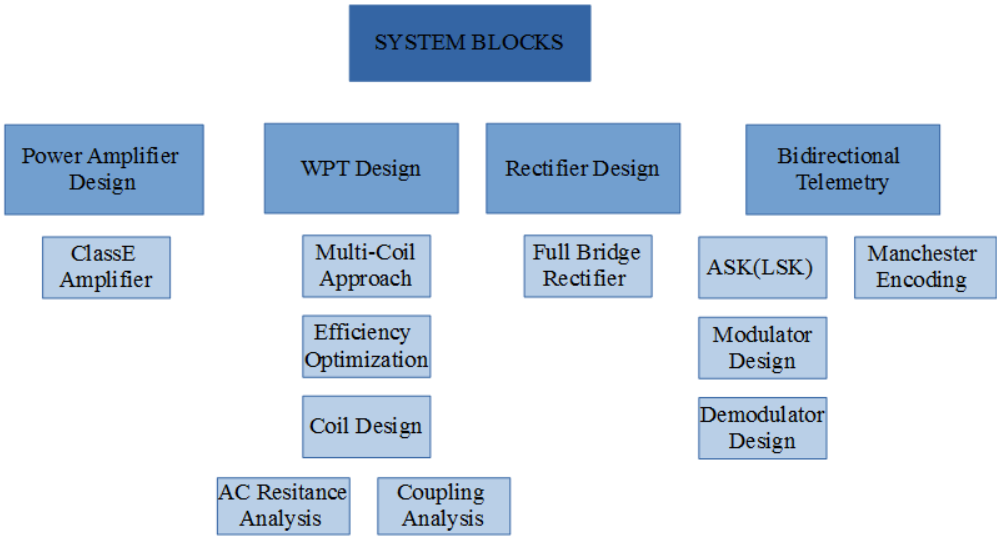


Figure 1.1: System Blocks

In Chapter 2, theory of wireless power transfer via electromagnetic induction is explained first. A novel method of Strongly Coupled Magnetic Resonance is analyzed and critical parameters for coil design are demonstrated.

In Chapter 3, power amplifier and rectifier structures are discussed in detail. Effects of these blocks on WPT performance are analyzed for complete system performance.

In Chapter 4, wireless power transfer design procedure is explained and design is completed. Adaptive system operation and corresponding feedback mechanisms are presented.

In Chapter 5, near field communication over WPT system is explained. Modulation and encoding schemes are analyzed and related hardware design is exhibited.

CHAPTER 2

WIRELESS POWER TRANSFER VIA ELECTROMAGNETIC INDUCTION

2.1 Theory

The fundamentals of wireless power transfer via electromagnetic induction consist Biot-Savart Law and Faraday's Law of induction and Lenz Law.

Assuming an electrical current is passing through a coil, magnetic flux density generated by the flow of charges is given by Biot-Savart Law [19], [20],

$$\vec{B} = -\frac{\mu_0}{4\pi} \oint_l \frac{I d\vec{l} \times \vec{e}_r}{r^2} \quad (2.1)$$

where r is the distance from the wire element to the point at which the field is being computed, \vec{e}_r is the unit vector of r . $I d\vec{l}$ is linear-current-element in the wire, and μ_0 is the permeability of free space.

If the current I passing through coil is time varying, magnetic flux density expression also varies depending on the frequency and position of the field point.

If there are two coils, and one of the coils (transmitter coil) is excited, the magnetic flux Φ_{21} in the second coil (receiver coil) can be expressed as,

$$\Phi_{21} = \int_s \vec{B}_{21} \cdot d\vec{S}_2 \quad (2.2)$$

where \vec{B}_{21} is the magnetic flux density generated by transmitter coil, S_2 is the surface

of secondary coil. Voltage induced on the receiver coil due to alternating magnetic field generated by the first coil is given by Faraday's law of induction [19], [20] :

$$v_2(t) = \oint \vec{E} \cdot d\vec{l} = -\frac{d\Phi_{21}(t)}{dt} \quad (2.3)$$

where $v_2(t)$ is the induced voltage in the second coil and \vec{E} is the induced electric field strength.

Mutual inductance M_{21} can be defined as the ratio of the partial flux Φ_{21} enclosed by conductor loop 2, to the current I_1 in conductor loop 1 as shown in Fig. 2.1.

$$M_{21} = \oint_{S_2} \frac{\vec{B}_{21}(I_1) \cdot d\vec{S}_2}{I_1} = \frac{\phi_{21}(I_1)}{I_1} \quad (2.4)$$

Similarly self inductance L_1 of coil 1 becomes,

$$L_1 = \frac{\Phi_{11}(I_1)}{I_1} \quad (2.5)$$

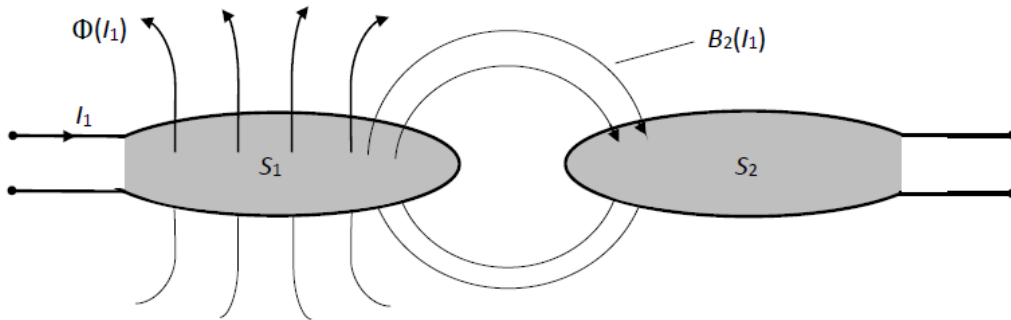


Figure 2.1: Mutual inductance M_{21} by the coupling of two coils via a partial magnetic flow

For the closed loop case of second coil (i.e current passes over coil), the current through L_2 also generates an additional magnetic flux ϕ_{22} , which opposes the magnetic flux ϕ_{21} (Lenz Law) [21].

Using Eq. (2.4), (2.5) and (2.6) the voltage on coil 2 becomes,

$$\begin{aligned} v_2(t) &= \frac{d\Phi_2}{dt} = \frac{d\Phi_{21} - d\Phi_{22}}{dt} \\ &= M \frac{di_1}{dt} - L_2 \frac{di_2}{dt} \end{aligned}$$

Here i_2 is the short circuit current in the second loop due to current i_1 in the first loop. Figure 2.2 shows the circuit model of magnetically coupled conductors (coils). If the receiver coil's internal resistance R_2 is also taken into account, the voltage $v_2(t)$ on the load resistance R_L can be written as,

$$v_2(t) = M \frac{di_1}{dt} - L_2 \frac{di_2}{dt} - i_2 R_2 \quad (2.6)$$

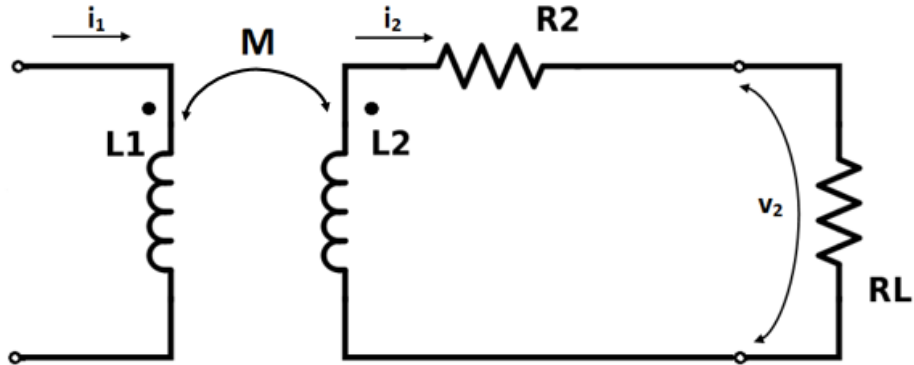


Figure 2.2: Equivalent circuit for magnetically coupled coils. L_1 and L_2 refers to the inductance of transmitter and receiver coils respectively, R_2 is internal resistance of receiver coil, R_L is load resistance and v_2 is voltage on the load resistance.

Since the currents passing through the coils are sinusoidal for most of the cases we can write Eq.(2.6) in complex notation for $\omega = 2\pi f$,

$$V_2 = j\omega M I_1 - j\omega L_2 I_2 - I_2 R_2 \quad (2.7)$$

Replacing $V_2 = I_2 R_L$ in Eq.(2.7) gives the relation between I_1 and I_2 .

$$I_2 = \frac{j\omega M I_1}{j\omega L_2 + R_2 + R_L} \quad (2.8)$$

Modeling equivalent circuit of the transmitter coil under magnetic coupling with the receiver coil introduces a new imaginary impedance Z_{ref} , which is the reflected impedance from the receiver coil [22]. Figure 2.3 shows the model.

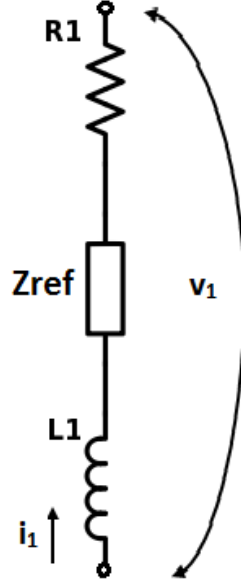


Figure 2.3: Equivalent circuit diagram of transmitter under mutual coupling. L_1 is transmitter coil inductance, R_1 its internal resistance and Z_{ref} is reflected impedance from receiver, i_1 is current passing through the coil and v_1 is voltage across the coil.

If the similar approach is applied at transmitter side, voltage across transmitter coil is calculated as follows,

$$V_1 = j\omega L_2 I_1 - j\omega M I_2 + I_1 R_1 \quad (2.9)$$

Replacing I_2 with I_1 from Eq.(2.8) gives the equivalent transmitter coil impedance Z_1 ,

$$Z_1 = \frac{V_1}{I_1} = j\omega L_2 + R_1 + Z_{ref} \quad (2.10)$$

where

$$Z_{ref} = \frac{(\omega M)^2}{j\omega L_2 + R_2 + R_L} \quad (2.11)$$

Then, in general form the reflected impedance seen at the transmitter side is,

$$Z_{ref} = \frac{(\omega M)^2}{Z_{rec}} \quad (2.12)$$

where Z_{rec} is the equivalent impedance seen at the receiver side.

2.1.1 Resonant Wireless Power Transfer

Maximum power efficiency for a resistive load can be achieved at the resonance condition. In the same way, for a properly designed wireless power transfer system the maximum efficiency is achieved at resonance condition [23],[24].

Figure 2.4 shows the basic circuit structure of a wireless power transfer system with magnetic induction. The system is composed of two series tuned resonant tanks. Power transfer efficiency of the all system is found by multiplying the efficiency of each resonant tank. For each loop (tank), efficiency is defined as the power transferred to the load over total power appear on all elements.

Total power transfer efficiency, voltage source at transmitter side and voltage sink at receiver side, is described as,

$$\eta = \frac{\text{Power dissipated on load } R_L \text{ at the receiver}}{\text{Power transmitted from the source } V_s} \quad (2.13)$$

Power efficiency at transmitter side,

$$\eta_1 = \frac{\text{Re}\{Z_{ref} I_1 I_1^*\}}{\text{Re}\{V_s I_1^*\}} \quad (2.14)$$

Power efficiency at receiver side,

$$\eta_2 = \frac{\text{Re}\{R_L I_2 I_2^*\}}{\text{Re}\{(R_L + j\omega L_2 + \frac{1}{j\omega C_2} + R_2) I_2 I_2^*\}} \quad (2.15)$$

The overall efficiency is,

$$\eta = \eta_1 \cdot \eta_2 \quad (2.16)$$

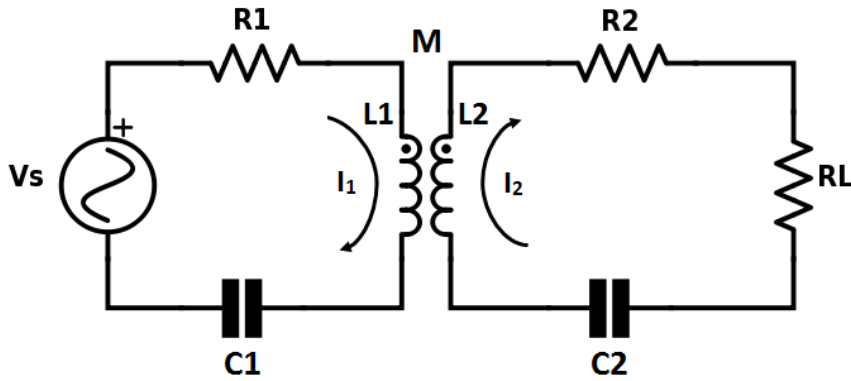


Figure 2.4: Basic circuit structure for resonant wireless power transfer system. L_1 , L_2 transmitter and receiver coil inductances respectively, C_1 , C_2 corresponding series tuning capacitors, M mutual inductance between coils.

At the resonance condition, where $\omega = \omega_0 = \frac{1}{\sqrt{L_1 C_1}} = \frac{1}{\sqrt{L_2 C_2}}$, Z_{ref} becomes pure resistive and efficiency becomes,

$$\eta = \frac{Z_{ref}}{Z_{ref} + R_1} \frac{R_L}{R_L + R_2} \quad (2.17)$$

2.1.1.1 Resonant Structures

Four circuit topologies, based on tuning capacitance connection type are shown in Figure 2.5.

- Series-Series Resonant
- Series-Parallel Resonant
- Parallel-Parallel Resonant
- Parallel-Series Resonant

Considering the practical implementations of a wireless power transfer system, the power source of the system is mostly a battery, not an alternating source. Due to the need of a sinusoidal current to drive the system, a power amplifier should be used. Efficient amplifier topologies like class E (or class F) amplifiers are series resonant circuits. Consequently, on the transmitter side the series resonant circuit is suitable choice.

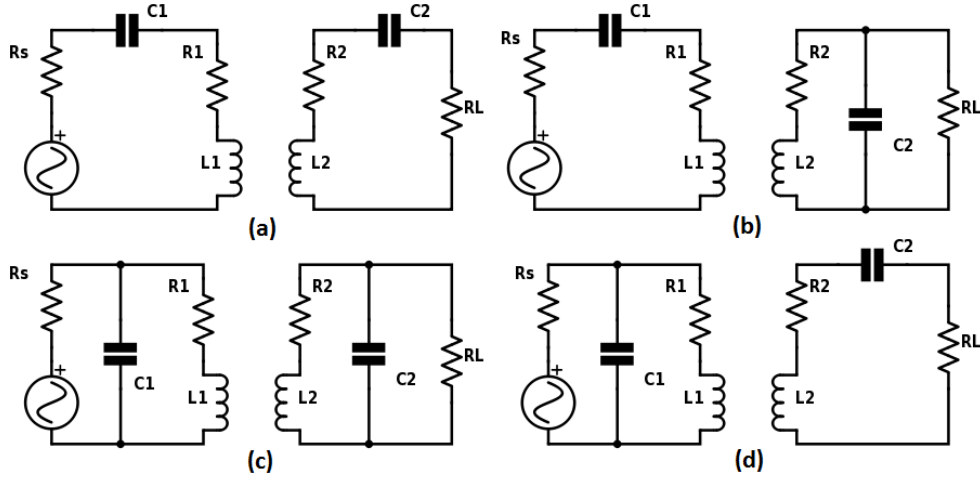


Figure 2.5: Circuit models : (a) series-series resonant , (b) series-parallel resonant , (c) parallel-parallel resonant , (d) parallel-series resonant

On the receiver side, parallel topology analysis shows that there could be two capacitor values for resonance condition depending on the load resistance. The impedance seen due to mutual coupling at the receiver side,

$$Z_{seen} = j\omega L_2 + R_{L2} + \left(\frac{1}{j\omega C_2} + R_{C2} \right) // R_L$$

The formula above shows resonance condition that does not only depend on tuning capacitor but also the load resistance (i.e tuning capacitor value changes depending on the load resistance). Therefore for systems with variable load, parallel resonant structure is not suitable.

In this study charging rate is not variable. However, when wireless power transfer system is active, the power is not only consumed for charging the battery but also by other system activities of the IMD. Therefore from WPT perspective load is not fixed during operation and series resonant structure at receiver side is a better choice.

2.2 Strongly Coupled Magnetic Resonance

Strongly coupled magnetic resonance (SCMR) fills the gap between two main wireless power transfer methods, electromagnetic radiation and electromagnetic induction [1]. Electromagnetic radiation transmits power to long distances with low efficiency while electromagnetic induction powers short distances with high efficiency. SCMR achieves high efficiencies at mid-field, i.e. for distances lower than wavelength of the signal by using high quality factor coils [25].

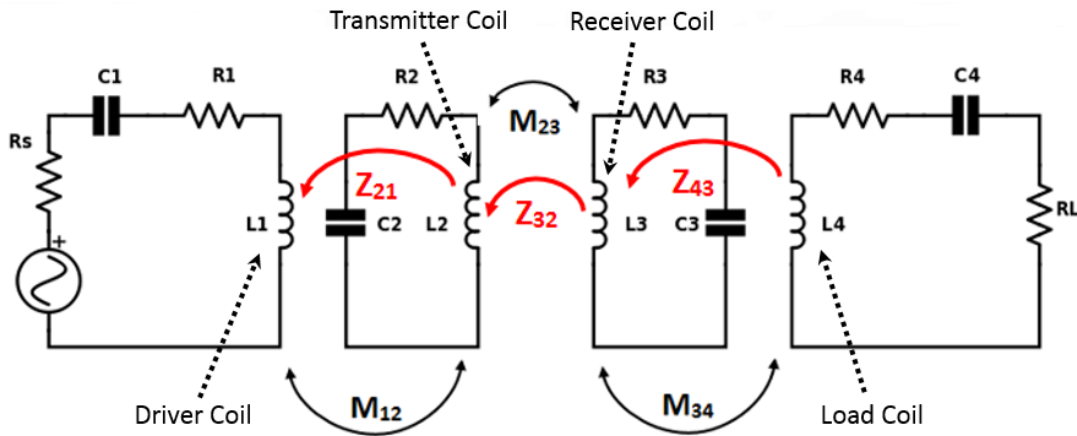


Figure 2.6: Strongly Coupled Magnetic Resonance System Architecture

SCMR is mainly a form of resonant magnetic induction implemented with four coils as seen in Figure 2.6. In this method the actual power transfer exists between the middle very high Q resonators. Driver coil is used to increase reflected load against source resistance and load coil is used to minimize load resistance to achieve higher reflection. Since the loaded Q factors of the resonators are high, minimal power loss could be achieved during the power exchange between inductor and capacitor of the corresponding resonator. Consequently a high efficiency system could be designed even at a low coupling.

From the reflected load theory, Eq.(2.12), load reflected on transmitter coil is inversely proportional with the load at receiver side. The critical part of the SCMR operation is to transform receiver load to a minimum resistance. In this way reflection on the transmitter increases and higher power transfer efficiency is established.

If high quality factor coils at implant size could be achieved at a frequency that does

not generate high tissue losses, a wireless charging system for an implantable biomedical device with high efficiency could be obtained with SCMR implementation.

The original derivation of SCMR is based on Coupled Mode Theory [25], [26]. But Reflected Load Theory also gives the same result [27] and in this thesis the system will be evaluated by Reflected Load Theory.

Figure 2.6 describes the simplified system model, where the mutual inductance between nonadjacent coils are ignored. This assumption is based on the coil locations. Because coil 1 is in close proximity with coil 2 and physically constructed smaller, coil 2 magnetically shields the interaction of coil 1 with other coils. Therefore mutual couplings M_{13} and M_{14} are negligible. Similarly due to same reasons M_{24} is also not taken into account.

Performing Kirchhoff's Voltage Law (KVL) to the model shown, the relationship between currents through each coil and the voltage applied to the driver coil can be shown as :

$$\begin{bmatrix} V_s \\ 0 \\ 0 \\ 0 \end{bmatrix} = \begin{bmatrix} R_s + Z_1 & -j\omega M_{12} & 0 & 0 \\ -j\omega M_{12} & Z_2 & -j\omega M_{23} & 0 \\ 0 & -j\omega M_{23} & Z_3 & -j\omega M_{34} \\ 0 & 0 & -j\omega M_{34} & Z_4 \end{bmatrix} \begin{bmatrix} I_1 \\ I_2 \\ I_3 \\ I_4 \end{bmatrix} \quad (2.18)$$

where

$$Z_1 = R_s + R_1 + j(\omega L_1 + \frac{1}{\omega C_1})$$

$$Z_2 = R_2 + j(\omega L_2 + \frac{1}{\omega C_2})$$

$$Z_3 = R_3 + j(\omega L_3 + \frac{1}{\omega C_3})$$

$$Z_4 = R_L + R_4 + j(\omega L_4 + \frac{1}{\omega C_4})$$

Solving the equation by applying the Reflected Load Theory gives the closed loop formula for the system impedance Z_{sys} ,

$$Z_{sys} = \frac{V_s}{I_1} = \left(Z_1 + \frac{(\omega M_{12})^2}{Z_2 + \frac{(\omega M_{23})^2}{Z_3 + \frac{(\omega M_{34})^2}{Z_4}}} \right) \quad (2.19)$$

At the resonant condition, where the driving frequency generates no imaginary impedance on the tanks, $\omega = \omega_0$, impedance of individual tanks become,

$$Z_1 = R_s + R_1$$

$$Z_2 = R_2$$

$$Z_3 = R_3$$

$$Z_4 = R_L + R_4$$

Designing the system based on Eq.(2.18) is not the best way to optimize power transfer efficiency, because the effects of each resonators on system is not seen clearly. Finding the efficiency of each individual loop and investigating the effect on neighbor loop is a better way to characterize the system.

$$\eta_{sys} = \eta_1 \cdot \eta_2 \cdot \eta_3 \cdot \eta_4 \quad (2.20)$$

where (at $\omega = \omega_0$),

$$\eta_1 = \frac{Z_{21}}{Z_{1,ref}}, \quad Z_{21} = \frac{(\omega M_{12})^2}{Z_{2,ref}}, \quad Z_{1,ref} = Z_{21} + Z_1$$

$$\eta_2 = \frac{Z_{32}}{Z_{2,ref}}, \quad Z_{32} = \frac{(\omega M_{23})^2}{Z_{3,ref}}, \quad Z_{2,ref} = Z_{32} + Z_2$$

$$\eta_3 = \frac{Z_{43}}{Z_{3,ref}}, \quad Z_{43} = \frac{(\omega M_{34})^2}{Z_4}, \quad Z_{3,ref} = Z_{43} + Z_3$$

$$\eta_4 = \frac{R_L}{Z_4}$$

Z_{ij} is the reflected impedance from i_{th} coil to j_{th} coil and $Z_{i,ref}$ is the total impedance seen on i_{th} resonator with reflection. That is reflected load from neighboring coil is added to resonant loops. The formulation is valid for resonant operation, that is all the reflections are resistive. Otherwise complex power equations need to be used to find efficiency as in Eq (2.13) and Eq (2.14). The methodology is going to be used at WPT Design section to maximize the WPT efficiency.

2.2.1 Frequency Splitting Phenomenon on SCMR

Frequency splitting phenomenon is a result of increasing coupling between transmitter and receiver blocks. As the coupling between coil 2 and coil 3 increases reflected load on coil 2 increases. The increase makes the load reflected on coil 1 smaller. After a point reflected load on coil 1 becomes very low and first resonator efficiency drops significantly. This efficiency drop effects all system performance.

In the case the system efficiency maximizes at both below and above of original system resonant frequency. The system behavior depends on the load impedance and coupling coefficient k_{23} between the resonant coils.

The overall system could be evaluated around critically coupled points as seen at Figure 2.7. At this point where $k_{23} = k_{crit}$ the reflected impedance from secondary coil to primary coil is equal to the initial impedance of the primary coil Z_1 . When k_{23} lower than k_{crit} the system is under-coupled and reflected impedance is smaller than the initial impedance of primary coil.

In the over-coupled area the impedance reflected from secondary coil to primary coil is smaller than the initial impedance of the primary coil. This means that power is mostly dissipated at the load side. In this region efficiency peaks at two symmetric

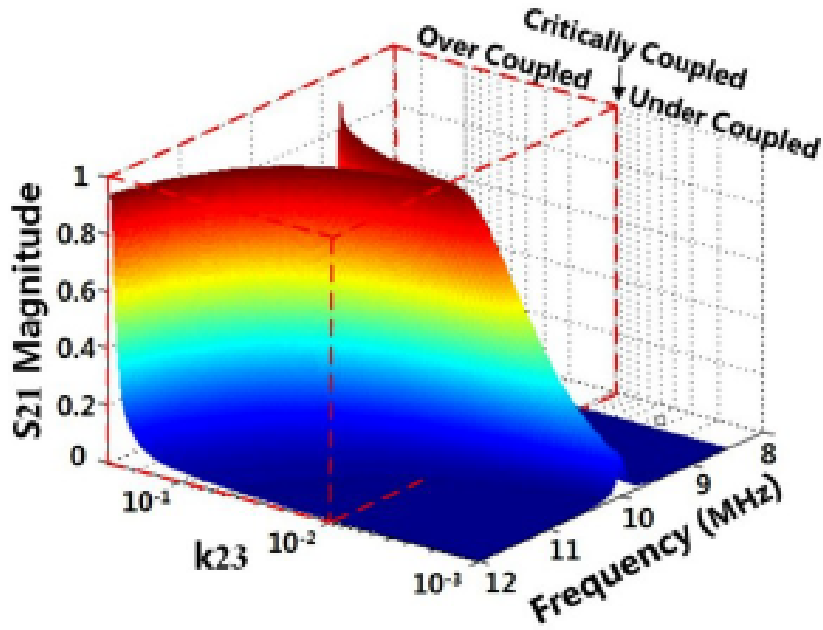


Figure 2.7: S_{21} magnitude as a function of frequency and coupling coefficient k_{23} [1]

(assuming ac resistances of coils remain same) roots around original resonant frequency and as coupling increases roots go far away from each other 2.7.

Frequency splitting is a critical part to discuss before starting design. In order to maintain the high efficiency operation frequency must be changed. That makes WPT control difficult and results in more complex control systems.

2.3 Coil Design

Circular geometry is concerned for the design due to the reasons:

- its conformity for the implantable medical device physical properties
- to make the analytical expressions easier

For a single loop coil with the condition $R/a \ll 1$, the self inductance of the coil is given by

$$L(a, R) = \mu_0 a \left(\ln\left(\frac{8a}{R}\right) - 2 \right) \quad (2.21)$$

where a is the radius of the coil and R is the wire radius.

Self inductance of a coil is calculated by summing single loop inductances of individual turns and also adding each mutual inductance between turns .

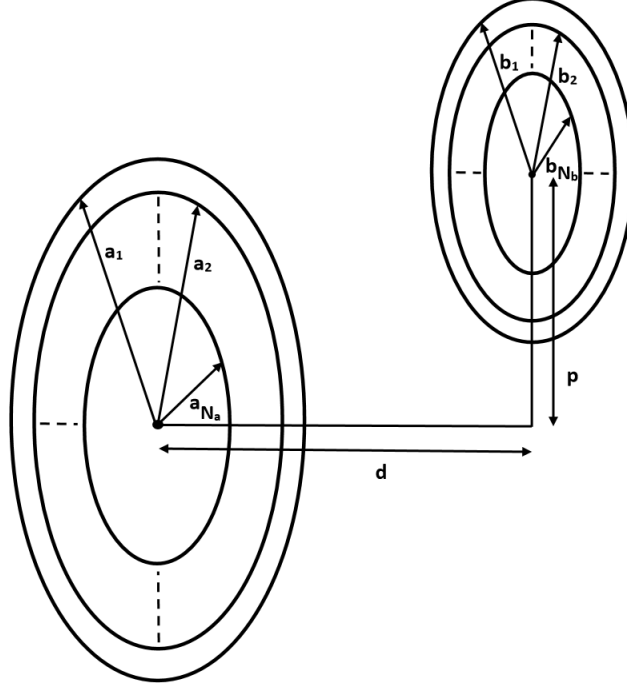


Figure 2.8: Geometric arrangement and notation for primary and secondary coils composed of concentric circular loops. a_i and b_i are coil radii of the corresponding turns, d is distance between coils, p is distance between axes, N_a and N_b are turn counts of the corresponding coils

For relative permeability of the wire and the surrounding environment is unity, mutual inductance M [28],

$$M(a, b, p, d) = \pi\mu_0\sqrt{\frac{a}{b}} \int_0^{\text{inf}} J_1(x\sqrt{\frac{a}{b}})J_1(x\sqrt{\frac{b}{a}})J_0(xp/\sqrt{ab}) \exp(-xd/\sqrt{ab})dx \quad (2.22)$$

where a radius of first loop, b radius of second loop, p axial misalignment, d distance between loops and J_0 , J_1 are Bessel functions of zeroth and first order respectively.

Mutual inductance for the perfect coupling case (i.e axially aligned) is calculated by,

$$M(a, b, p = 0, d) = \mu_0\sqrt{ab}[(\frac{2}{\kappa} - \kappa)K(\kappa) - (\frac{2}{\kappa})E(\kappa)] \quad (2.23)$$

where $\kappa = \left(\frac{4ab}{(a+b)^2+d^2}\right)^{\frac{1}{2}}$ and $K(\kappa), E(\kappa)$ are complete elliptic integrals of the first and second kind.

Therefore the overall self inductance of a coil with circular geometry (helix or spherical) is given by,

$$L_a = \sum_{i=1}^{N_a} L(a_i, R) + \sum_{i=1}^{N_a} \sum_{j=1}^{N_b} M(a_i, a_j, p=0, d=0)(1 - \delta_{i,j}) \quad (2.24)$$

2.4 Coupling Between Coils

The coupling coefficient “ k ” between coils is defined by,

$k = \frac{M_{ab}}{\sqrt{L_a L_b}}$ where M_{ab} is the mutual inductance between coils and L_a and L_b are self inductances of the coils. The mutual inductance between two coils are found by summing the mutual inductance of each turn of one coil with every other turn of the other coil .

$$M_{ab} = \sum_{i=1}^{N_a} \sum_{j=1}^{N_b} M(a_i, b_j, p, d) \quad (2.25)$$

where N_a, N_b denote the number of turns in the two and a_i, b_j are the loop radius for the corresponding turn.

2.5 AC Resistance of a Coil

The theory behind Strongly Coupled Magnetic Resonance requires high quality factor “ Q ” coils. Q factor is given by,

$$Q = \frac{\text{storage power}}{\text{dissipating power}} = \frac{\omega L}{R}$$

where ω is angular frequency (at resonance), L is inductance of coil and R is the resistance (AC resistance) of the coil.

Since the implantable device is small, it is not possible to use a high inductance coil inside the device. The only way to design a high Q coil is to increase frequency while keeping ac resistance low.

2.5.1 Litz Wire

Litz wire type consists individually insulated parallel (twisted or not) strands and constructed to reduce ac resistance losses due to skin and proximity effects up to a few MHz. Therefore the wire type is the best candidate to achieve high Q coils. Calculating the ac losses of the coil formed by Litz wire correctly is a major process for the design procedure.

Two methods are concerned for calculating the ac losses.

2.5.1.1 Method 1

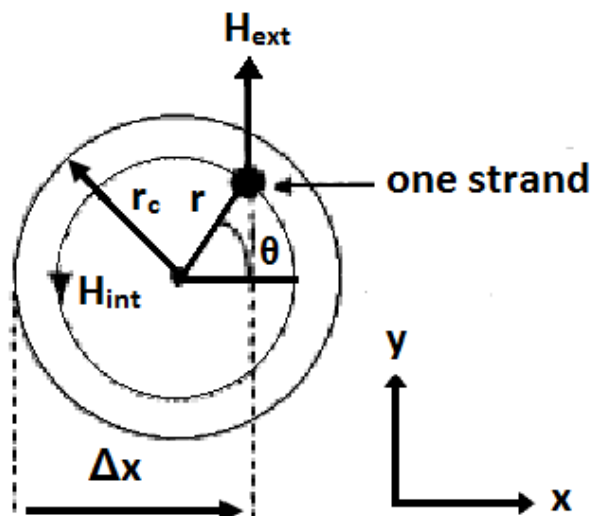


Figure 2.9: External and Internal magnetic field on a single turn where r_c is conductor radius and r is position of the strand in conductor (Litz wire) [2]

This method calculates Eddy current losses due to alternating AC current and then finds AC resistance of the coil in a closed loop formula [2]. Figure 2.9 shows magnetic field at a point(strand) over the coil formed by magnetic field generated by other turns H_{ext} and the magnetic field generated by the turn itself H_{int} . Therefore the overall H

field at a point expressed as,

$$\vec{H} = \vec{H}_{ext} + \vec{H}_{int} = (H_{ext} + H_{int} \sin \theta) \vec{y} + H_{int} \cos \theta \vec{x} \quad (2.26)$$

A critical assumption in the method is, it calculates the H – *field* across the winding layers with linear distribution. Then H_{ext} is found as follows,

$$H_{ext}(\Delta x, k) = (k - 1)I_L + I_L \frac{\Delta x}{2r_c} \quad (2.27)$$

$$\Delta x = r_c + r \cos \theta$$

$$H_{int}(r) = \frac{Ir}{2\pi r^2} \quad (2.28)$$

where k is the layer number , I_L is amplitude of current by unit width of a layer, r_c is conductor radius and r is position of strand in the turn. For a single layer coil, layer number corresponds to turn number.

Using the result in Appendix A, AC resistance of Litz wire per unit length is found as,

$$R_{AC} = \frac{2P}{I^2} = \frac{\sqrt{2}Np}{\pi\delta N_0 d_0} (\Psi_1(\psi) - \frac{\pi^2 N_0 \beta}{24} (16m^2 - 1 + \frac{24}{\pi^2}) \Psi_2(\psi)) \quad (2.29)$$

2.5.1.2 Method 2

This method is implemented by evaluating the magnetic field distribution on each conductor that caused by other turns independently.

Appendix B explains the derivation in detail and result is used to calculate AC resistance of planar spiral coil constructed by Litz wire.

From [29], losses of a spiral planar winding constructed by Litz wire could be calculated by integrating conduction losses, eddy current losses due to internal magnetic

field and eddy current losses due to H_{ext} (generated by other turns) for each turn of the coil.

$$R_{AC} = \frac{\sqrt{2}pNI}{\pi\delta N_0 d_0} \Psi_1(\psi) - \frac{\sqrt{2}p\beta NI}{\pi\delta d_0} \Psi_2(\psi) - \frac{8\sqrt{2}\pi\beta r_c^2 I}{\delta d_0} \sum_{i=1}^N \frac{H_{ext}^2}{I^2} \Psi_2(\psi) \quad (2.30)$$

where,

p resistivity,

N number of turns,

I current single on conductor,

N_0 number of strands Litz wire,

d_0 strand diameter,

r_c conductor radius.

2.5.1.3 Results of AC Resistance Modelling Methods

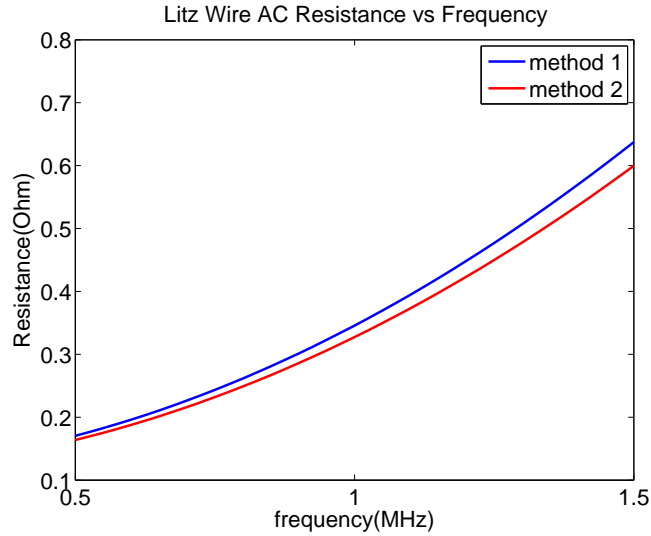


Figure 2.10: AC Resistance vs Frequency for designed transmitter coil

2.10 and 2.11 shows results of the implementation of two methods for the designed transmitter and receiver coil. Both methods are in strong correlation for both coils. The Litz wire types and the coil parameters are explained in detail in WPT Design section.

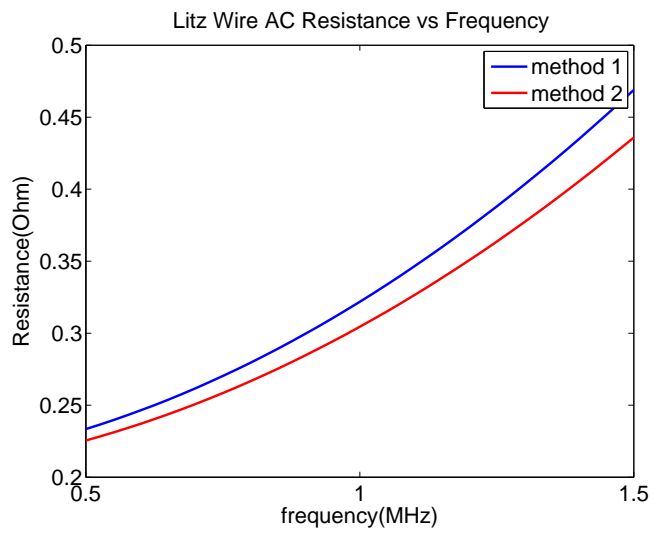


Figure 2.11: AC Resistance vs Frequency for designed receiver coil

CHAPTER 3

POWER AMPLIFIER AND RECTIFIER DESIGN

This chapter explains the design and critical points for DC to AC conversion at transmitter side and AC to DC conversion at the receiver side. It is critical to analyze power amplifier and rectifier selections before starting WPT design because this WPT analysis and adaptive system operation is closely related.

3.1 Power Amplifier Design

Implantable medical devices, either wireless powered or wireless charged, are battery powered at the transmitter side due to its practicality and safety for electrical isolation. Because inductive links use alternating magnetic field to transfer power, an AC to DC conversion is necessary. A high efficiency power amplifier is therefore critical to provide both lower power losses and lower data transfer losses.

Different power amplifiers such as A, AB, B, C, D, E, F are used in transcutaneous power amplification systems in medical frequency bands with output powers changing mW to several watts. Two main categories exist for power amplifiers: linear and switching amplifiers. Switching power amplifier is the common choice for many designs due to high efficiency and high frequency band compared to linear amplifiers.

Among switching power amplifiers, Class-E amplifiers is the one that is used widely in wireless power systems because of their simplicity [30]. In this thesis class-E amplifier is also the design choice and will be concerned in detail.

3.1.1 Class_E Power Amplifier

Most of the power amplifiers lose largest power at the switching device. Hence for class-E amplifier efficiency is maximized by minimizing those losses. The amplifier (Fig.3.2) works with zero voltage zero current (ZVZC) principle that is transistor voltage and current are not high at the same time as shown in Fig.3.1. At the transistor 'on' state, the voltage is nearly zero when current is flowing, that is, the transistor acts as a low resistance closed switch. At the transistor 'Off' state, the current is zero when there is high voltage, that is, the transistor acts as an open switch. Also for a better operation zero slope voltage and zero slope current switchings should exists at transitions to minimize losses [31].

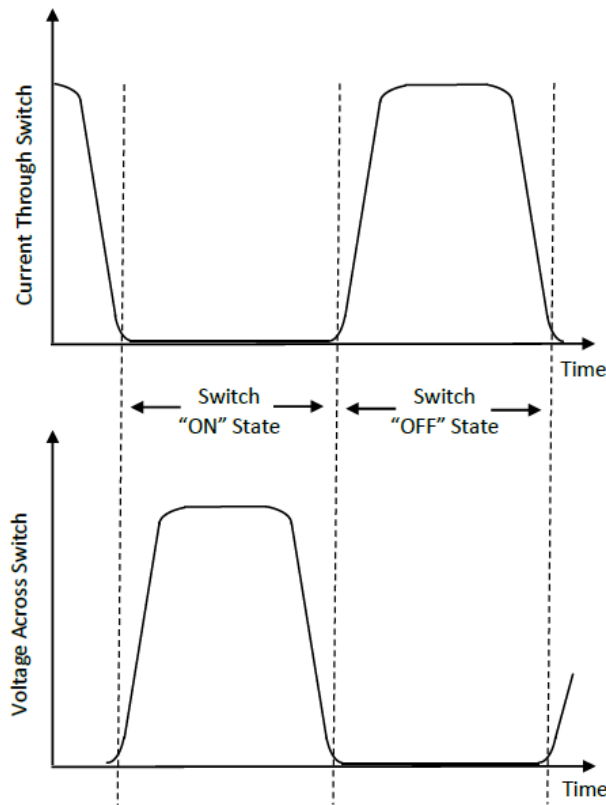


Figure 3.1: Ideal transistor voltage and current waveforms for class-E amplifier

Fig. 3.2 shows the schematic of class-E amplifier. In the circuit L_1 maintains constant current to the system, C_1 supports ZVZC operation, L_2 is transmitter coil for wireless power system, C_2 is tuning capacitor for resonant operation and R_1 is the reflected resistance from the load side.

Amplifier loaded quality factor $Q_L = \frac{\omega L_2}{R}$ is critical for operation. Because the harmonic content will be filtered out at high Q resonant tanks of the WPT system generated current at the amplifier side should be as pure as possible. The second harmonic current is $\frac{0.51}{Q_L}$ and third harmonic current is $\frac{0.08}{Q_L}$ relative to fundamental current. In nominal circuit operation minimum possible Q_L value is 1.7879 [32].

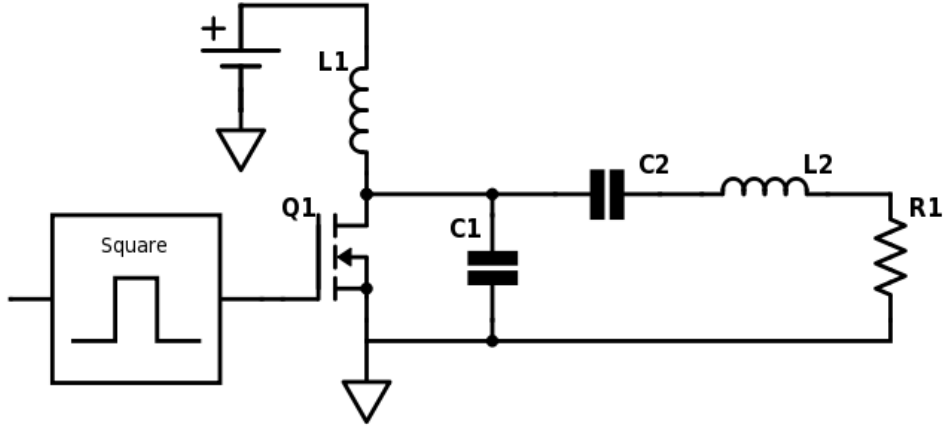


Figure 3.2: Schematic of class-E power amplifier

In the design procedure L_2 and $R1$ values are determined from the WPT design results and therefore values for the remaining circuit elements are calculated according to those. From [32]:

$$C_1 = \frac{1}{2\pi f R1 \left(\frac{\pi^2}{4} + 1\right) \frac{\pi}{2}} \left(0.99866 + \frac{0.91424}{Q_L} - \frac{1.03175}{Q_L^2}\right) + \frac{0.6}{(2\pi f)^2 L_1} \quad (3.1)$$

$$C_2 = \frac{1}{2\pi f R1} \left(\frac{1}{Q_L - 0.104823}\right) \left(1.00121 + \frac{1.01468}{Q_L - 1.7879}\right) - \frac{0.2}{(2\pi f)^2 L_1} \quad (3.2)$$

L_1 does not have a single value point, for proper operation its impedance value needs to be 30 times or more larger than impedance of C_1 .

The overall resistive losses of the amplifier is,

$$R_{load} = R1 + ESR_{L2} + ESR_{C2} + 1.365R_{on} - 0.211ESR_{C1} \quad (3.3)$$

where the ESR is equivalent series resistance.

Efficiency of the amplifier is calculated as,

$$\eta = \frac{R}{R_{load}} - \frac{(2\pi A)^2}{12} - 0.01 \quad (3.4)$$

where $A = (1 + \frac{0.82}{Q_L})(\frac{t_f}{T})$, t_f is the fall time of the drain current when the transistor is turned-off, T is the period of operation and "0.01" refers for dc-feed choke dc and RF losses.

The final equation to describe class-E amplifier is for its power output and it is calculated as follows.

$$P = \frac{(V_{CC} - V_0)^2}{R_{load}} (0.576801)(1.0000086 - \frac{0.414395}{Q_L} - \frac{0.577501}{Q_L^2} + \frac{0.205967}{Q_L^3}) \quad (3.5)$$

V_0 is the transistor saturation offset voltage and it is taken zero for field-effect transistor.

3.1.2 Class-E Amplifier Optimal Design

In wireless powering applications, the reflected impedance changes due to positional changes and load changes on the receiver side. Due to that load impedance of class-E amplifier shifts during operation and therefore optimal design value for R_{load} should be carefully investigated. Fig.3.3 shows waveforms of class-E amplifier for various loads. When R_{load} equals optimum design value (Design Point) zero voltage zero current switching appears ideally. But for the cases when Design Point does not match additional transistor losses generates. For the case $R_{load} < \text{Design Point}$, the load tends to draw current from amplifier quickly and the amplifier voltage increases to compensate this. This results in device body diode conduction during the transistor off period.

When $R_{load} > \text{Design Point}$, load tends to draw insufficient current from amplifier, yielding incomplete voltage transition. MOSFET switches when residual voltage remains on it (hard switching) which leads C_{oss} (transistor output capacitance) losses.

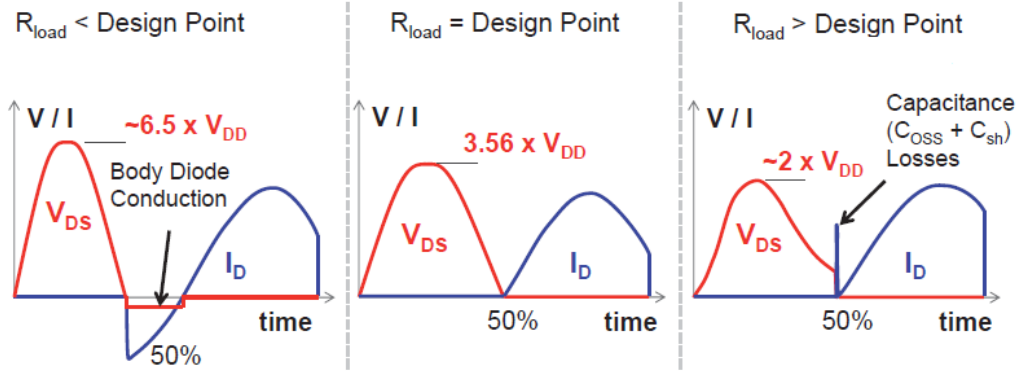


Figure 3.3: Class-E amplifier V_{DS} , I_D graphs as a function of time for different load resistances [3]

Because for the first case losses increases linearly with decreasing load and for the second case increases exponentially with increasing load , $R_{load} < \text{Design Point}$ is a better choice for load variation and should be considered first before starting the design.

3.1.3 Class-E Amplifier Design Results

The amplifier is designed according to the WPT results for operation at 4 cm implant depth. The parameters are shown in Table 3.1

Table3.1: Parameters of designed class-E amplifier

L1	C1	C2	L2	R
330 uH	4.5nF	1.18nF	22.7uH	6Ω

For 1 Mhz operation frequency, loaded quality factor of the system becomes 22 theoretically. This value is high enough for achieving almost sinusoidal current and first harmonic component of the current is only %2.2. (Fig. 3.6)

Amplifier designed with the calculated parameters are simulated at LT-Spice as shown in Table 3.4. In the simulation, 350 mΩ L2 inductor AC resistance, 100 mΩ L1 resistance and 50 mΩ capacitor parasitic resistances are included. ZV/ZC switching is seen in Fig. 3.5. Although soft switching of current is not observed, this is not critical for high efficiency operation. 715 mW power is supplied to the 6 Ohm load,

while total power input to the system is 775.5 mW. Consequently, amplifier efficiency becomes almost % 92.

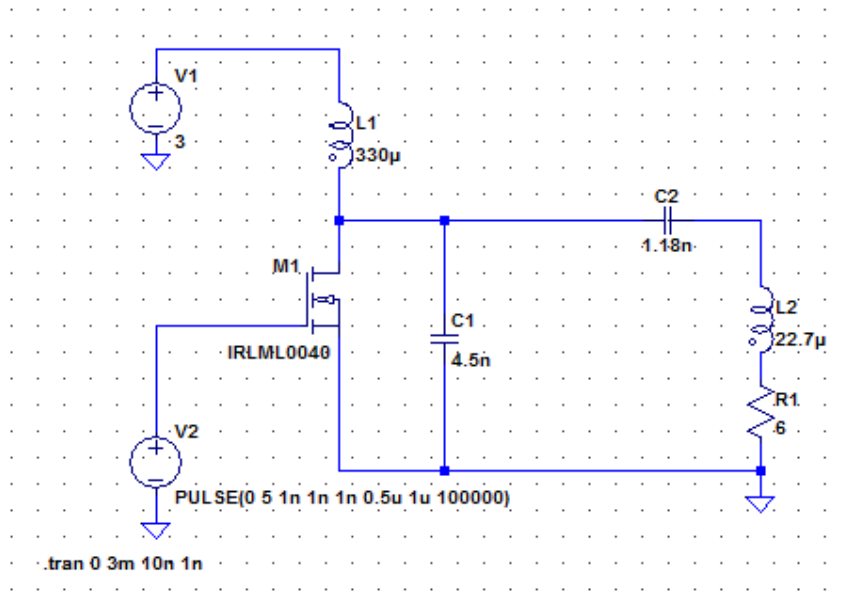


Figure 3.4: Class-E amplifier schematic on LT Spice

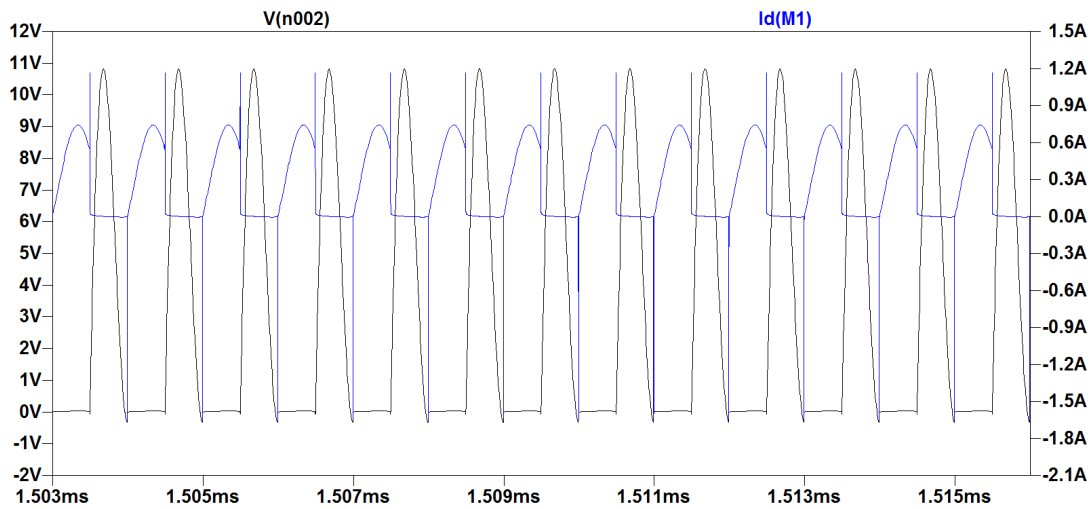


Figure 3.5: Zero voltage/Zero current switching behaviour

For distances greater than 4cm, R_{load} on the amplifier decreases and system operates below Design Point. Because in this region there are only MOSFET internal body diode losses happens and it is not very critical. No action is taken for operation when implant depth is larger than 4cm.

On the other hand, load on amplifier increases significantly due to higher coupling with the receiver for distances lower than 4 cm. This generates hard switching losses

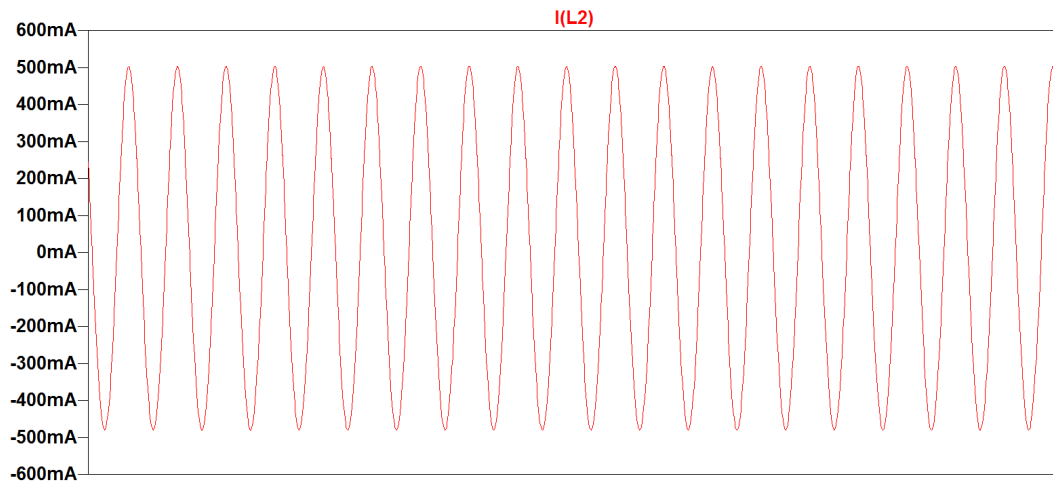


Figure 3.6: Almost pure coil current with 1MHz frequency

on the transistor and efficiency drop becomes important. As will be explained in the WPT design section in detail, to solve this problem system operation frequency is changed to achieve optimum operation. Class-E amplifier is needed to be tuned for the new configuration and this is done by applying a switch capacitor array parallel to C2 capacitor. Switching operation is done with Solid State Relays (SSR) to pass the current in two ways, in order to not to disturb the AC current.

3.2 Rectifier Design

Rectifier design is another critical chapter in wireless power transfer process. If the rectifier at the receiver end is not a well-considered solution, the system performance remains average even though the designed WPT system is excellent. To charge the rechargeable battery and supply other system voltages at receiver side DC voltage is required hence the generated voltage/current on receiver coil must be converted to DC.

Rectifier design plays critical role to keep system voltage stable and not to disrupt coil current to continue resonant operation.

Among the rectifier topologies that are investigated, one topology with minimum additional component count is Zero Voltage Switching (ZVS) class-E rectifier in Fig. 3.7. The advantage of this topology is, it only uses one rectifying element (diode)

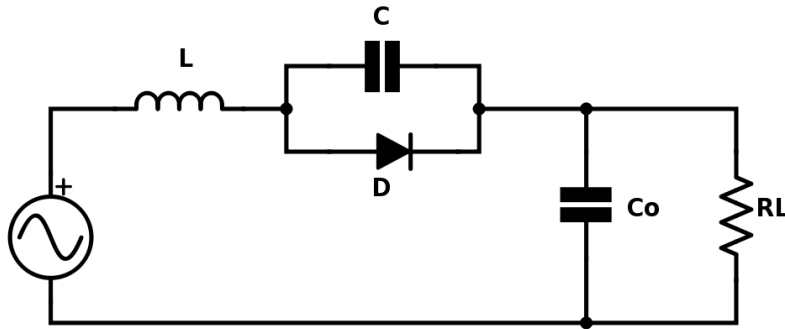


Figure 3.7: ZVS Class-E rectifier

and minimizes the loss on it. However, phase difference between voltage and current on the receiver side disrupts resonant operation and needs compensation on the transmitter(s) side. It would be a problematic solution for variable load system because as the load resistance changes, duty cycle of the rectifying diode changes and phase difference also changes [33].

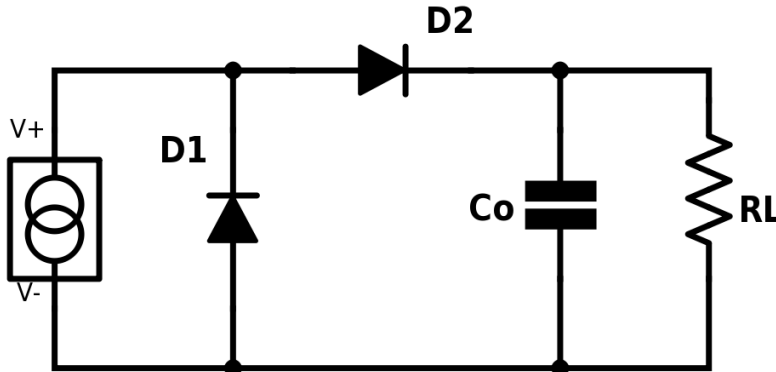


Figure 3.8: Class-D synchronous rectifier

Another rectifier topology with minimal component count is current driven synchronous class-D rectifier as shown in Fig. 3.8. This rectifier topology is proper for resonant operation. By replacing the diodes with transistors it could also be used as a regulator. However diodes turn on and off with high dV/dt which results in high switching noise [34], [35].

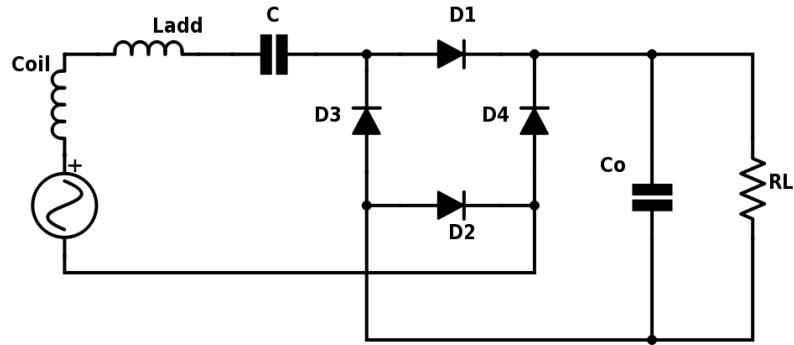


Figure 3.9: Full bridge rectifier

The common choices for the rectifier for implantable devices are full-bridge rectifiers. For that type of rectifier to be efficient the inductance of the coil should be high or load resistance should be small. But for an implantable device because of small geometry constraints inductance can not be high enough and devices perform low current operations. Fig. 3.9 shows full bridge rectifier circuit sourced from a series resonant LC tank. From [36],

- $Q > \frac{2}{\pi}$ for diode to be continuous conduction

- $Q > 2$ for the line current to be nearly sinusoidal (less than 5 percent third harmonic) and power factor to be unity.

Considering the constraints and reasons above, the full-bridge rectifier is considered to be best choice for an implantable device if the coil is supported with additional inductor to increase loaded quality factor.

3.2.1 Rectifier Design Result

Taking into account the WPT design results, a load coil with 1.3 μH inductance is achieved. However for a load resistance of 50 Ω at receiver side results in Q factor of 0.163. This is lower than $2/\pi$ for diodes to be in full conduction mode.

To make line current almost sinusoidal, Q factor should be greater than 2. To achieve this value the load coil inductance need to be higher than 16 μH . Because changing load coil is not an option for optimum WPT operation a discrete inductor series with load coil is used. In this case the additional inductor is required to be low loss and minimum size. Because it is not possible to find an inductor around 15 μH inductance with the given properties a 5.6 μH inductor is used at least to achieve full conduction of diodes.

Designed rectifier is simulated using LT Spice at 1 MHz frequency as shown in Fig. 3.10. In the simulation, 100 $\text{m}\Omega$ coil AC resistance, 800 $\text{m}\Omega$ inductor internal resistance and 50 $\text{m}\Omega$ capacitor parasitic resistance is included. As shown in Fig. 3.11 diode is fully conducting but current in load coil is not a perfect sinusoidal as seen in Fig. 3.12 .

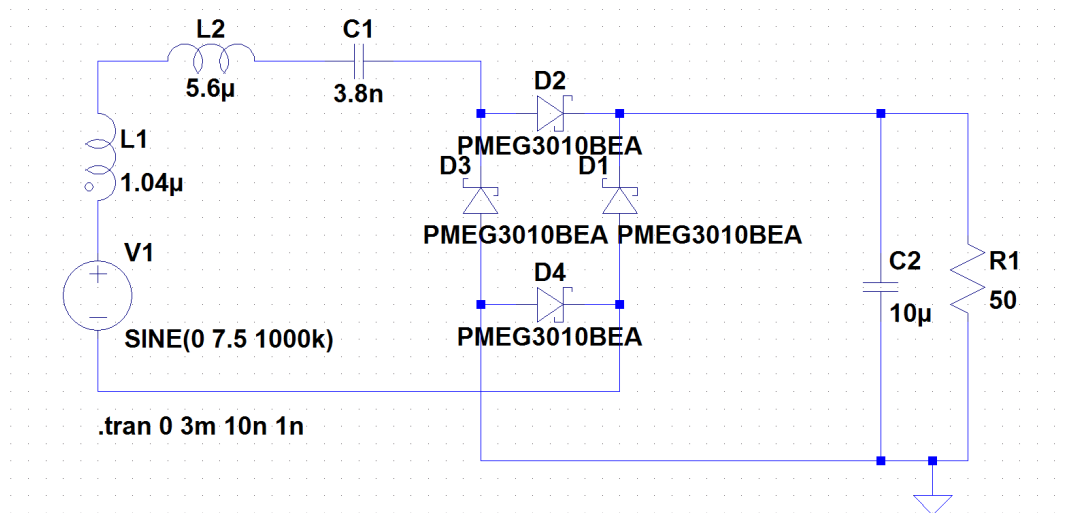


Figure 3.10: Designed rectifier schematic

541 mW power is dissipated on 50 Ω load resistance when the input power of 614 mW is supplied. Efficiency of the rectifier becomes % 88.

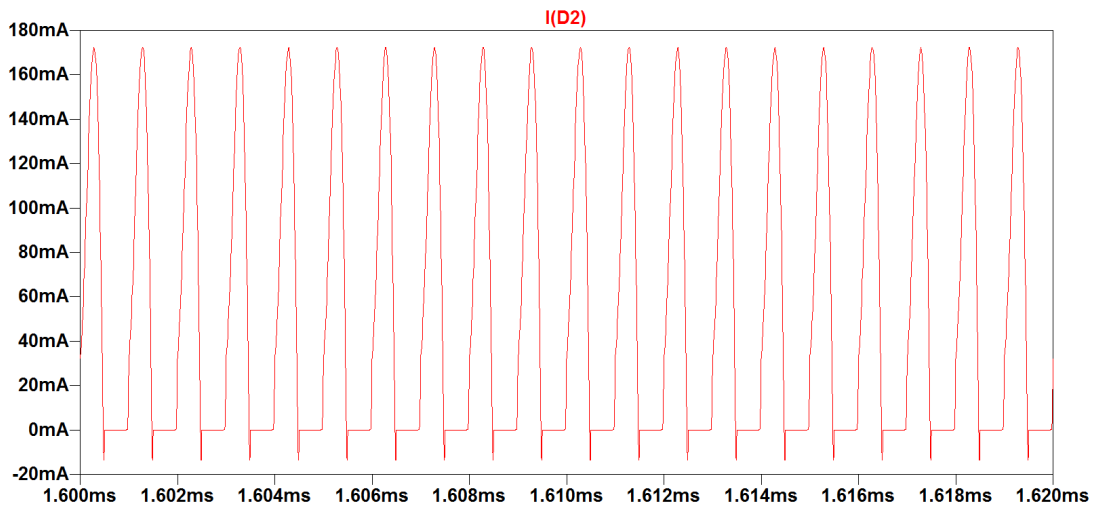


Figure 3.11: Rectifier diode current

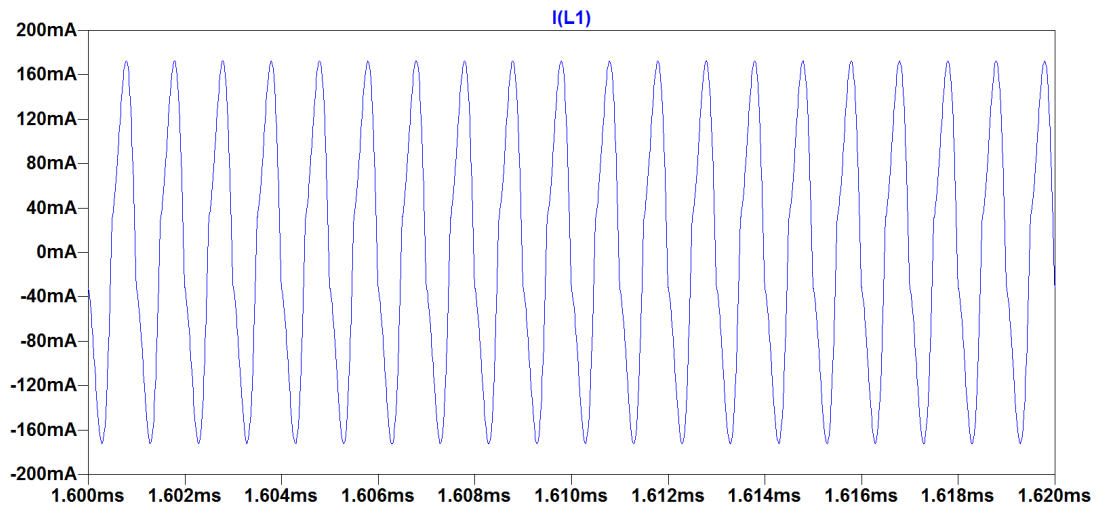


Figure 3.12: Current on the load coil after rectification

CHAPTER 4

WPT DESIGN

Before starting WPT design for maximum efficiency operation, it is necessary to define requirements and develop a design flowchart as shown in Fig. 4.1

As a first step the size of the implanted device determines optimization parameters. Rechargeable stimulator devices' radius changes from (not perfect shape, estimated from base areas) 2,5 cm to 3 cm mostly. To keep the used area minimum in this work, maximum receiver coil radius is selected to be 2 cm. As explained in AC resistance analysis, Litz wire is selected to achieve a high Q receiver coil. For Litz wire to be efficient against eddy current losses skin depth of copper at that frequency should be smaller than the strand diameter [37]. Litz wires are manufactured up to 46 AWG (40 μm) in strand diameter but are produced on demand (due to high manufacturing costs). Therefore wires with 44 AWG (51 μm) strand diameter with different strand counts are used for optimization. Therefore the skin depth at maximum frequency becomes $\delta_{f_{max}} = 51 \mu\text{m}$

The frequency corresponding to this skin depth value is calculated as 1.67 Mhz. The system is not forced up to limits and by giving 10% tolerance, 1.5 MHz is selected as the upper frequency.

The critical part in the frequency selection process is that, it should not generate excessive tissue losses for patient safety.

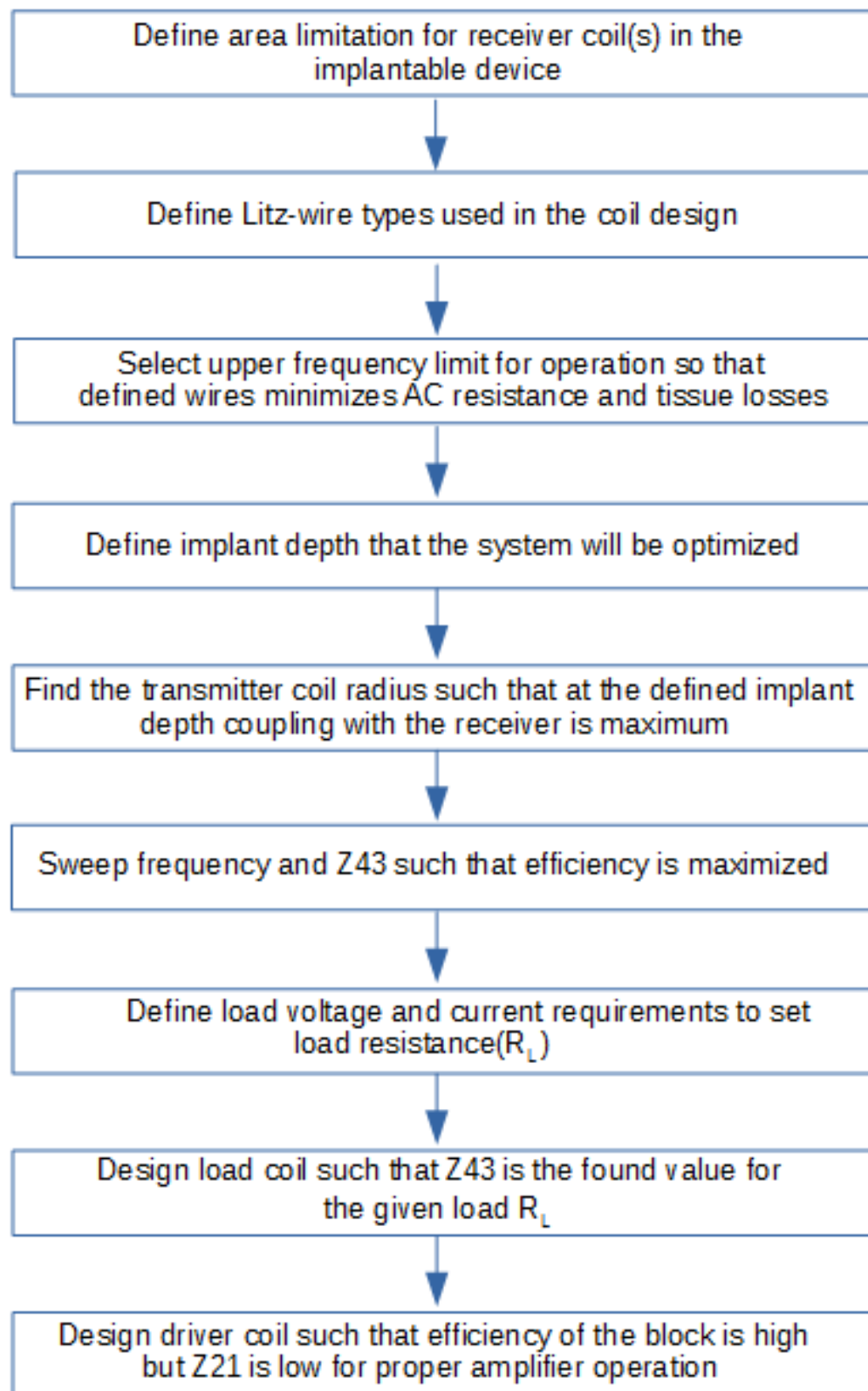


Figure 4.1: Wireless power transfer design procedure

When tissues, skin, fat and muscle are investigated up to 1.67 Mhz, it is seen that muscle has the highest conductivity (conduction losses) and skin has the highest loss tangent. But the losses are negligible up to a maximum frequency of 1.67 Mhz. Fig. 4.2 and Fig. 4.3 shows the conductivity and relative permittivity of muscle, skin and fat up to 1.5 MHz.

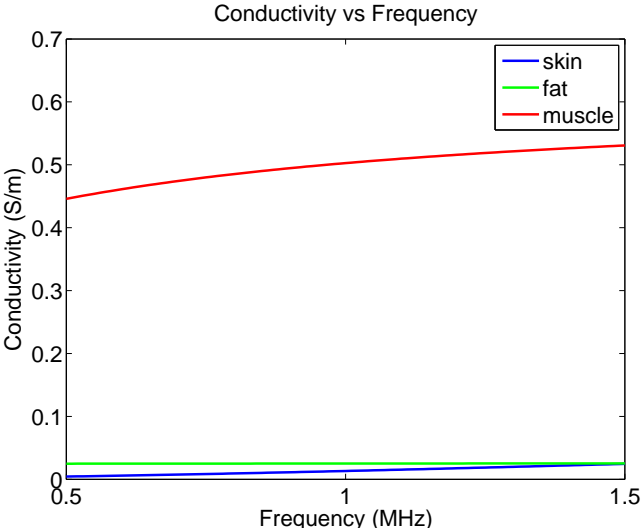


Figure 4.2: Tissue conductivities vs frequency

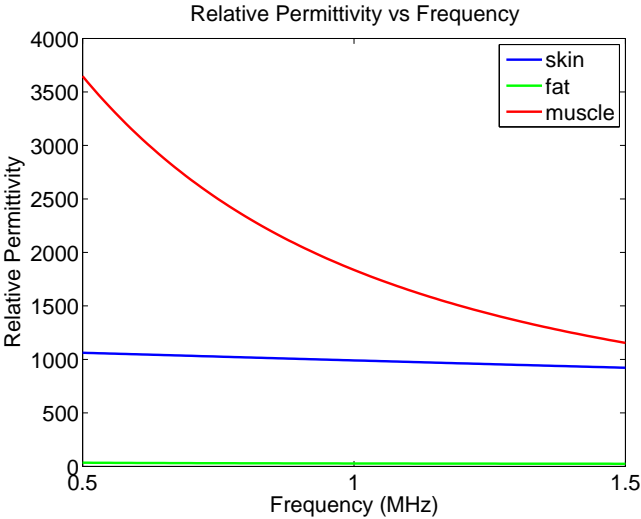


Figure 4.3: Tissue relative permittivity vs frequency

Rechargeable implantable devices’ maximum implant depth are up to 2-2.5 cm for most of the devices due to WPT limits. The depth was up to 4 cm for non-rechargeable devices and in this study implant depth is selected as 4 cm.

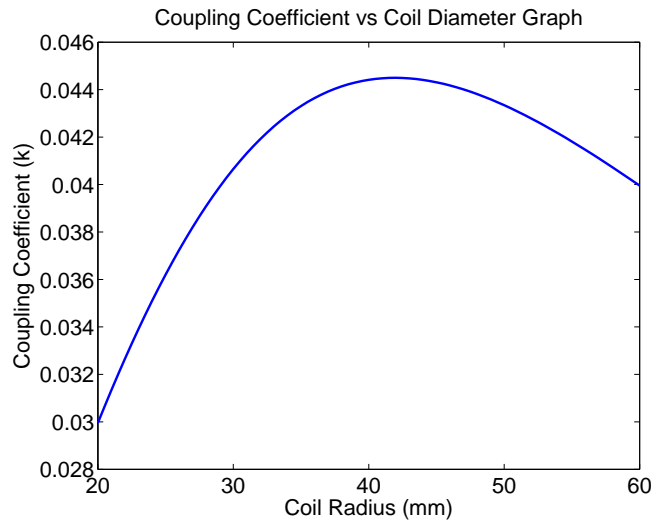


Figure 4.4: Coupling coefficient k for different coil radiuses at 4 cm distance

After selecting the maximum implant depth, transmitter coil radius should also be defined before optimization procedure. It is the radius that generates maximum coupling with the receiver coil at a given implant depth. Magnetic coupling coefficient (k) is a parameter that depends only on the physical constraints. Although the coupling coefficient depends on the number of turns, k factor between single turn coils gives the right result. Therefore single turn transmitter with a receiver of 2 cm radius is investigated. The distance between coils are assumed as 4 cm. Fig. 4.4 shows the graph of k as a function of transmitter coil radius. Results show maximum coupling occurs when the transmitter coil radius is 4 cm.

After setting the size restrictions' to start the design, an optimization procedure should be defined. SCMR power transfer method uses the load coil (coil 4) to transform optimum load to receiver coil (coil 3). In the same manner the driver coil (coil 1) is used to maintain the optimum load to the power amplifier.

In the center of the design, strongly coupled transmitter and receiver coils exist. Therefore after designing these coils it is straightforward to design driver and load coils.

The first thing to decide is the selection of Litz wire type for coils. 4 Litz wire types are ordered for the design as shown in table 4.1.

Table4.1: Litz wire types and corresponding parameters

wire type	strand count	strand diameter(mm)	wire diameter(mm)
Type1	105	0.05	0.511
Type2	255	0.05	0.812
Type3	400	0.05	1.024
Type4	1050	0.05	1.628

Among these wires, Type1 is selected for the receiver coil to minimize coil volume and increase the mutual inductance with the transmitter coil. For the external coil there is no strict volume requirement and it is more critical to design a low loss coil to increase power efficiency. Therefore, Type3 and Type4 wires are candidates for transmitter coil wire type but Type3 is selected to increase power amplifier quality factor (because smaller wire diameter increases turn number).

Note: For 4-coil SCMR design, power amplifier is connected to the driver coil (coil 1) not transmitter coil (coil 2). But the design implemented in this thesis has a 3-coil structure finally due to adaptive operation requirements.

2 unknown critical parameters; frequency of operation and reflected load from the load coil to the receiver coil Z_{43} remain.

Table4.2: Optimization parameters

parameter	range	step
frequency	[800-1200] KHz	100 KHz
Z_{43}	[2-8] Ohm	500 mOhm

Parameters in Fig. 4.2 are swept with the given step sizes to find the best pair that provides maximum power transfer efficiency in the given ranges. The result is shown at graph 4.5. From the results it is observed that as frequency increases, efficiency increases slightly and reaches a maximum for Z_{43} is greater than 4 Ω .

As a result, the operation frequency is selected as 1 Mhz and Z_{43} as 5 Ω . The slight increase in efficiency above 1 Mhz is ignored because it also results in higher rectifier and amplifier losses.

Efficiency vs Frequency and Load Graph

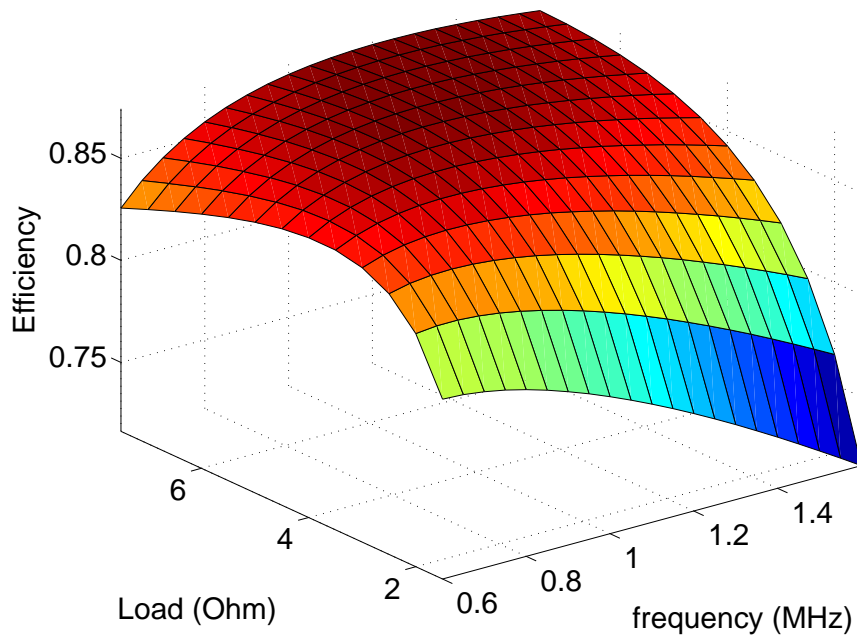


Figure 4.5: Efficiency with frequency and Z_{43}

4.1 Receiver Voltage and Current Requirement Analysis

The system is designed to recharge a battery inside an implantable device. Implantable devices like neurostimulators have 200 mAh to 300 mAh capacity Li-ion batteries. Li-ion batteries have nominal voltage 3.6 to 3.7 V and charged at 4.1 to 4.2 V at maximum. The most suitable charging scheme for Li-ion batteries is constant current/constant voltage (CC/CV) charging due to mainly two reasons [38], [39], [40]:

- degradation in battery capacity is minimum
- increase in life-cycle

The charging rate also effects battery health and lifetime significantly. In [40] it is noted that 0.5 C charging current is suitable for CC/CV charging. Charging a 200 mAh battery with 0.5 C rate corresponds to 100 mA current.

At constant voltage stage, the voltage need to be supplied to battery is 4.2 V. Including the rectifier (300 mV), regulator (200 mV) and battery charger IC (300 mV) voltage

drops, nearly 5V voltage should be maintained.

Therefore load on receiver becomes,

$$R_L = \frac{\text{charging voltage}}{\text{charging current}} = \frac{5 V}{100 mA} = 50 \Omega$$

Consequently, the system could be considered to transfer power to a 50 Ω load.

4.2 Adaptive System Operation

Orientation changes between wireless power transfer coils effect all systems that use magnetic induction method. Due to this fact, coupling coefficient k depends only on the physical placement of the coils, as the relative position between coils changes k changes and mutual coupling changes. As a result of this, reflected impedance changes and system performance show degradation. For a SCMR system, this response is seen more strongly due to existing high mutual coupling.

The system designed is optimized for 4 cm implant depth. But for different patients it could be used at 1 cm depth or more than 4 cm.

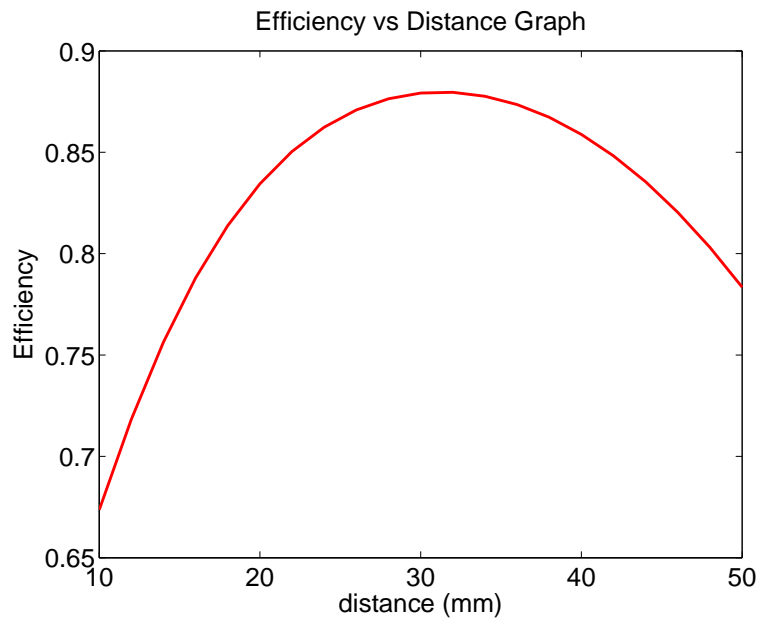


Figure 4.6: Efficiency versus distance graph for the 4 coil system

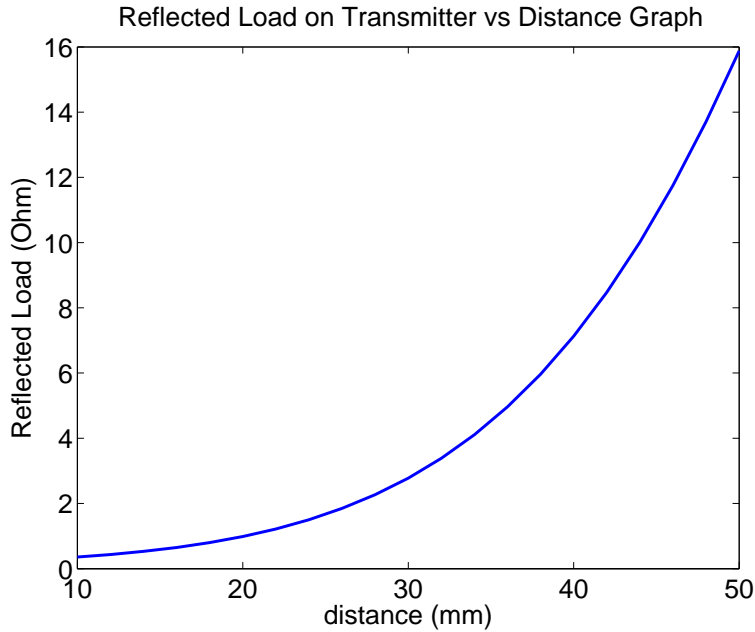


Figure 4.7: Z_{21} versus distance graph for the 4 coil system

Fig. 4.6 and 4.7 show the designed system's efficiency and reflected impedance (Z_{21}) graphs for 1 to 5 cm distance range.

From the graphs it is seen that as the distance between transmitter and receiver coil decreases reflected impedance on the driver coil decreases. As a result efficiency decreases. That behavior could be handled with a higher impedance driver coil. In that case even the reflected load decreases with decreasing distance it would still remain high compared to coil ac resistance and efficiency would not degrade. However a wide load range is not applicable for class-E amplifier. So even though the wireless power transfer efficiency remain stable as coils get closer, it is not possible to drive system due to power amplifier limitations.

To solve this problem, that is keeping the reflected impedance on the driver coil stable as the orientation changes, different methods are presented in literature.

The first one is only applicable for SCMR systems [41]. The method suggest using more than one driver coils with each having different inductance and couplings with the transmitter coil. Only one driver coil is active at a time depending on the transfer distance. The paper does not include a feedback mechanism on changing the driver coils and making it manually. It is therefore not autonomous and has power drops

between driver coil selections. Also due to larger volume requirement on transmitter side the method is not preferred in this design.

The second solution is using buck-boost DC/DC converters at the load side [42]. By controlling the switching the frequency of the converter, the load seen by the receiver coil R_{load} changes and the system response is controlled from the receiver side against placement changes.

For an ideal DC/DC converter input power equals to the output power, i.e.,

$$V_{in}I_{in} = V_{out}I_{out}$$

The impedance seen by the converter output R_L that is, actual load to transmit power is (in our case rechargeable battery and modeled as resistive load),

$$Z_{out} = \frac{V_{out}}{I_{out}} = R_{load}$$

The input impedance of the converter, that is impedance seen by the load coil Z_{in} is,

$$Z_{in} = Z_{out} \frac{V_{in}^2}{V_{out}^2}$$

Therefore for the boost converter as the load seen by load coil decreases, for the buck converter it increases.

This method is a proper alternative for a wireless power transfer system. But for an implantable device the complexity and component cost (both size and count) of the method shows that it is not a good solution.

The third method includes tuning the power amplifier for different operation points by a capacitor array [43]. The solution presented in this thesis uses switch-capacitor array as a way explained below.

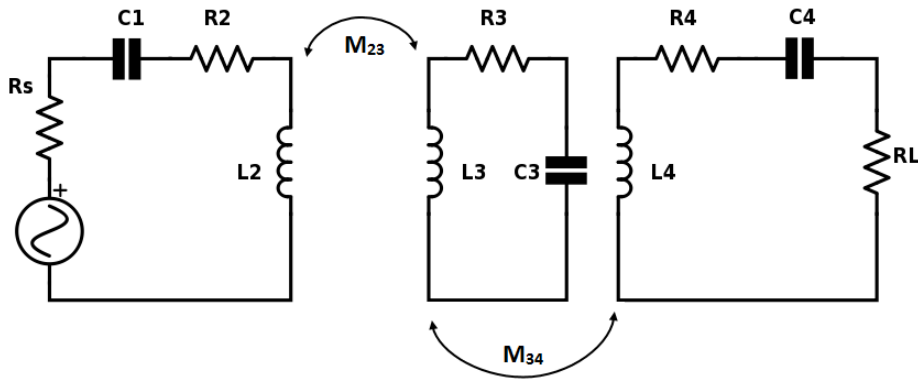


Figure 4.8: Z_{21} versus distance graph for 3-coil system

During the analysis of the SCMR wireless power transfer systems, it is seen that the system could be implemented as a 3-coil system 4.8. Since the loaded Q factor of the transmitter coil is high enough for the class-E amplifier, it could be used as a driver coil. Figures 4.9 and 4.10 show the results of the designed 3-coil system. It is seen that as the distance decreases efficiency increases naturally. But the increase of the reflected resistance (Z_{23}) is dramatic and can not be handled properly by class-E amplifier again.

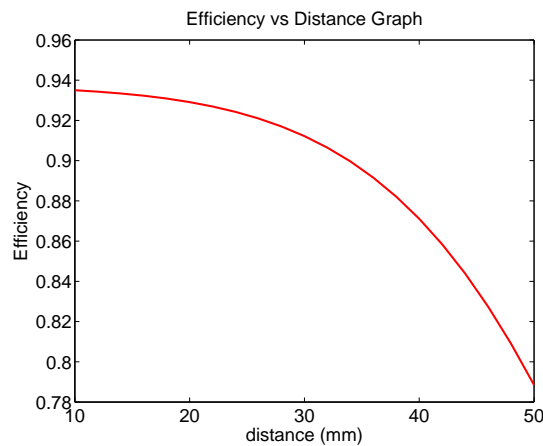


Figure 4.9: Efficiency versus distance graph for 3-coil system

When the system is analyzed in depth, it is seen that reflected load on the transmitter coil could be modified against distance changes by changing the operation frequency. Fig. 4.11, Fig. 4.12, Fig. 4.13 shows efficiency, reflected impedance (real part) and reflected impedance (imaginary) graphs with operation frequencies at 1 cm, 2 cm and 3 cm transfer distances.

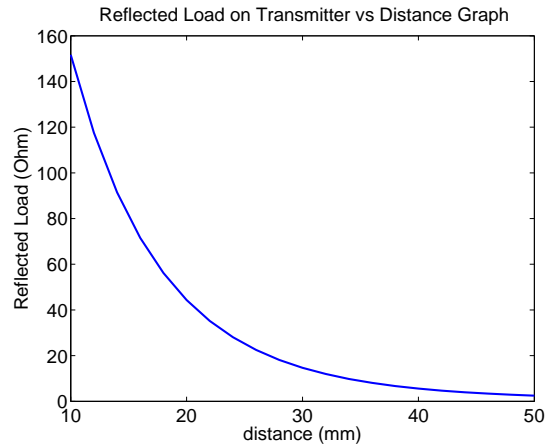


Figure 4.10: Z_{21} versus distance graph for 3-coil system

The graphs show wireless power transfer system, tuned at 1 Mhz, gets into resonance at some lower frequency for different distances with similar loads where the system is tuned for 4 cm. For different implant distances system could be retuned to different operation frequencies by keeping the load resistance stable. Power transfer efficiency also remains stable.

For that purpose, the class-E amplifier is tuned to the new operation frequency [44] by using a switch capacitor array [45].

Besides changing operation frequency to control the WPT system, the supply voltage level on the transmitter side should also be controlled. To achieve this a DAC controlled buck converter is used. By changing the DAC output, feedback of the converter is changed yielding a change in the output voltage level. By using this method, class-E amplifier voltage level can be adjusted between 0 to 5 V with 20 mV steps.

4.2.1 Amplifier Feedback Design

Four feedback mechanisms are performed to detect conditions for an operation frequency change:

- A power monitor device that measures voltage and current values of the supply of amplifier. By reading this voltage and current values, impedance seen by the amplifier supply is calculated and checked whether it is in the proper operation range.

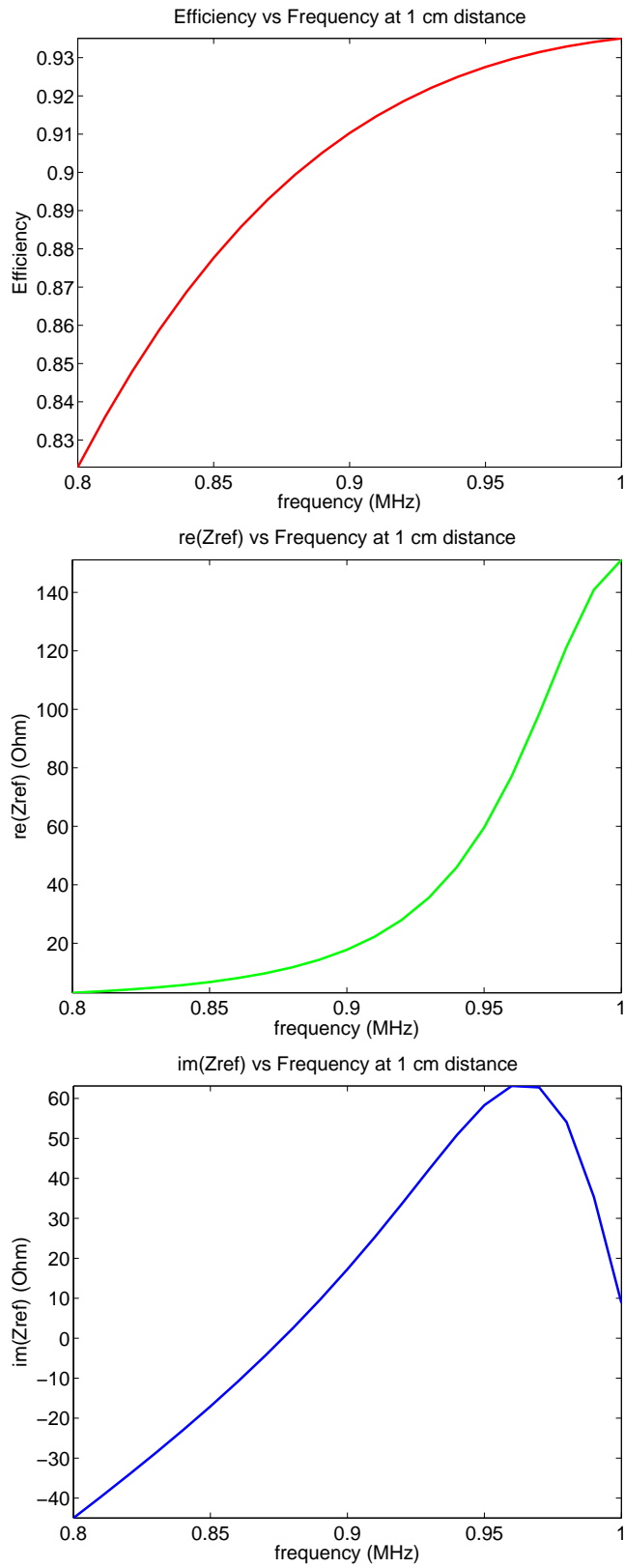


Figure 4.11: 3-Coil design results at 1 cm

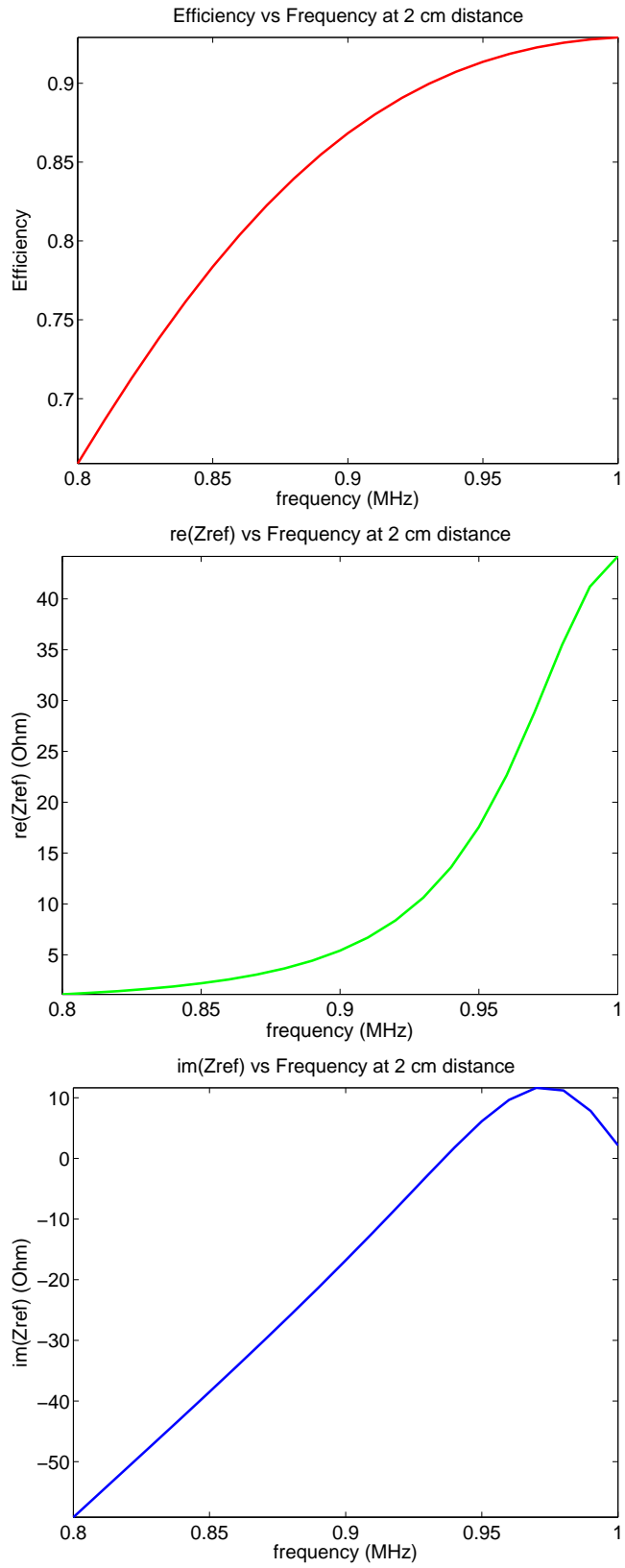


Figure 4.12: 3-Coil design results at 2 cm

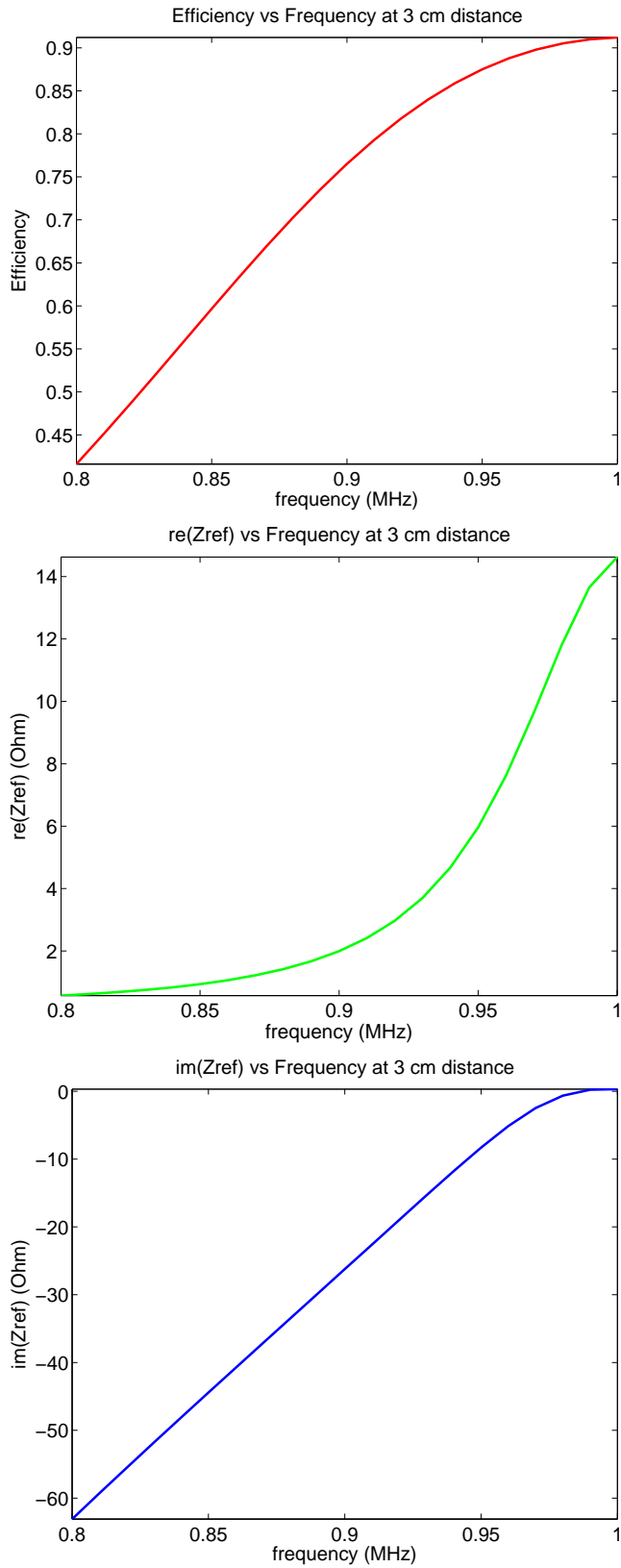


Figure 4.13: 3-Coil design results at 3 cm

- The second method is to check the soft switching structure of the class-E amplifier. If the amplifier is overloaded, voltage remains on the MOSFET transistor when the gate is started to open. When the voltage drops to ground level, nearly 20 ns passes and this hard-switching case should be detected in this interval. To achieve this, an npn BJT transistor driven by a reverse polarity clock signal of class-E amplifier clock signal is used as seen in Fig. 4.14. The voltage on the collector of the transistor is compared with a threshold level. If hard switching exists comparator outputs ns pulses. If this output is sent to microcontroller (MCU) directly, it generates continuous interrupts which is not preferred. Therefore output of the comparator is given to a monostable multivibrator to make pulses longer. In this way MCU can detect this error situation at any time.

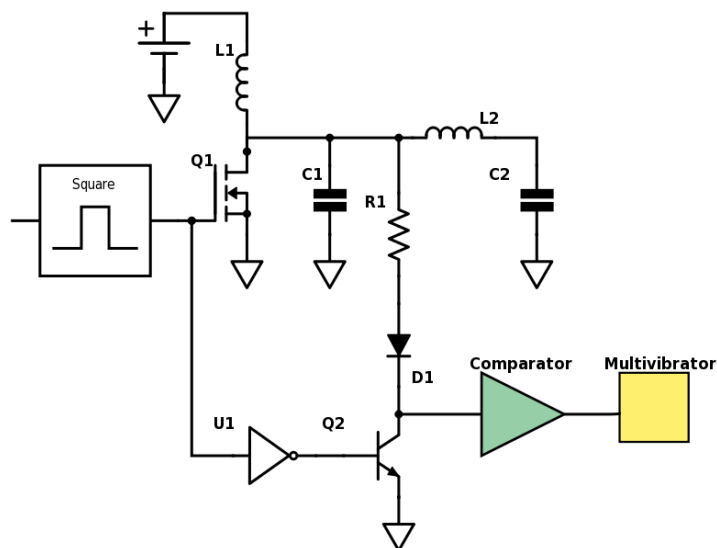


Figure 4.14: Zero voltage switching detection

- The third and critical method is to measure current on the driver coil. In order to achieve this, voltage on capacitor C2 is measured, as shown in Fig. 4.15. A peak detector with time constant 1 ms, much larger than driver clock period(1/1 Mhz) is used. The signal level could be up to 100 V and therefore divided and buffered before sending it to the MCU as an analog input. MCU converts this analog signal to digital form and calculates current on driver coil. Because voltage on the receiver side is also learned from back telemetry, coupling between coils is calculated. By learning coupling coefficient k system is tuned to correct the operating point.

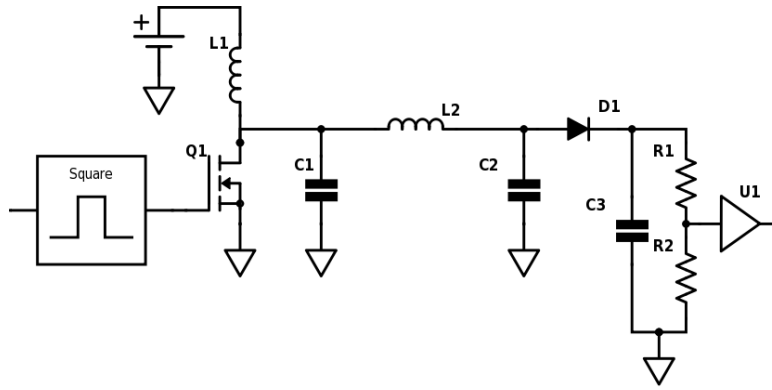


Figure 4.15: Circuit for estimating the transmitter coil current

- The last method is to detect the voltage level on the drain of class-E MOSFET. This is done similarly using with the hardware explained in method 3. Comparing the peak voltage level with the supply level, amplifier operation point is detected [3].

4.3 Numerical Analysis Results

After designing the wireless power transfer system by using analytical model, the results are also confirmed numerically by using COMSOL Multiphysics program. Magnetic and Electric Fields Module and Electrical Circuit Module are used for simulation. Frequency domain analysis at 1 MHz frequency is performed on 2D axially symmetric system.

The system is modeled in AC/AC configuration as in Fig. 2.6. The model is first simulated assuming 4 cm distance between the transmitter and receiver coils (Fig. 4.16). Fig. 4.17 shows magnetic flux distribution of system.

The same system is then simulated in tissue as shown in Fig. 4.18. Tissue is constructed from 4 mm skin, 40 mm fat and 20 mm muscle behind the implant device. Since the device needed to be placed between fat and muscle, to keep implant depth proper fat tissue is kept thicker. Fig. 4.19 shows the magnetic flux distribution of system.

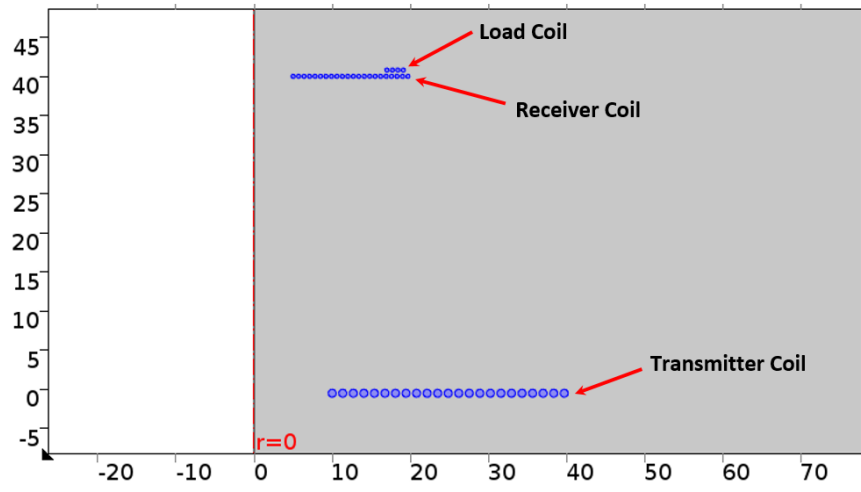


Figure 4.16: Simulation model with air between coils

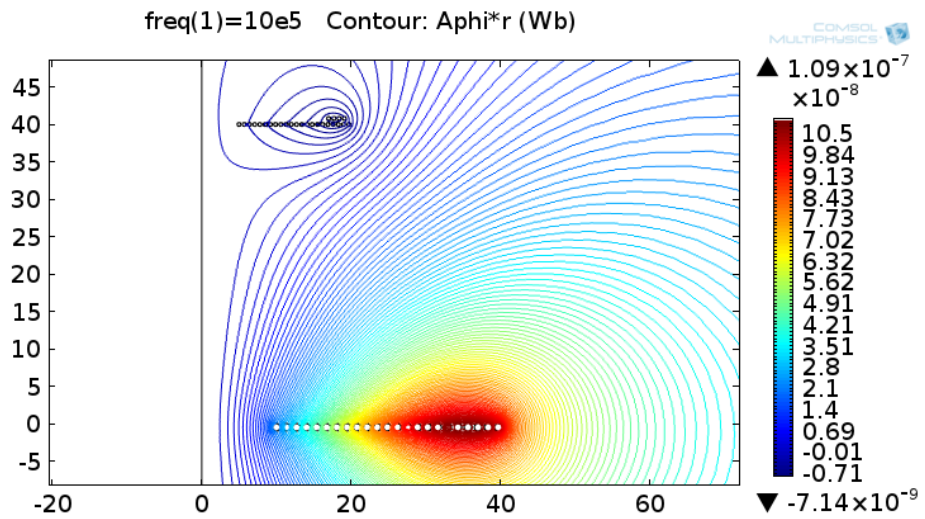


Figure 4.17: Magnetic Flux distribution with air between coils

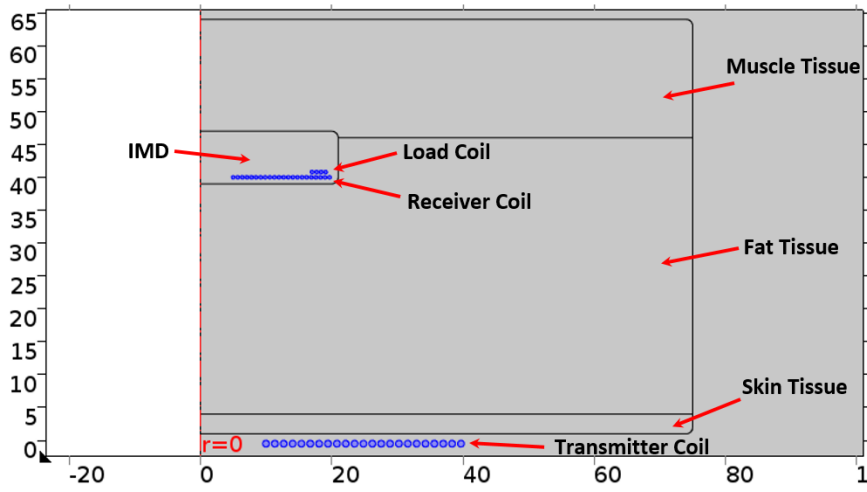


Figure 4.18: Simulation model with tissue

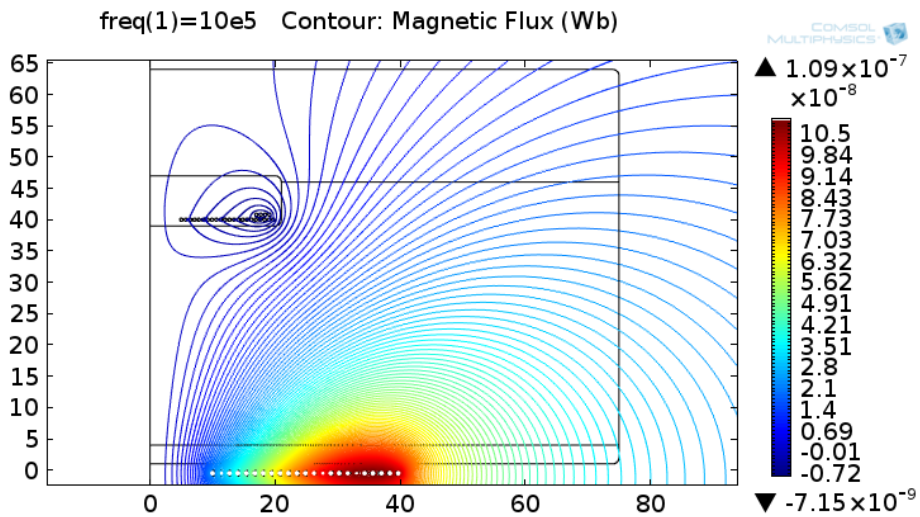


Figure 4.19: Magnetic Flux distribution with tissue between coils

The power transfer efficiency of the air core model is found to be % 85,5 ,while %85 is found in the tissue model. Comparing the efficiency and magnetic flux distribution results, it is seen that operation frequency does not generate excess tissue losses and it is suitable for safe operation.

CHAPTER 5

NEAR FIELD COMMUNICATION

Near field communication (NFC) is a process that performs data transfer over the same electromagnetic waves that transfers wireless power. The main idea to implement this system is to use the wireless power transfer in a controlled way. Data transfer about wireless power transfer related data, makes the system more reliable and safe. The data transfer ability between implantable device and external charger device also removes the need for any other communication channel. By using NFC any data that controls the implantable device could be send and any signal that is monitored could be received.

For the designed NFC system to be practical and reliable, during the data transfer, voltage level on the receiver side should not drop to a level that disturbs power transfer and therefore battery charging operation. To perform the system in this way NFC should not change wireless power transfer efficiency. In addition modulation and demodulation circuits should not be complex so that the hardware used at the receiver side can be minimized due to size requirements.

There are three modulation techniques used for the implementation of near field communication [46], [47],

- 1- Amplitude Shift Keying (ASK)
- 2- Frequency Shift Keying (FSK)
- 3- Phase Shift Keying (PSK)

The choice of modulation technique on the receiver side is more straight-forward. Since the communication is performed over the WPT lines and it is controlled by transmitter side it is not possible to change frequency or phase from the implant (receiver) side. The only way is to change the load seen by receiver coil. This is called Load Shift Keying at some sources but in the end results as a Amplitude Shift Keying.

For the transmitter side all modulation methods mentioned above are possible but the preferred method is again ASK. Since wireless power transfer system designed in this thesis uses resonance FSK decreases WPT efficiency. In addition, since the system is implemented by coils that have high Q factor, it is not possible to have a wide-band system. PSK is a good solution to keep efficiency stable during operation and it is easy to implement on modulation side. However demodulator circuits on the implant side are complex and they are not the best solution unless performing an ASIC design. ASK on the other hand is easy to implement on both the modulation and demodulation side. By keeping the modulation depth small, an NFC system with little power loss during communication could be implemented.

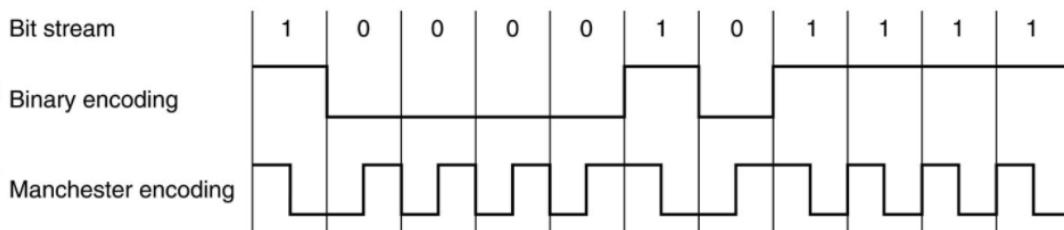


Figure 5.1: Binary Encoding and Manchester Encoding Schemes for the corresponding bit stream

For this half duplex communication system Manchester Encoding (ME) method is selected. Fig. 5.1 shows ME data structure. ME defines low to high transition as bit 0 and high to low transition as bit 1. Therefore both bit 0 and bit 1 includes digital high and digital low signals as a pair with 50 duty cycle but in reversed order. The advantage of using ME - consecutive 0's or 1's does not create different voltage drops depending on the data sent. Whatever the data sent it has 50 percent digitally high and 50 percent digitally low signal. - The pulses inside data is either 1/baudrate or 2/baudrate. That makes the demodulator design easier. If ME was not used pulses of data could be 1/baudrate or 8/baudrate (consecutive 0's or 1's for a byte).

The data transfer is preferred to be implemented over UART interface of microcontroller units. The hardware UART module's inside the MCU transfers the bits of data with a little firmware load. The other way to achieve same result could be using timer module, detecting edges of transitions and decoding data from pulse widths of detected signal. This is a heavy load for an MCU that operates at low clock frequency to not to spend much power.

Baud rate selection primarily depends on the carrier frequency and step response of the class-E amplifier. The rate should be lower than 1/10 of the carrier frequency for proper demodulation. On the other hand for backward telemetry, data should not be lost due to class-E amplifier response and should be smaller than its settling time (step response).

The baud rate selected for NFC operation is 19200 bps (one of standard UART baud rate) considering limitations explained above. That is the modulation signal is about 50 KHz which is small enough to recover data from carrier signal (i.e WPT frequency, between 800 KHz to 1Mhz). In the end due to Manchester Encoding bit rate of the system becomes half of the baud rate, that is 9600 bps.

5.1 Modulator Design

- Modulator Design at the Transmitter Side

The modulator circuit used in transmitter side is shown in Fig. 5.2. Class-E power amplifier is used at the transmitter side to drive the transmitter coil. The load on RC resonant branch of amplifier is 6 Ohm during charging. To get a low modulation depth a 60 Ohm load branch is added to the system. Because UART lines are digitally high while they are not active, newly added load branch is driven by a PMOS inverter.

The diode on load branch is to stop reverse current that passes from body diode of NMOS transistor (the current is AC). Average power transferred during forward telemetry is dropped only 10 percent.

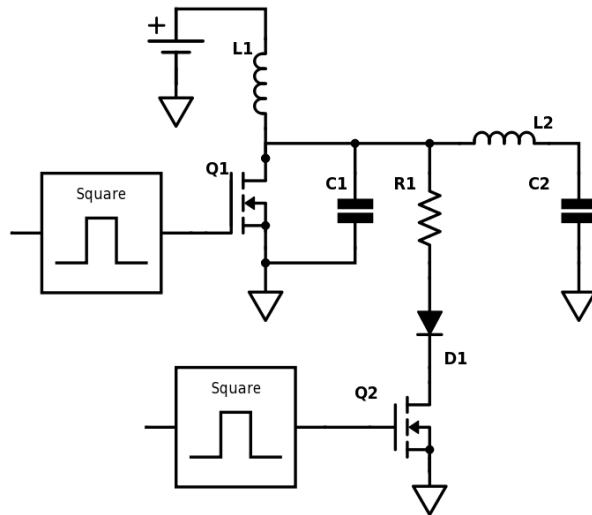


Figure 5.2: Modulator design at the transmitter side

- Modulator Design at the Receiver Side

The modulator circuit used in receiver side is shown in Fig. 5.3. The system is detuned from the resonance frequency during backward telemetry and load shifting to transmitter is changed. Again the detuning branch is driven by PMOS inverter. The modulation is processed from only one edge (signal is still not rectified) not to lose power on other cycle. The capacitor value is chosen such that voltage drop is minimum.

5.2 Demodulator Design

The demodulator circuits for both the transmitter and receiver sides are implemented in a similar structure due to similar modulation structures for both forward and backward telemetry. The only difference happens at the amplifier side because of different signal voltage levels. The ASK demodulator circuit is shown at Fig. 5.4.

While at receiver side demodulator input is taken from the node where inductor and tuning capacitor meets (before signal suppressed by capacitor), at transmitter side demodulator input is taken from the drain node of NMOS transistor.

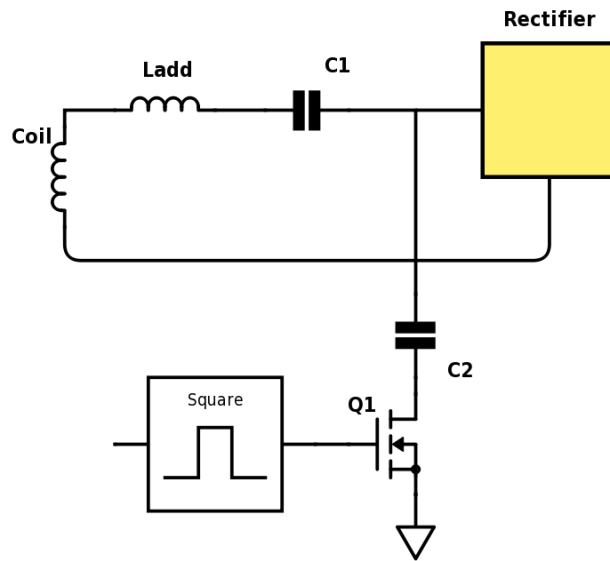


Figure 5.3: Modulator design at the receiver side

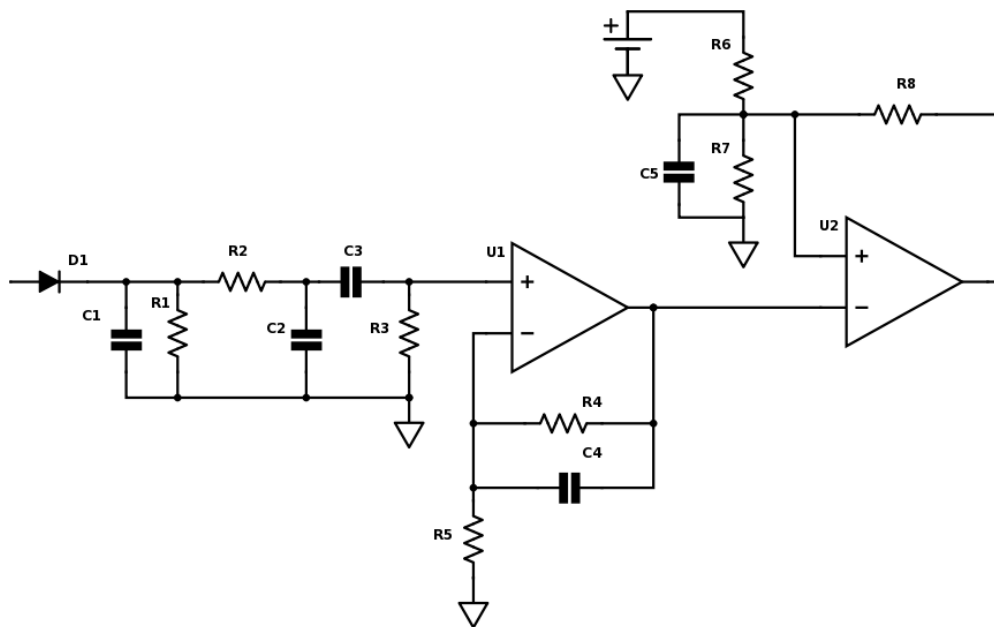


Figure 5.4: Demodulator circuit design

The demodulator consists of several passive elements used for first order filtering of the carrier and DC signal that generates artifacts on the desired modulation signal. The first stage performs a peak detection to catch modulation data (also low pass filtering). For further removal of the out-of-band signal a low-pass filter stage follows the peak detector. That stage is continued with a high-pass filter to remove the DC signal. The obtained signal is amplified and filtered by OPAMP so that the signal level almost reaches to supply rail levels. The final stage is a converter with hysteresis to invert the signal for making it UART compatible.

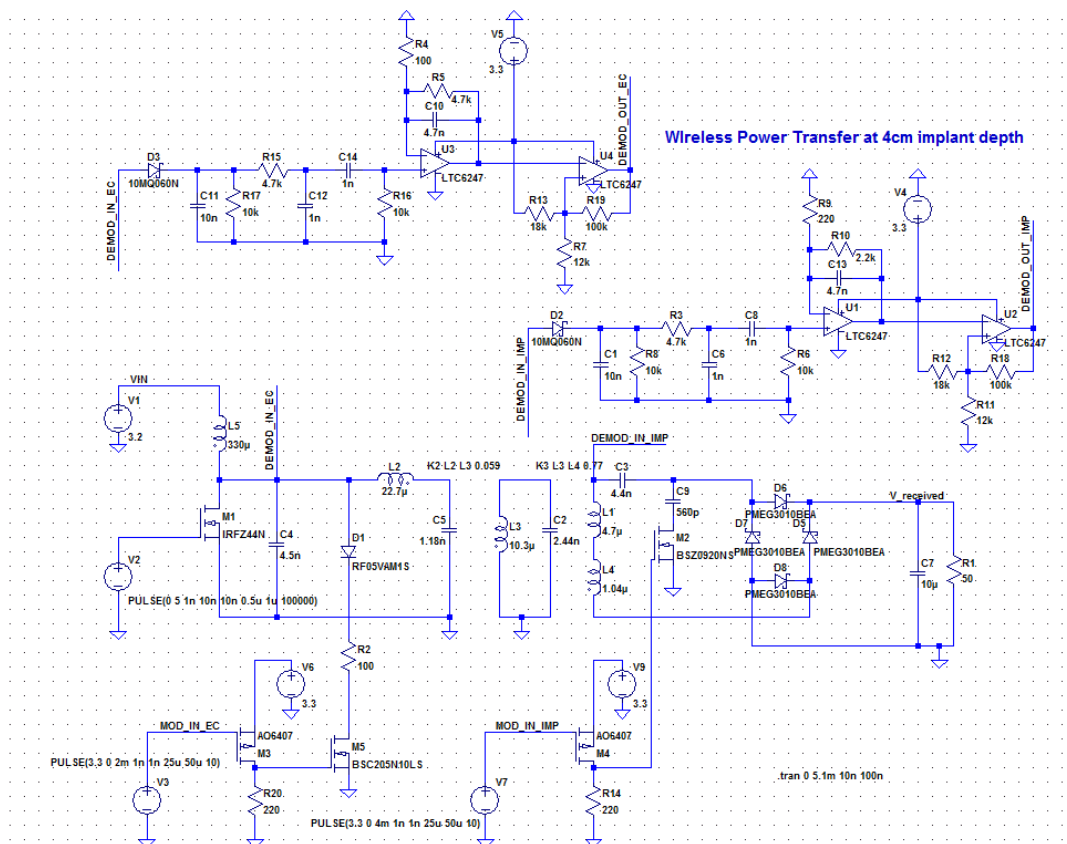


Figure 5.5: Schematic of the complete system designed in LT Spice

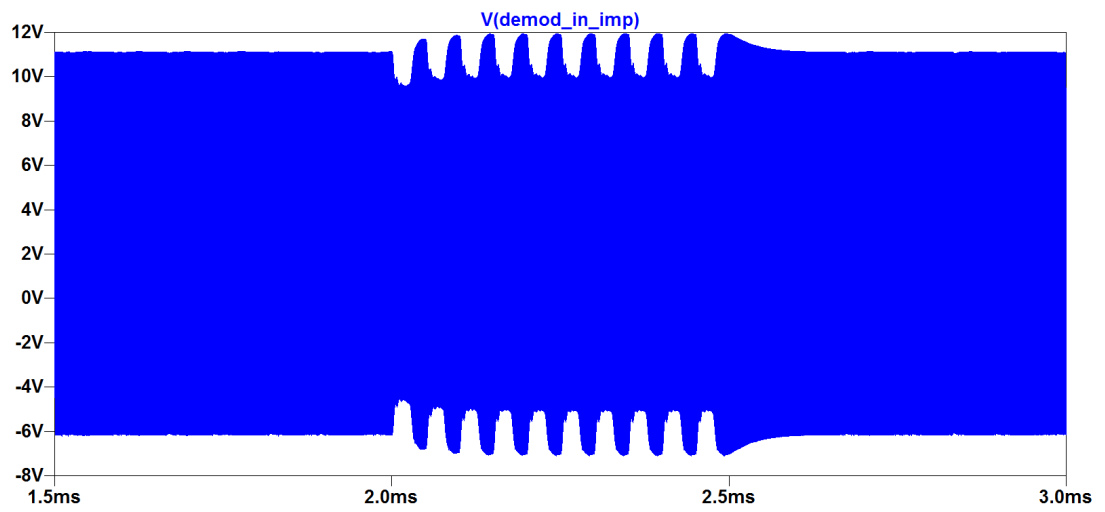
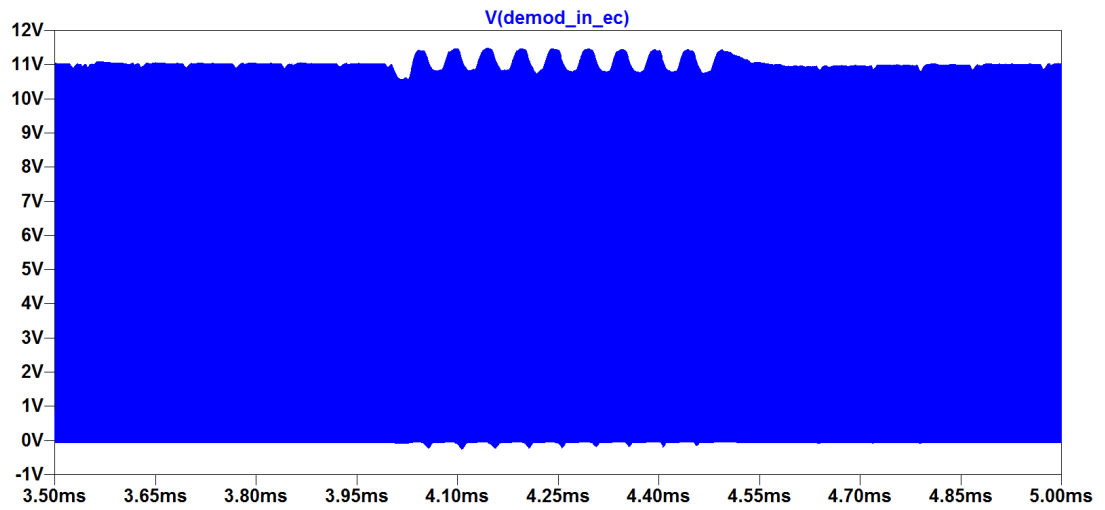


Figure 5.6: Modulated signals on external charger and implant side

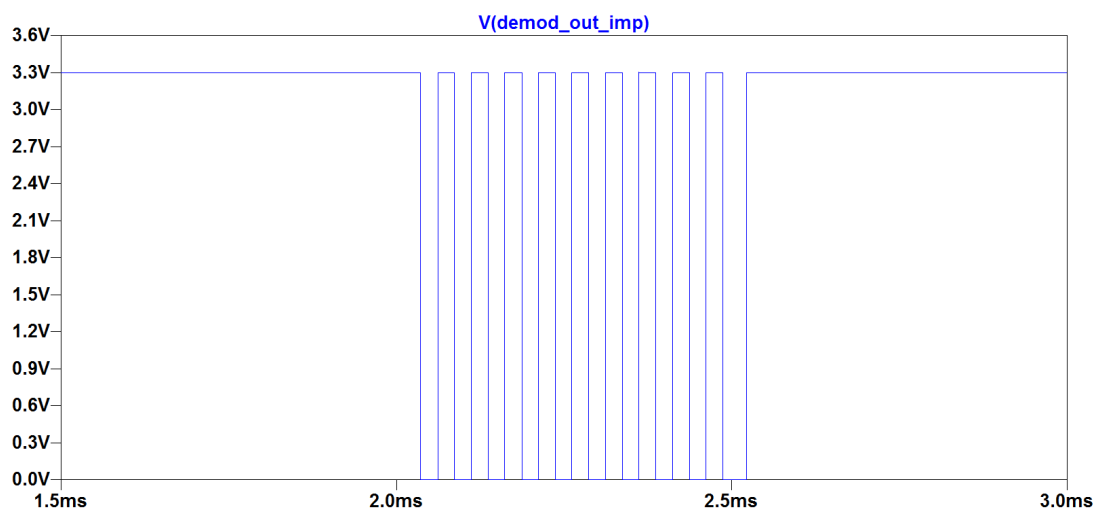
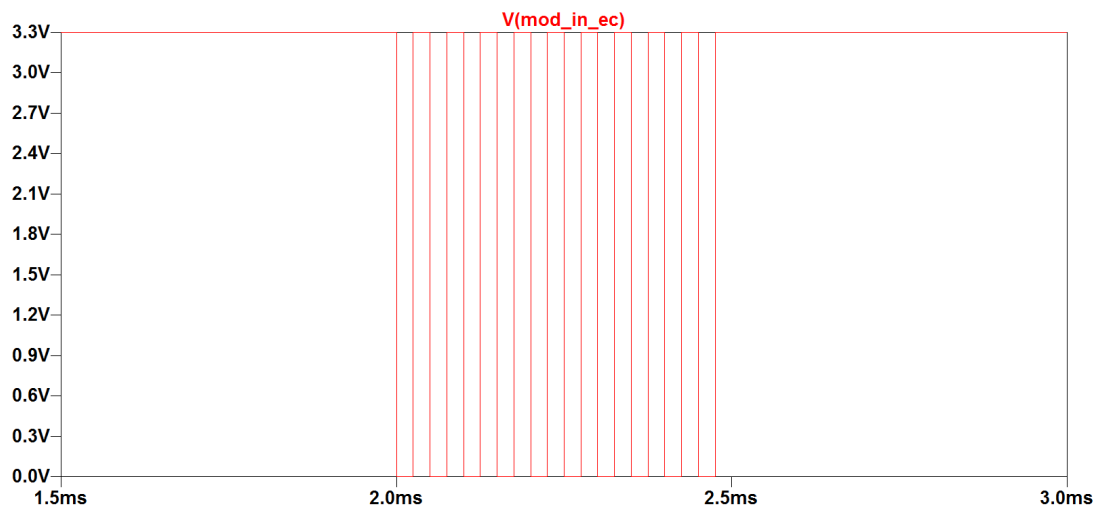


Figure 5.7: Modulation signal from external charger and Demodulated signal at the Implant side

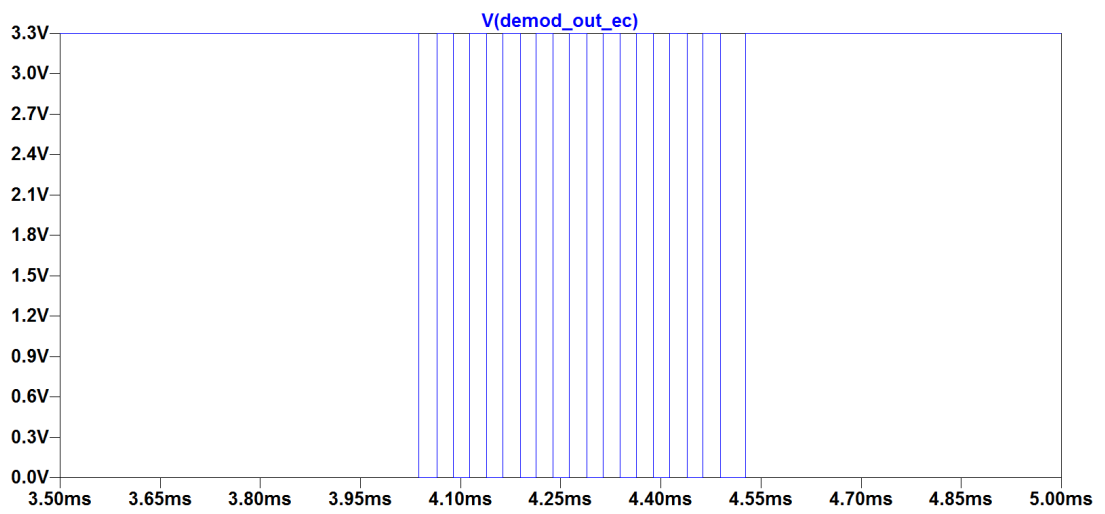
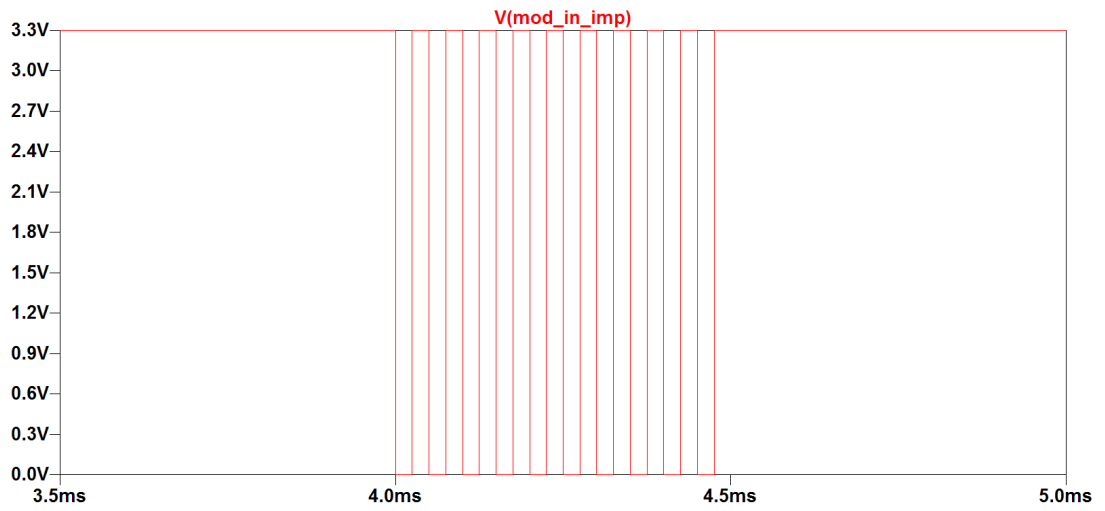


Figure 5.8: Modulation signal from Implant side and Demodulated signal at the external charger side

CHAPTER 6

EXPERIMENTAL RESULTS

Theoretical analysis and the design steps of complete wireless power transfer system for IMDs are presented in the previous chapters. In this chapter practical results of coil design, WPT efficiency and NFC performance are discussed. Fig. 6.1 shows the wound coils and Fig. 6.2 shows the manufactured boards of external charger and implantable device.

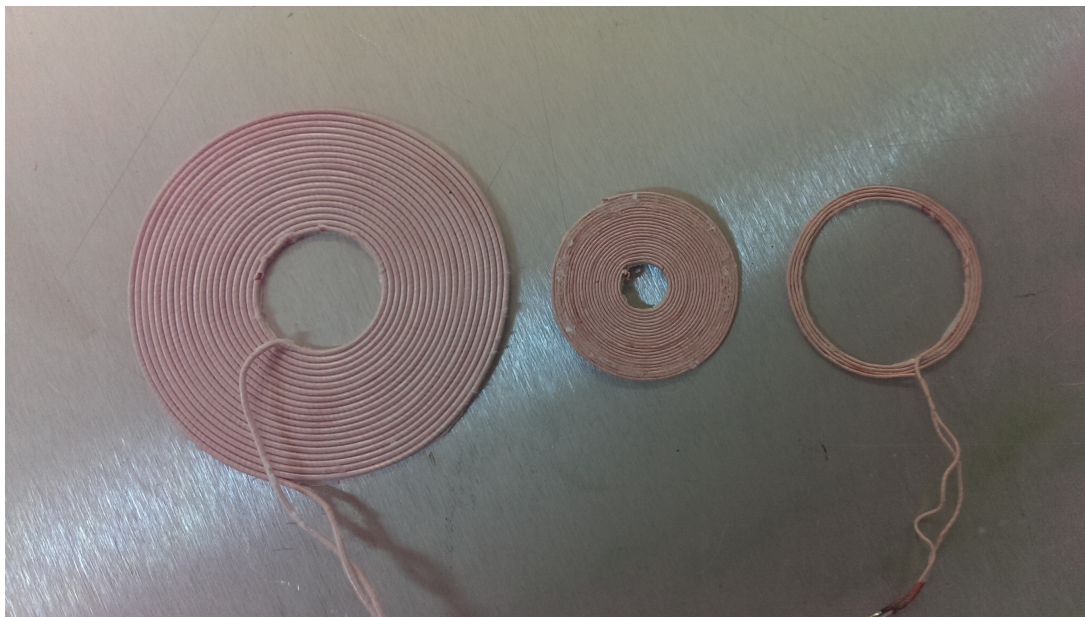


Figure 6.1: Wound coils of WPT system. On left side transmitter coil, on middle receiver coil and on right side load coil

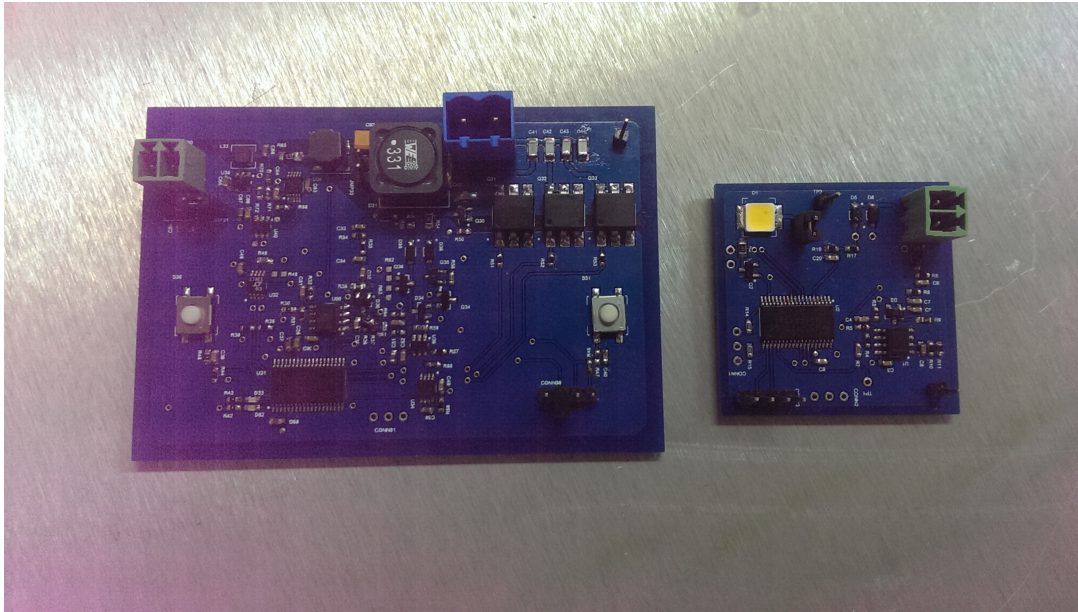


Figure 6.2: Manufactured PCB's for the WPT system. External Charger is on the left and receiver electronics of IMD is on the right

6.1 Experimental Setup

The numerical analysis showed that the system performance is very similar for the cases air between coils and tissue between coils. That is, almost no tissue losses appear during WPT due to low operation frequency. Because of this fact, styrofoam layers, which has same electrical parameters with air, used between coils in experiments as shown in 6.3. In the experiments Agilent E3631A Triple Output DC Power Supply, Agilent 34410A Digital Multimeter and Agilent DSO6014A Oscilloscope are used for supply and measurement devices.

For proper power transfer analysis, DC power supply input of power amplifier at transmitter side is given separately to ignore external charger device internal power consumption. Voltage and current parameters for transmitted power are measured from DC Supply digital screen. For the received power parameters, DC supply is connected directly to rectifier output at the receiver side to check current drawn from the supply at given voltage 4.5 V. At actual WPT operation only rectifier voltage is measured via multimeter. Current drawn at that voltage was already measured.

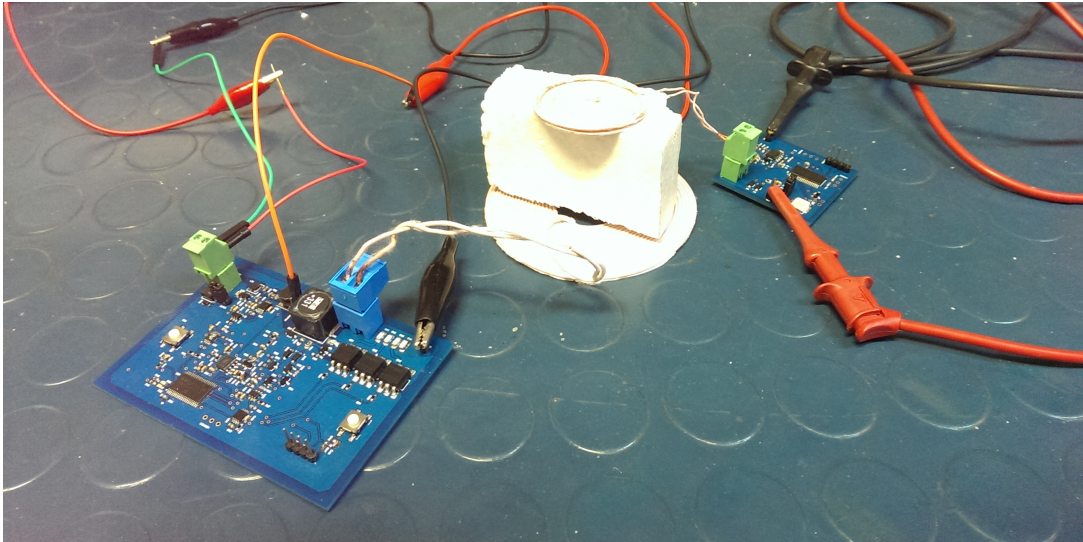


Figure 6.3: Experimental Setup for the system at 4 cm transfer depth

6.2 Coil Parameters

Table 4.15 shows calculated and measured inductance values of the produced planar spiral coils.

Table6.1: Inductance comparison of the coils

coil #	MATLAB	COMSOL	Experimental
Coil 2	22 μH	22.58 μH	21.40 μH
Coil 3	10.4 μH	10.35 μH	11.49 μH
Coil 4	1.04 μH	1.19 μH	1.31 μH

All the inductance values measured experimentally are in close proximity with the MATLAB and COMSOL results. However the reasons for the slight difference are as follows,

- for coil 2, inner side 1 turn is removed for better tuning of the amplifier
- for coil 3, there is 1 mm offset from target radius due to production error
- for coil 4, radius of the coil is increased 1 mm intentionally to achieve the desired Z_{43} value. This is because coil 3 is in very close proximity with coil 4 and coupling coefficient very tolerant to even slight positional variations.

AC Resistance values of the coils for 1 MHz operation frequency are demonstrated in Table 6.2 . Experimental results matches with the results of both methods. The value of Coil 4 shows an increase, due to increased radius of the coil.

Table6.2: AC Resistance comparison of the coils at 1 MHz frequency

coil #	Method 1	Method 2	Experimental
Coil 2	338 $m\Omega$	320 $m\Omega$	342 $m\Omega$
Coil 3	321 $m\Omega$	304 $m\Omega$	303 $m\Omega$
Coil 4	86 $m\Omega$	64 $m\Omega$	109 $m\Omega$

6.3 WPT Power Efficiency Results

The overall WPT system is composed of power amplifier, core WPT system (AC/AC) and rectifier blocks. AC to AC efficiency of the system at 4 cm implant depth was found to be % 85 percent from both analytical and experimental results. At lower depths with decreased operation frequency, amplifier loading was suppressed and WPT efficiency stability maintained. Table 6.3 shows the theoretical results of the efficiency of each system block.

Table6.3: Efficiency of the system blocks expected by design results

Power Amplifier	WPT (AC/AC)	Rectifier	Total Efficiency
% 92	% 85	% 88	% 68

Table 6.4 shows the experimental results for the efficiency of the system for 1, 2 and 4 cm implant depths.

Table6.4: Experimental results of overall wireless power transfer efficiency

Depth	frequency	Source Voltage, Current	Received Voltage, Current	Efficiency
1 cm	880 kHz	% 4.7 V, 180 mA	4.5 V, 108 mA	% 57
2 cm	940 kHz	% 4.25 V, 195 mA	4.5 V, 108 mA	% 58
4 cm	1000 kHz	% 4.76 V, 174 mA	4.5 V, 108 mA	% 58

At all implant distances efficiency values of the complete system are found % 10 lower than the expected design results. Possible reasons are as follows:

- ESR values of the tuning capacitors are higher than the value used in analysis (50 m Ω)
- SSRs used in amplifier side creates additional losses
- Loss of the additional inductor used in the receiver side is more than expected
- 2 % second harmonic on ClassE amplifier current

6.4 Near Field Communication Results

Forward and backward telemetry for 1, 2, and 4 cm implant depths at frequencies of maximum power efficiency is analyzed experimentally. Manchester encoded data pulsed by MCU UART channel at 19200 baud rate is implemented. The data used in operation is one byte 0x8B which appears as two byte 0x9A and 0x65 after Manchester encoding. The data byte is selected such that it has all the combinations of the consecutive digital pulses, 00, 01, 10, 11.

6.4.1 Forward Telemetry Results

Forward telemetry results at 2 cm implant depth are shown in Figures.6.4 - Fig.6.9.

From Fig. 6.8 it is seen that the data is demodulated successfully. At the end of the data UART stop is a little longer than it should be. It may generate problem for data recovery of the final byte of the stream. However with a proper communication protocol that involves byte length in its header the problem is solved easily by MCU by sending extra one byte at the end of the stream. In this way communication becomes more reliable.

Fig. 6.9 shows the rectified voltage variation during data transfer. It is seen that the voltage drop is about 100 mV and it is not critical for proper operation maintenance.

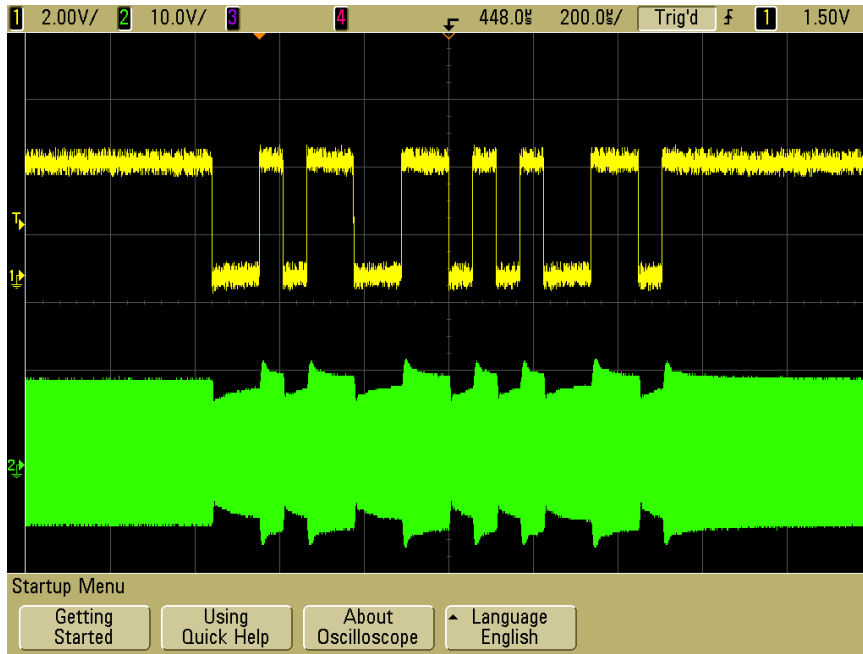


Figure 6.4: Forward Telemetry at 2 cm depth: Yellow trace shows the data modulation signal sent from the external charger side. Green trace shows the variation of the demodulator input signal at the IMD side.

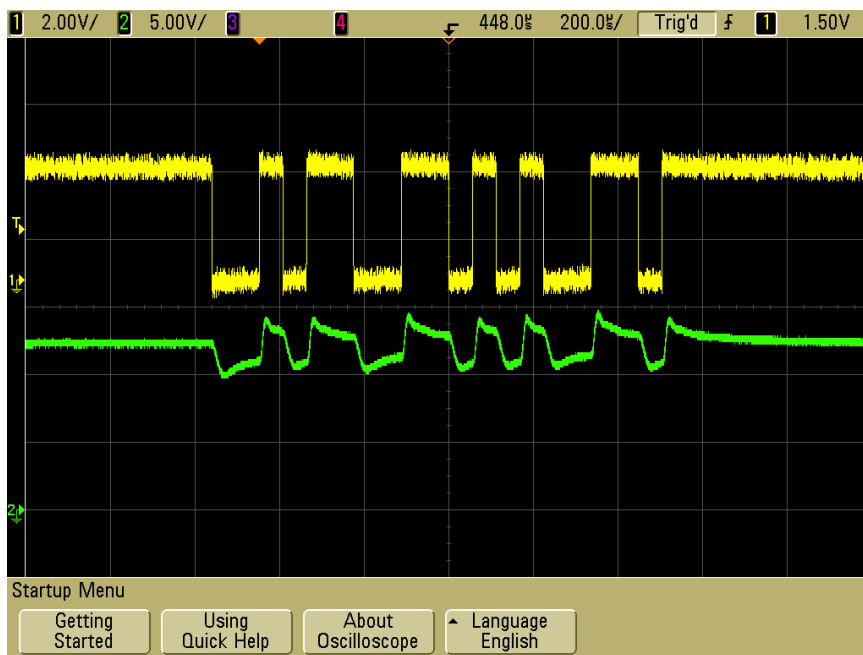


Figure 6.5: Forward Telemetry at 2 cm depth: Yellow trace shows the data modulation signal sent from the external charger side. Green trace shows the low pass filtered output of the peak detector at the IMD side.

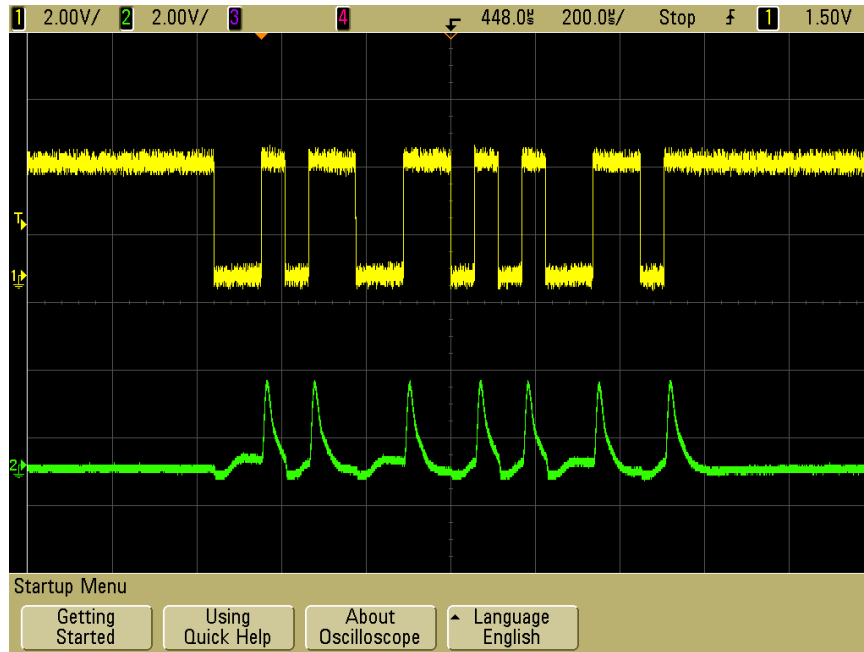


Figure 6.6: Forward Telemetry at 2 cm depth: Yellow trace shows the data modulation signal sent from the external charger side. Green trace shows the high pass filtered signal before amplifier stage at the IMD side.

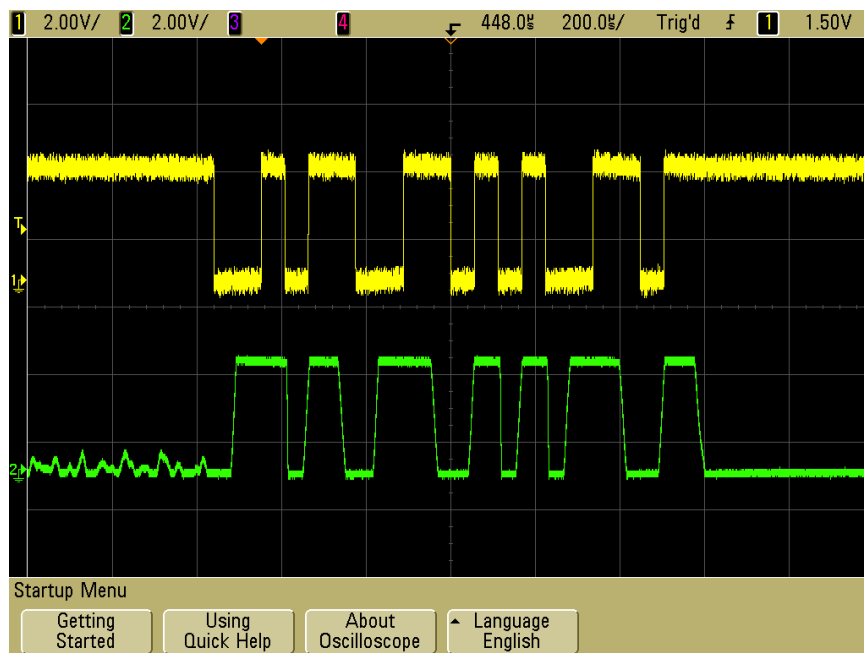


Figure 6.7: Forward Telemetry at 2 cm depth: Yellow trace shows the data modulation signal sent from the external charger side. Green trace shows the amplified signal before inverting comparator at the IMD side.

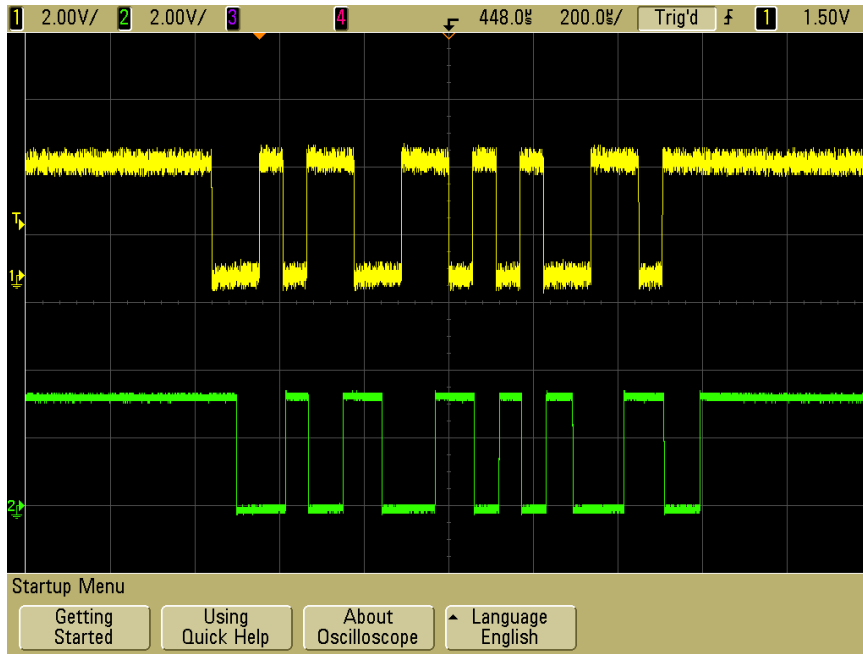


Figure 6.8: Forward Telemetry at 2 cm depth: Yellow trace shows the data modulation signal sent from the external charger side. Green trace shows the demodulated signal at the IMD side.

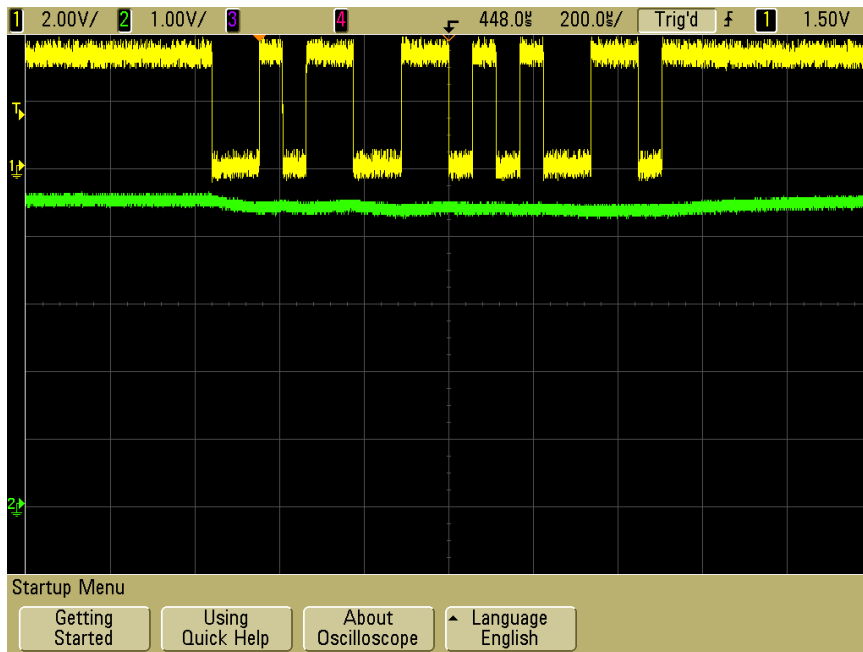


Figure 6.9: Forward Telemetry at 2 cm depth: Yellow trace shows the data modulation signal sent from the external charger side. Green trace shows the rectified voltage variation at the IMD side during data transfer.

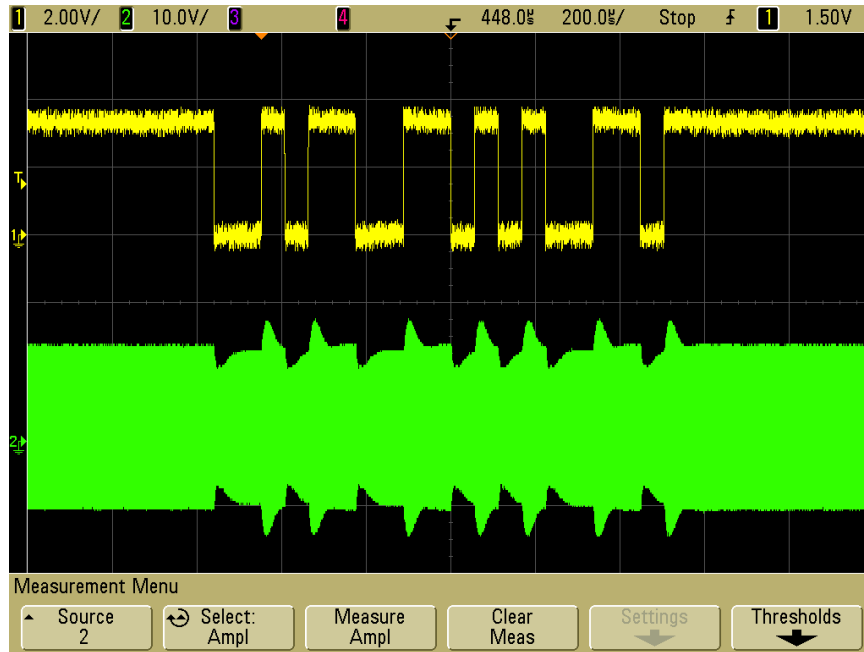


Figure 6.10: Forward Telemetry at 1 cm depth: Yellow trace shows the data modulation signal sent from the external charger side. Green trace shows the variation of demodulator input signal at the IMD side.

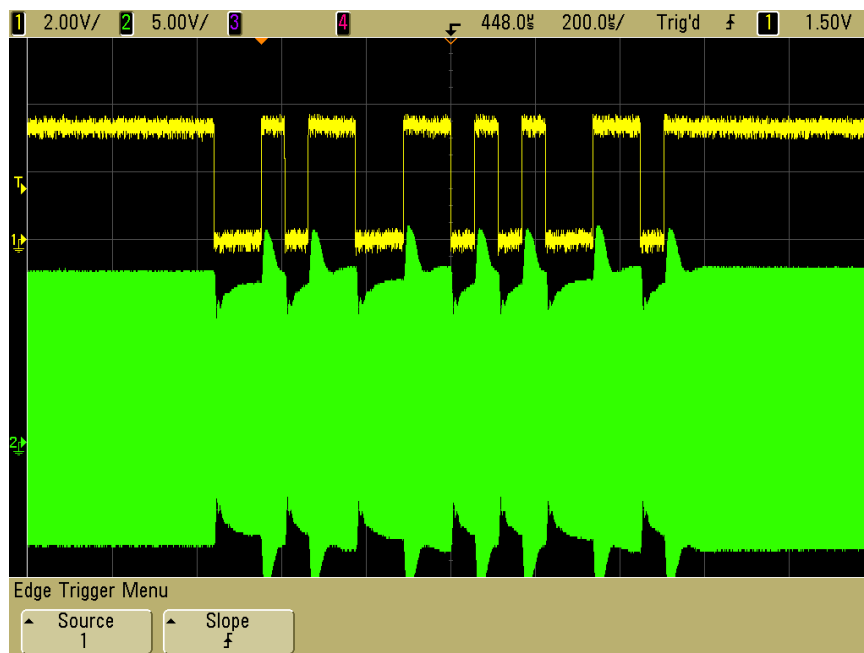


Figure 6.11: Forward Telemetry at 4 cm depth: Yellow trace shows the data modulation signal sent from the external charger side. Green trace shows the variation of demodulator input signal at the IMD side.

Forward telemetry performance at 1 cm and 4 cm implant depths are also analyzed. Fig. 6.10 and Fig. 6.11 shows the demodulator input signal at 1 cm and 4 cm respectively. The signals are also demodulated correctly even with different responses at demodulator input side.

The critical point for the performance of the forward telemetry system is that amplifier should be tuned as close as possible to its ideal value. Otherwise response of the amplifier becomes unpredictable and data can not be recovered correctly.

6.4.2 Backward Telemetry Results

Backward telemetry results at 2 cm implant depth are shown in Fig.6.12 - Fig.6.15.

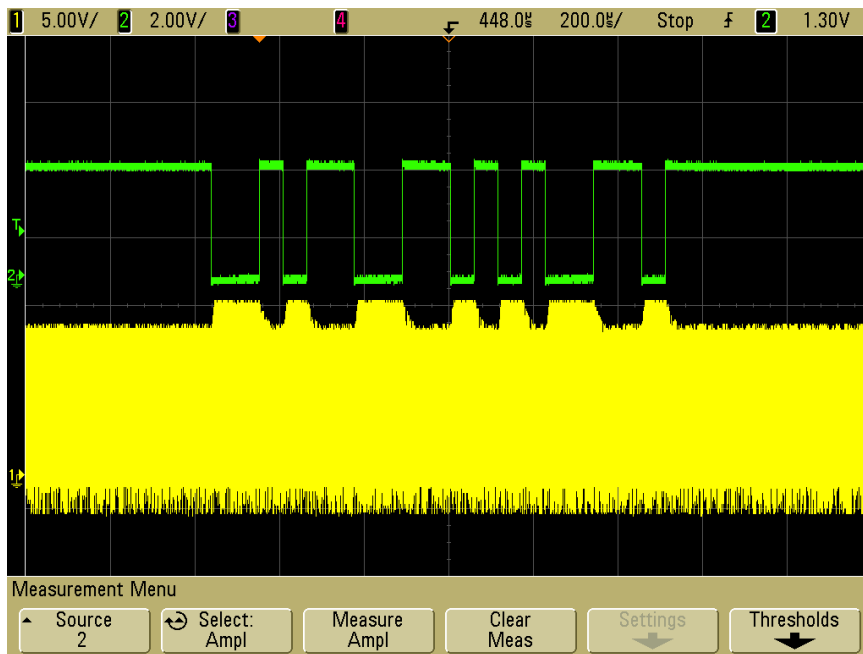


Figure 6.12: Backward Telemetry at 2 cm depth: Green trace shows the data modulation signal sent from the IMD side. Green trace shows the variation of demodulator input signal at the external charger side.

The voltage drop at the rectifier side is 150 mV during backward telemetry as seen in Fig. 6.16 and that drop does not create a problem for charging operation. Small decrease in charge current could occur but it could also be compensated by setting the voltage level with 150 mV margin initially.

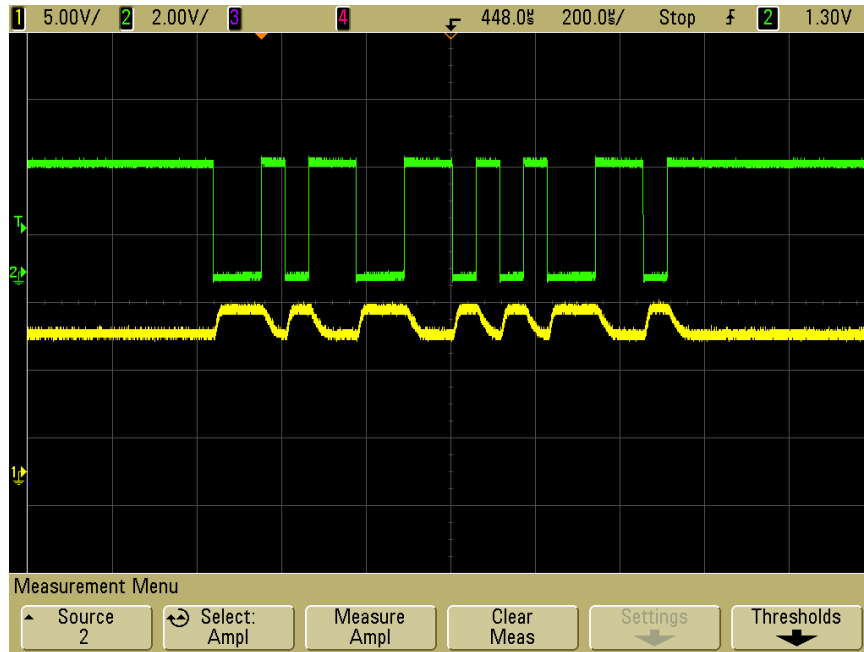


Figure 6.13: Backward Telemetry at 2 cm depth: Green trace shows the data modulation signal sent from at the IMD side. Yellow trace shows the low pass filtered output of the peak detector at the external charger side.

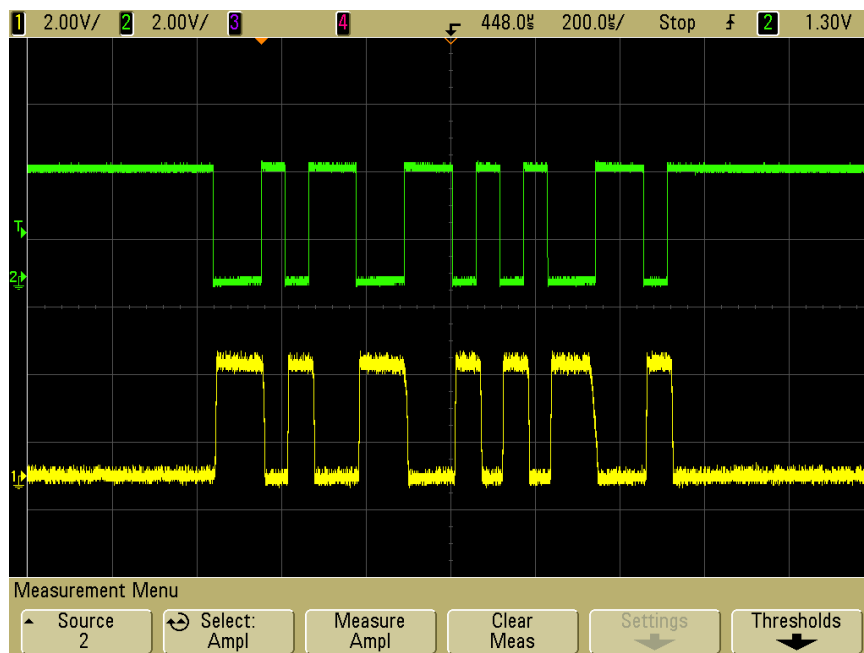


Figure 6.14: Backward Telemetry at 2 cm depth: Green trace shows the data modulation signal sent from the IMD side. Yellow trace shows the amplified signal before inverting comparator at the external charger side.

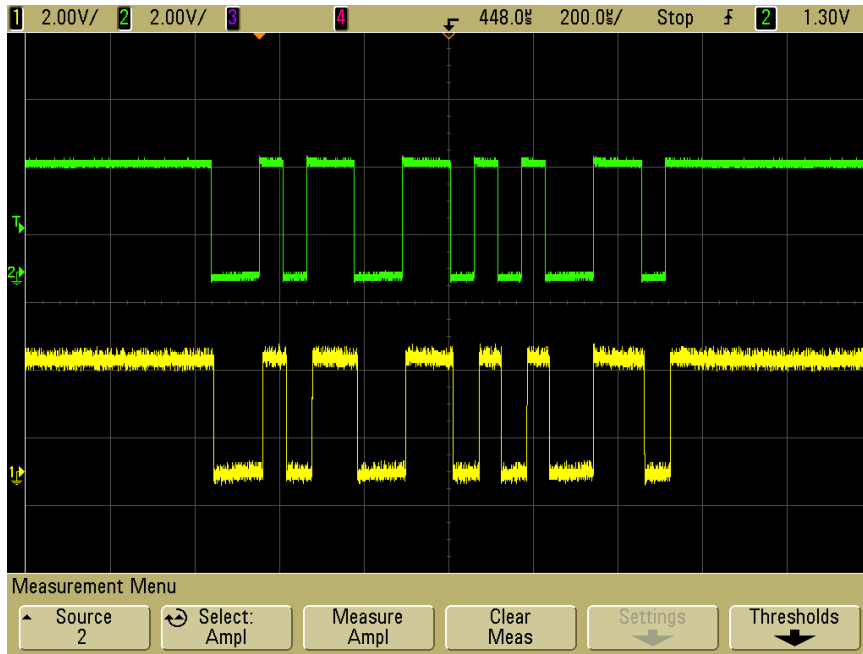


Figure 6.15: Backward Telemetry at 2 cm depth: Green trace shows the data modulation signal sent from the IMD side. Yellow trace shows the demodulated signal at the external charger side.

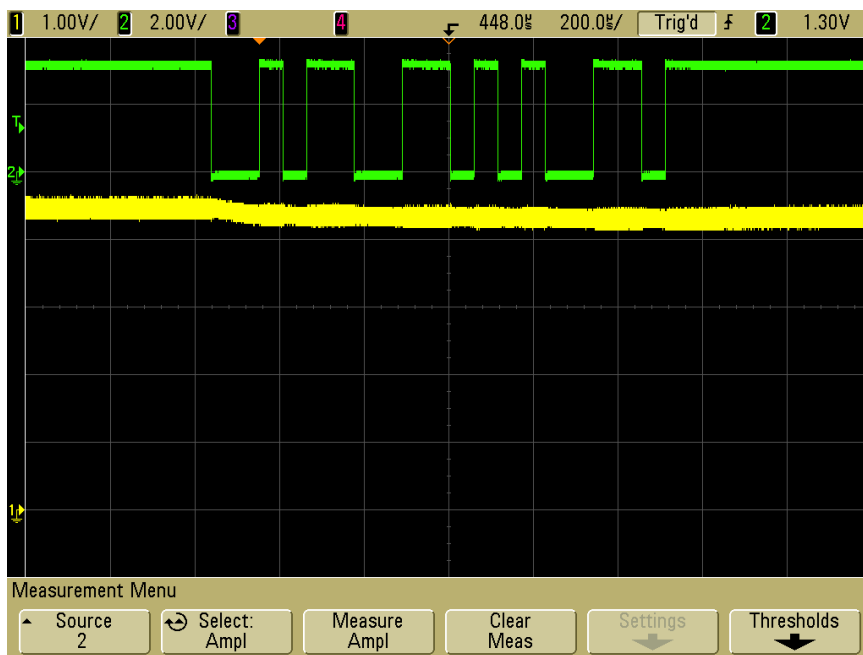


Figure 6.16: Backward Telemetry at 2 cm depth: Green trace shows the data modulation signal sent from the IMD side. Yellow trace shows the rectified voltage variation at the IMD side during data transfer.

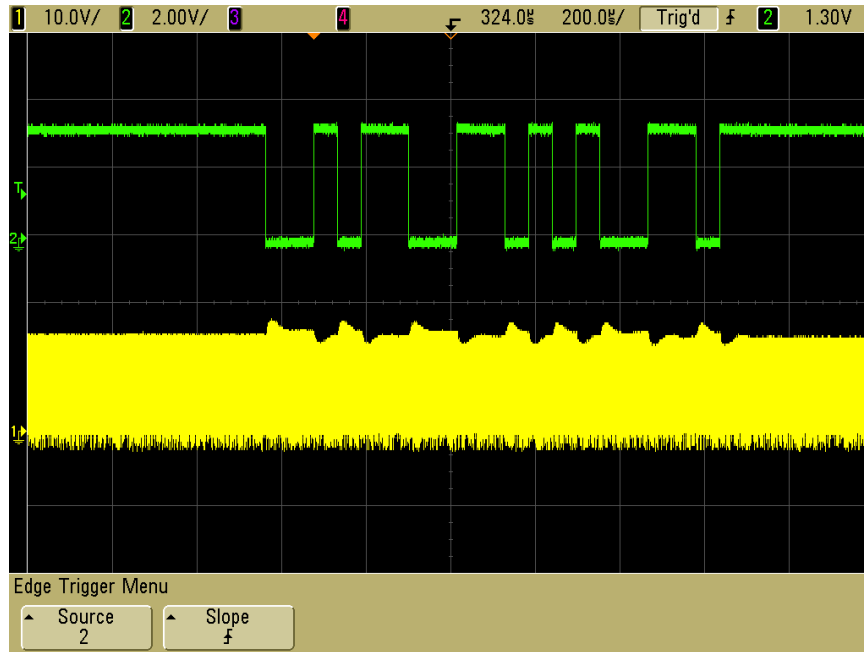


Figure 6.17: Backward Telemetry at 1 cm depth: Green trace shows the data modulation signal sent from the IMD side. Green trace shows the variation of demodulator input signal at the external charger side

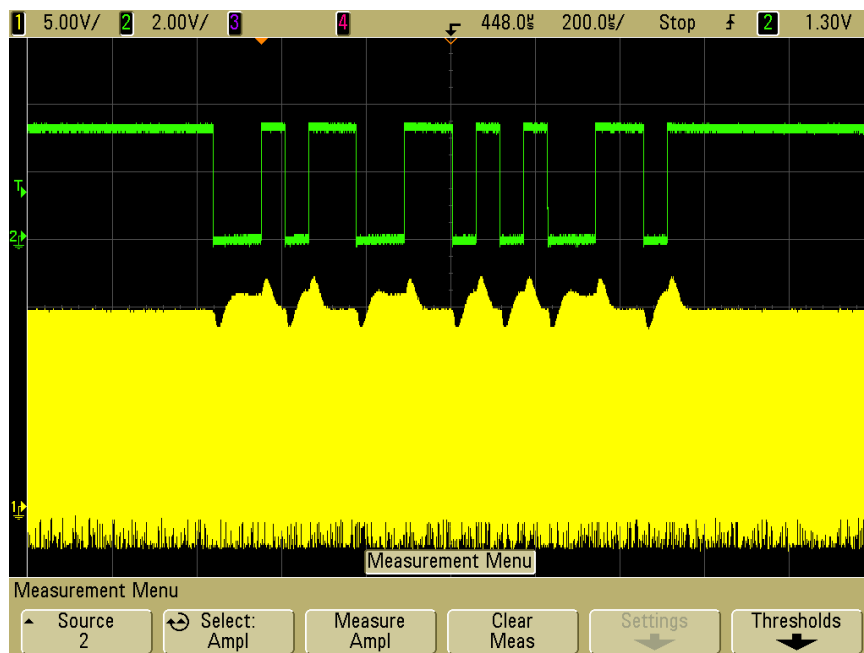


Figure 6.18: Backward Telemetry at 1 cm depth: Green trace shows the data modulation signal sent from the IMD side. Green trace shows the variation of demodulator input signal at the external charger side

Fig. 6.15 shows the demodulated signal output at the external charger side. The data sent from the implant device is demodulated correctly. The behavior of backward telemetry is investigated at 1 cm and 4 cm distances also. Fig. 6.17 and Fig. 6.18 show the demodulator input signal at 1 cm and 4 cm depths respectively. Because the demodulator input signal is taken from the drain of MOSFET of class-E amplifier telemetry performance is strongly related with the amplifier response. As seen its behavior changes at different implant depths. The data is recovered at all cases but when amplifier is tuned perfectly. Therefore as in forward telemetry case amplifier should be tuned correctly to achieve error free data transfer for backward telemetry.

CHAPTER 7

CONCLUSION

In this thesis, analytical, numerical and experimental analysis of wireless power transfer system for implantable medical devices are presented. The aim of the thesis was to investigate higher efficiency WPT system for IMDs to decrease charge time and increase implant depth.

Magnetic induction is the traditional method to transfer power for IMDs. However, the applications of the method is limited to a 2,5 cm implant depth with low power transfer rating because of SAR limitations. In order to improve system performance a novel method, Strongly Coupled Magnetic Resonance [25], was proposed for IMDs and its compatibility was investigated. The method SCMR uses 4 coil system to achieve high efficiency by using high Q factor middle resonators to increase power coupling. High Q factor coil design at implant size is a challenging task and handled by using Litz wires.

In order to make WPT system practical, power amplifier and rectifier stages are discussed and implemented to achieve DC driven and DC ended system. ClassE power amplifier is chosen as the power amplifier due to its high efficiency characteristics and suitable usage for resonance condition. However, the amplifier is not tolerant to significant load changes and needs to be retuned for different operation points. This behavior affected the WPT design methodology significantly. The WPT system was optimized and designed for 4 cm implant depth. But to make the system operate at lower distances (highly increased load coupling) a 3 coil system is implemented by changing the frequency of operation and hence adjusting the amplifier for the new operation point. At 1 cm to 4 cm operation range % 58 overall wireless power transfer

efficiency was achieved.

A near field communication system was also designed to make power transfer in a controlled way and also to transfer data for the IMDs actual operation. Manchester encoded data communication was established at 19200 baud rate for both forward and backward telemetry.

The critical point for the system behavior was the amplifier operation. If it is not tuned correctly, NFC can not be established. Because the received power data is lost at the transmitter side, perfect tuning also not perfectly established with other amplifier feedbacks.

In this thesis a WPT system for biomedical devices with bidirectional telemetry is presented. To improve the performance of the system for realistic applications some points should be analyzed further in the future. They are as follows,

- A smaller strand diameter Litz wire for higher frequency operation could be used to decrease implant coil radius while preserving transfer efficiency
- A smart feedback mechanism to find optimum operation point could be investigated to maintain WPT operation for different implant depths.
- NFC demodulator design and encoding scheme could be improved to be tolerant for untuned amplifier behavior.

REFERENCES

- [1] X. Wei, Z. Wang, and H. Dai, "A critical review of wireless power transfer via strongly coupled magnetic resonances," *Energies*, vol. 7, no. 7, pp. 1–26, 2014.
- [2] F. Tourkhani and P. Viarouge, "Accurate analytical model of winding losses in round litz wire windings," *IEEE Transactions on Magnetics*, vol. 37, pp. 538–543, Jan 2001.
- [3] M. d. Rooij, "Performance comparison for a4wp class-3 wireless power compliance between egan fet and mosfet in a class e amplifier," in *PCIM Asia 2015; International Exhibition and Conference for Power Electronics, Intelligent Motion, Renewable Energy and Energy Management*, pp. 1–8, June 2015.
- [4] J. Kim and Y. J. Park, "Approximate closed-form formula for calculating ohmic resistance in coils of parallel round wires with unequal pitches," *IEEE Transactions on Industrial Electronics*, vol. 62, pp. 3482–3489, June 2015.
- [5] J. F. Patrick, P. A. Busby, and P. J. Gibson, "The development of the nucleus® freedom™ cochlear implant system," *Trends in Amplification*, vol. 10, no. 4, pp. 175–200, 2006.
- [6] K. Agarwal, R. Jegadeesan, Y. X. Guo, and N. V. Thakor, "Wireless power transfer strategies for implantable bioelectronics: Methodological review," *IEEE Reviews in Biomedical Engineering*, vol. PP, no. 99, pp. 1–1, 2017.
- [7] S. Ozeri and D. Shmilovitz, "Ultrasonic transcutaneous energy transfer for powering implanted devices," *Ultrasonics*, vol. 50, no. 6, pp. 556 – 566, 2010.
- [8] "Contents," *Ultrasound in Medicine & Biology*, vol. 43, no. 10, pp. v – viii, 2017.
- [9] A. M. Sodagar and P. Amiri, "Capacitive coupling for power and data telemetry to implantable biomedical microsystems," in *2009 4th International IEEE/EMBS Conference on Neural Engineering*, pp. 411–414, April 2009.
- [10] R. Jegadeesan, K. Agarwal, Y. X. Guo, S. C. Yen, and N. V. Thakor, "Wireless power delivery to flexible subcutaneous implants using capacitive coupling," *IEEE Transactions on Microwave Theory and Techniques*, vol. 65, pp. 280–292, Jan 2017.
- [11] J. S. Ho, S. Kim, and A. Poon, "Midfield wireless powering for implantable systems," vol. 101, pp. 1369–1378, 06 2013.

- [12] L. Marnat, M. H. Ouda, M. Arsalan, K. Salama, and A. Shamim, "On-chip implantable antennas for wireless power and data transfer in a glaucoma-monitoring soc," *IEEE Antennas and Wireless Propagation Letters*, vol. 11, pp. 1671–1674, 2012.
- [13] X. Luo, S. Niu, S. L. Ho, and W. N. Fu, "A design method of magnetically resonating wireless power delivery systems for bio-implantable devices," *IEEE Transactions on Magnetics*, vol. 47, pp. 3833–3836, Oct 2011.
- [14] S. Bhuyan, S. K. Panda, K. Sivanand, and R. Kumar, "A compact resonance-based wireless energy transfer system for implanted electronic devices," in *2011 International Conference on Energy, Automation and Signal*, pp. 1–3, Dec 2011.
- [15] R. F. Xue, K. W. Cheng, and M. Je, "High-efficiency wireless power transfer for biomedical implants by optimal resonant load transformation," *IEEE Transactions on Circuits and Systems I: Regular Papers*, vol. 60, pp. 867–874, April 2013.
- [16] A. K. RamRakhyani and G. Lazzi, "Multicoil telemetry system for compensation of coil misalignment effects in implantable systems," *IEEE Antennas and Wireless Propagation Letters*, vol. 11, pp. 1675–1678, 2012.
- [17] H. Hu and S. V. Georgakopoulos, "Wireless powering of biomedical implants by conformal strongly coupled magnetic resonators," in *2015 IEEE International Symposium on Antennas and Propagation USNC/URSI National Radio Science Meeting*, pp. 1207–1208, July 2015.
- [18] A. K. RamRakhyani, S. Mirabbasi, and M. Chiao, "Design and optimization of resonance-based efficient wireless power delivery systems for biomedical implants," *IEEE Transactions on Biomedical Circuits and Systems*, vol. 5, pp. 48–63, Feb 2011.
- [19] D. Cheng, *Field and wave electromagnetics*. The Addison-Wesley series in electrical engineering, Addison-Wesley Publishing Company, 1989.
- [20] E. Purcell, *Electricity and Magnetism*. Electricity and Magnetism, Cambridge University Press, 2013.
- [21] T. Sun, X. Xie, and Z. Wang, *Wireless Power Transfer for Medical Microsystems*. Springer-Verlag New York, 1 ed., 2013.
- [22] K. Finkenzeller, *RFID Handbook: Fundamentals and Applications in Contactless Smart Cards and Identification*. Wiley Publishing, 2nd ed., 2003.
- [23] Y. H. Kim, S. Y. Kang, S. Cheon, M. L. Lee, J. M. lee, and T. Zyung, "Optimization of wireless power transmission through resonant coupling," in *SPEEDAM 2010*, pp. 1069–1073, June 2010.

- [24] A. Karalis, J. Joannopoulos, and M. Soljačić, “Efficient wireless non-radiative mid-range energy transfer,” *Annals of Physics*, vol. 323, no. 1, pp. 34 – 48, 2008. January Special Issue 2008.
- [25] A. Kurs, A. Karalis, R. Moffatt, J. D. Joannopoulos, P. Fisher, and M. Soljagic, “Wireless power transfer via strongly coupled magnetic resonances,” *Science*, vol. 317, pp. 83–86, July 2007.
- [26] A. Bodrov and S. Sul, *Analysis of Wireless Power Transfer by Coupled Mode Theory (CMT) and Practical Considerations to Increase Power Transfer Efficiency*. INTECH Open Access Publisher, 2012.
- [27] M. Kiani and M. Ghovanloo, “The circuit theory behind coupled-mode magnetic resonance-based wireless power transmission,” *IEEE Transactions on Circuits and Systems I: Regular Papers*, vol. 59, pp. 2065–2074, Sept 2012.
- [28] C. M. Zierhofer and E. S. Hochmair, “Geometric approach for coupling enhancement of magnetically coupled coils,” *IEEE Transactions on Biomedical Engineering*, vol. 43, pp. 708–714, July 1996.
- [29] G. Y. W. Luo, Q. Ke and K. Yang, “Analytical computation of ac resistance of single-layer air-core helmholtz coils,” 2014.
- [30] A. Laskovski, T. Dissanayake, and M. R. Yuce, “Wireless power technology for biomedical implants,” 10 2009.
- [31] N. O. Sokal, “Class-e rf power amplifiers,” 2001.
- [32] N. O. Sokal and A. D. Sokal, “Class e-a new class of high-efficiency tuned single-ended switching power amplifiers,” *IEEE Journal of Solid-State Circuits*, vol. 10, pp. 168–176, Jun 1975.
- [33] A. Ivascu, M. K. Kazimierczuk, and S. Birca-Galateanu, “Class e resonant low dv/dt rectifier,” *IEEE Transactions on Circuits and Systems I: Fundamental Theory and Applications*, vol. 39, pp. 604–613, Aug 1992.
- [34] M. K. Kazimierczuk, “Class d current-driven rectifiers for resonant dc/dc converter applications,” *IEEE Transactions on Industrial Electronics*, vol. 38, pp. 344–354, Oct 1991.
- [35] M. Mikotajewski, “Class d synchronous rectifiers,” *IEEE Transactions on Circuits and Systems*, vol. 38, pp. 694–697, Jul 1991.
- [36] V. Vorperian and R. B. Ridley, “A simple scheme for unity power-factor rectification for high frequency ac buses,” *IEEE Transactions on Power Electronics*, vol. 5, pp. 77–87, Jan 1990.

- [37] C. R. Sullivan and R. Y. Zhang, “Simplified design method for litz wire,” in *2014 IEEE Applied Power Electronics Conference and Exposition - APEC 2014*, pp. 2667–2674, March 2014.
- [38] P. Keil and A. Jossen, “Charging protocols for lithium-ion batteries and their impact on cycle life—an experimental study with different 18650 high-power cells,” *Journal of Energy Storage*, vol. 6, pp. 125 – 141, 2016.
- [39] M. A. Monem, K. Trad, N. Omar, O. Hegazy, B. Mantels, G. Mulder, P. V. den Bossche, and J. V. Mierlo, “Lithium-ion batteries: Evaluation study of different charging methodologies based on aging process,” *Applied Energy*, vol. 152, pp. 143 – 155, 2015.
- [40] S. S. Zhang, “The effect of the charging protocol on the cycle life of a li-ion battery,” *Journal of Power Sources*, vol. 161, no. 2, pp. 1385 – 1391, 2006.
- [41] G. Lee, B. H. Waters, Y. G. Shin, J. R. Smith, and W. S. Park, “A reconfigurable resonant coil for range adaptation wireless power transfer,” *IEEE Transactions on Microwave Theory and Techniques*, vol. 64, pp. 624–632, Feb 2016.
- [42] M. Fu, C. Ma, and X. Zhu, “A cascaded boostbuck converter for high-efficiency wireless power transfer systems,” *IEEE Transactions on Industrial Informatics*, vol. 10, pp. 1972–1980, Aug 2014.
- [43] J. Lee, Y. S. Lim, W. J. Yang, and S. O. Lim, “Wireless power transfer system adaptive to change in coil separation,” *IEEE Transactions on Antennas and Propagation*, vol. 62, pp. 889–897, Feb 2014.
- [44] P. Si, A. P. Hu, S. Malpas, and D. Budgett, “A frequency control method for regulating wireless power to implantable devices,” *IEEE Transactions on Biomedical Circuits and Systems*, vol. 2, pp. 22–29, March 2008.
- [45] R. Carta, J. Thoné, G. Gosset, G. Cogels, D. Flandre, and R. Puers, “A self-tuning inductive powering system for biomedical implants,” *Procedia Engineering*, vol. 25, no. Supplement C, pp. 1585 – 1588, 2011. EuroensorsXXV.
- [46] S. Sonkusale and Z. Luo, “A complete data and power telemetry system utilizing bpsk and lsk signaling for biomedical implants,” in *2008 30th Annual International Conference of the IEEE Engineering in Medicine and Biology Society*, pp. 3216–3219, Aug 2008.
- [47] A. K. RamRakhyani and G. Lazzi, “On the design of efficient multi-coil telemetry system for biomedical implants,” *IEEE Transactions on Biomedical Circuits and Systems*, vol. 7, pp. 11–23, Feb 2013.

APPENDIX A

LITZ WIRE POWER LOSS CALCULATION

Eddy current losses in a given strand of a conductor is given by [2],

$$P = p/2 \int_0^{r_0} \int_0^{2\pi} J J^* r d_r d_\pi$$

$$P = \frac{I^2 p}{\sqrt{2}\pi\delta d_0} \Psi_1(\psi) - \frac{2\sqrt{2}\pi p}{\delta} H^2 \Psi_2(\psi) \quad (\text{A.1})$$

where,

I amplitude of current in conductor,

$\delta = \sqrt{\frac{p}{\pi f \mu_0}}$ is skin depth,

d_0 diameter of a strand,

p copper resistivity,

$\Psi_1(\psi)$, $\Psi_2(\psi)$,

$$\Psi_1(\psi) = \frac{\text{ber}(\psi/\sqrt{2})\text{bei}'(\psi/\sqrt{2}) - \text{bei}(\psi/\sqrt{2})\text{ber}'(\psi/\sqrt{2})}{\text{ber}'(\psi/\sqrt{2}) + \text{bei}'^2(\psi/\sqrt{2})}$$

$$\Psi_2(\psi) = \frac{\text{ber}_2(\psi/\sqrt{2})\text{ber}'(\psi/\sqrt{2}) - \text{bei}_2(\psi/\sqrt{2})\text{bei}'(\psi/\sqrt{2})}{\text{ber}^2(\psi/\sqrt{2}) + \text{bei}^2(\psi/\sqrt{2})}$$

where, ber and bei are real and imaginary parts of Kelvin Function respectively,

$$\psi = \frac{d_0}{\delta}.$$

Then the density of Eddy current losses in k_{th} layer of i_{th} conductor is expressed as,

$$\frac{dP_{ij}}{dS} = \frac{\beta}{\pi r_0^2} P = \frac{I_0^2 p \beta}{2\sqrt{2}\pi^2 \delta r_0^3 \Psi_1(\psi)} - \frac{2\sqrt{2} p \beta}{\delta r_0} H^2 \Psi_2(\psi)$$

β is the packing factor, $\beta = \frac{N_0}{(d_0/d_c)^2}$, N_0 number of strands in Litz wire, d_c conductor diameter.

The total power dissipation, per unit length of the winding, is found by summing all conductor losses of each layer,

$$P = \sum_{k=1}^m \sum_{j=1}^{m'} P_{kj}$$

$$= \frac{NI^2 p}{\sqrt{2}\pi \delta N_0 d_0} (\Psi_1(\psi) - \frac{\pi^2 N_0 \beta}{24} (16m^2 - 1 + 24/\pi^2) \Psi_2(\psi)) \quad (\text{A.2})$$

where,

N number of conductors in a layer and m number of layers.

APPENDIX B

MAGNETIC FIELD CALCULATION ON COIL ITSELF

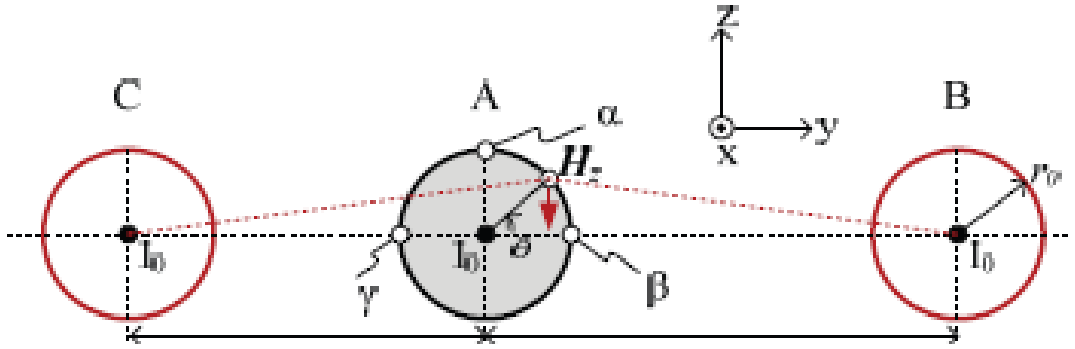


Figure B.1: Schematic diagram for the calculation of z-directed H-fields applied to target wire A by source wires B and C, I_0 is current on each wire, r_0 is conductor radius, α , β and γ are reference points [4]

Figure B.1 shows the reference points α , β and γ on a conductor to find the magnetic field on it [4]. The reference points are selected on the edges of the conductor because the magnetic field expression is used to determine proximity effect losses and these losses maximizes on edges.

H -field intensities, from the right side and left side neighbor wires respectively, are calculated as follows,

$$H_{z,right} = -\vec{z} \frac{I_0}{2\pi} \frac{p_{right} - r_0 \cos \theta}{p_{right}^2 + r_0^2 - 2p_{right}r_0 \cos \theta} \quad (\text{B.1})$$

$$H_{z,left} = \vec{z} \frac{I_0}{2\pi} \frac{p_{left} + r_0 \cos \theta}{p_{left}^2 + r_0^2 + 2p_{left}r_0 \cos \theta} \quad (\text{B.2})$$

p_{right} and p_{left} are center to center distances of the corresponding wires.

Then the magnitude of H-field intensities on reference points becomes,

$$H_{\alpha, left} = \frac{I_0}{2\pi} \frac{p_{left}}{p_{left}^2 + r_0^2} \quad (B.3)$$

$$H_{\alpha, right} = \frac{I_0}{2\pi} \frac{p_{right}}{p_{right}^2 + r_0^2} \quad (B.4)$$

$$H_{\beta} = H_{\beta, left} - H_{\beta, right} = \frac{I_0}{2\pi} \left(\frac{1}{p_{left} + r_0} - \frac{1}{p_{right} - r_0} \right) \quad (B.5)$$

$$H_{\gamma} = H_{\gamma, left} - H_{\gamma, right} = \frac{I_0}{2\pi} \left(\frac{1}{p_{left} - r_0} - \frac{1}{p_{right} + r_0} \right) \quad (B.6)$$

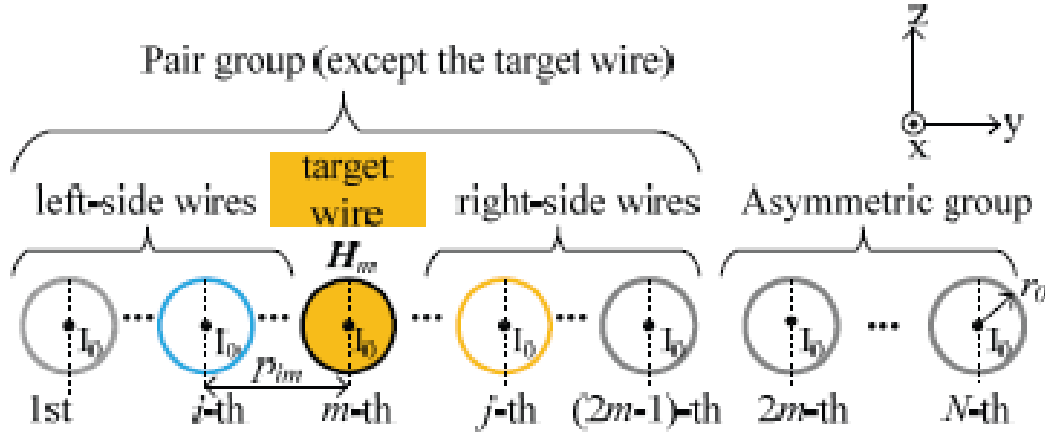


Figure B.2: Schematic of coil configuration when calculating H-fields on the m-th wire in a system of N turns [4]

If the winding is considered as two group of wires as shown in figure B.2, calculation of the magnitude of magnetic field gets easier because reference points β and γ are symmetrical in pair group. Due to the fact proximity effect is proportional with the square of H-field, H_{pair} is,

$$H_{pair} = \vec{z} \sqrt{\frac{1}{2}(H_{\beta}^2 + H_{\gamma}^2)}$$

And the H -field on the m_{th} wire due to i_{th} and j_{th} pair wires,

$$\begin{aligned}
 H_{m,pair}(i, j) &= \vec{z} H_{m,pair}(i, j) \\
 &= \vec{z} \frac{I_0}{2\pi} \sqrt{\frac{(p_{im}^2 + r_0^2)}{(p_{im}^2 - r_0^2)^2} + \frac{(p_{mj}^2 + r_0^2)}{(p_{mj}^2 - r_0^2)^2} - \frac{2(p_{im}p_{mj} - r_0^2)}{(p_{im}^2 - r_0^2)(p_{mj}^2 - r_0^2)}}} \quad (\text{B.7})
 \end{aligned}$$

H field applied to m_{th} wire from k_{th} wire can be obtained at reference point α ,

$$H_{m,asy}(k) = \vec{z} H_{m,asy} = -\vec{z} \frac{I_0}{2\pi} \frac{p_{mk}}{p_{mk}^2 + r_0^2} \quad (\text{B.8})$$

Summation of H -fields from pair and asymmetrical turns on m_{th} wire gives the overall H -field,

$$H_m = H_{m,pair} + H_{m,asy} = \vec{z} H_m \quad (\text{B.9})$$

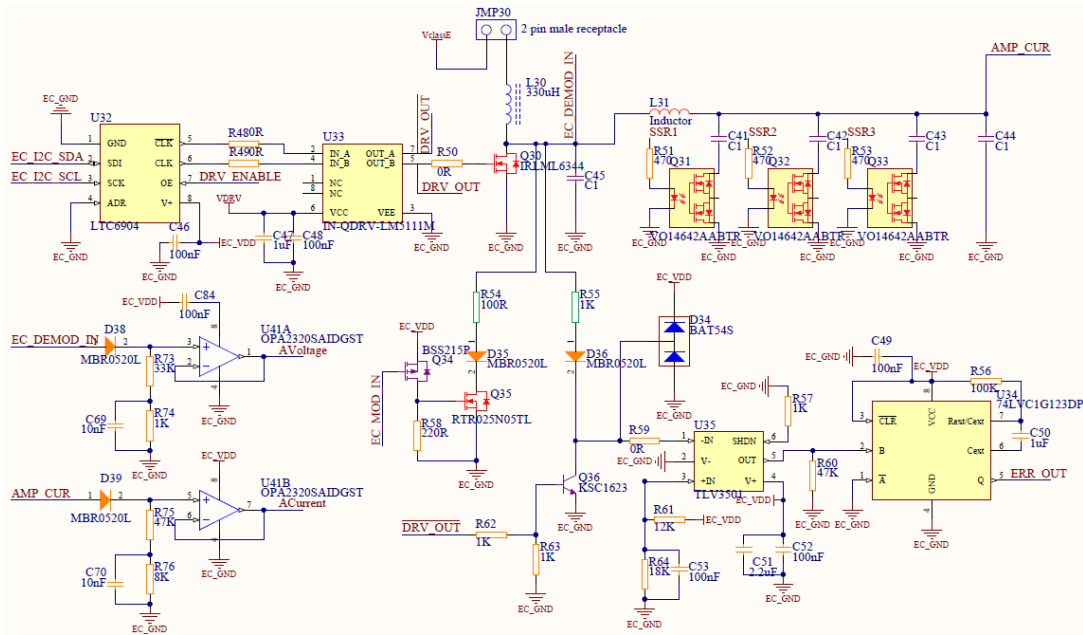


Figure C.2: External Charger Device: Schematic of ClassE Power Amplifier

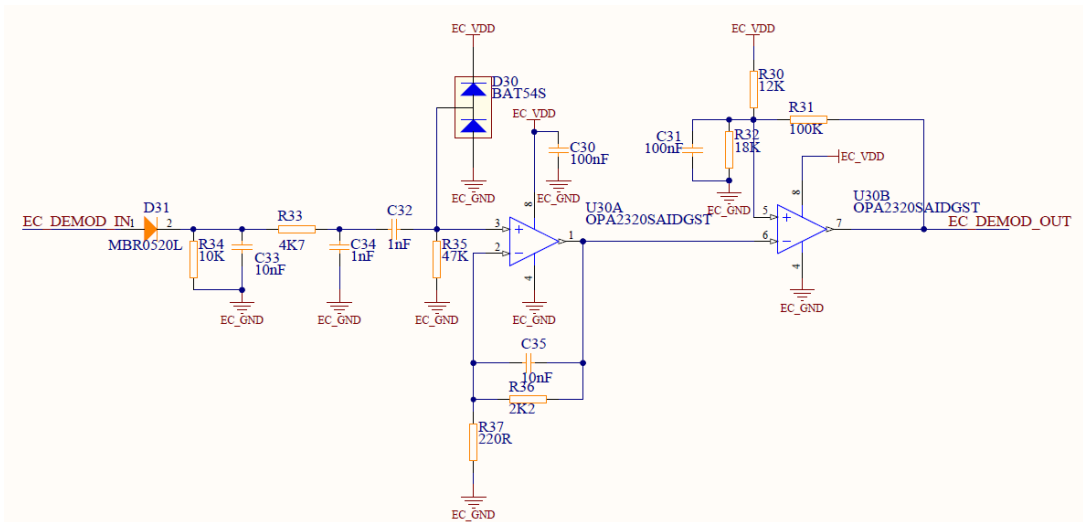


Figure C.3: External Charger Device: Schematic of Demodulator Circuit

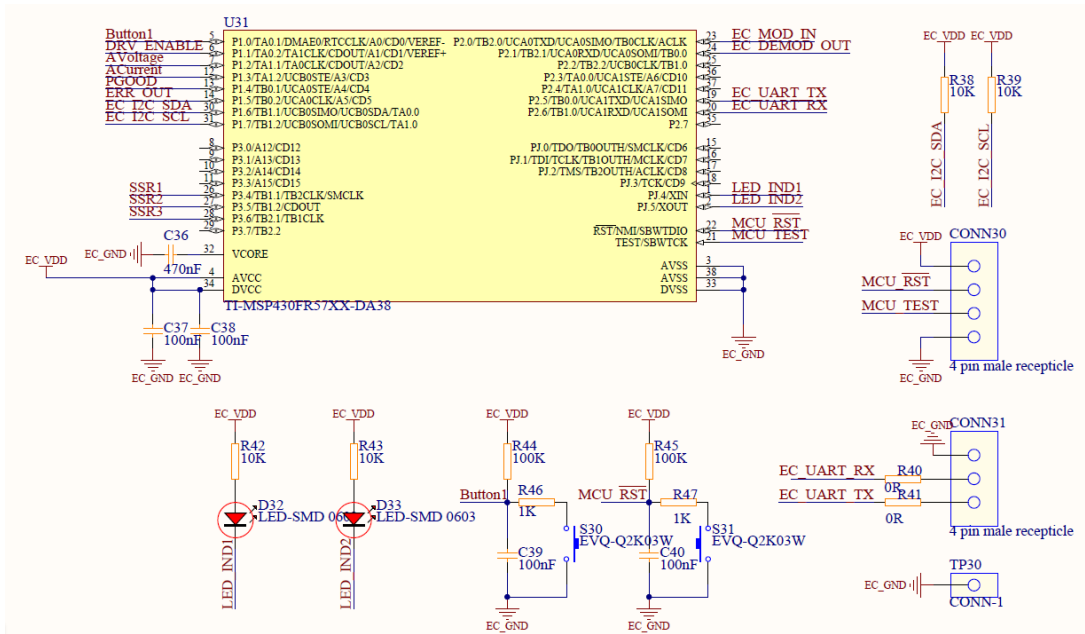


Figure C.4: External Charger Device: Schematic of MCU and User Interface

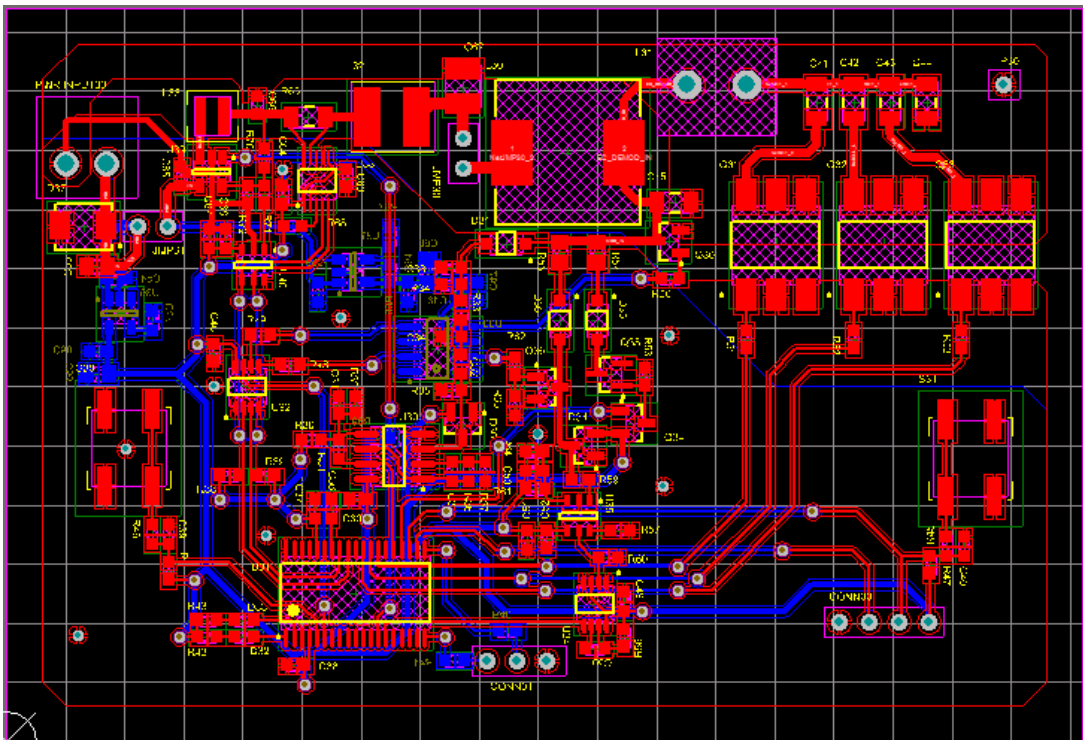


Figure C.5: PCB layout of the external charger

APPENDIX D

IMPLANTABLE MEDICAL DEVICE SCHEMATICS

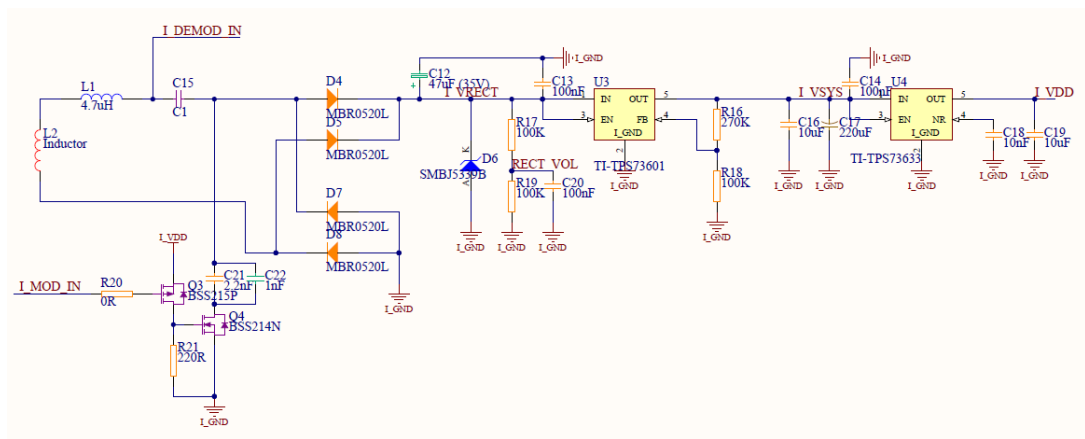


Figure D.1: Implantable Medical Device: Schematic of Power Harvester and Modulator

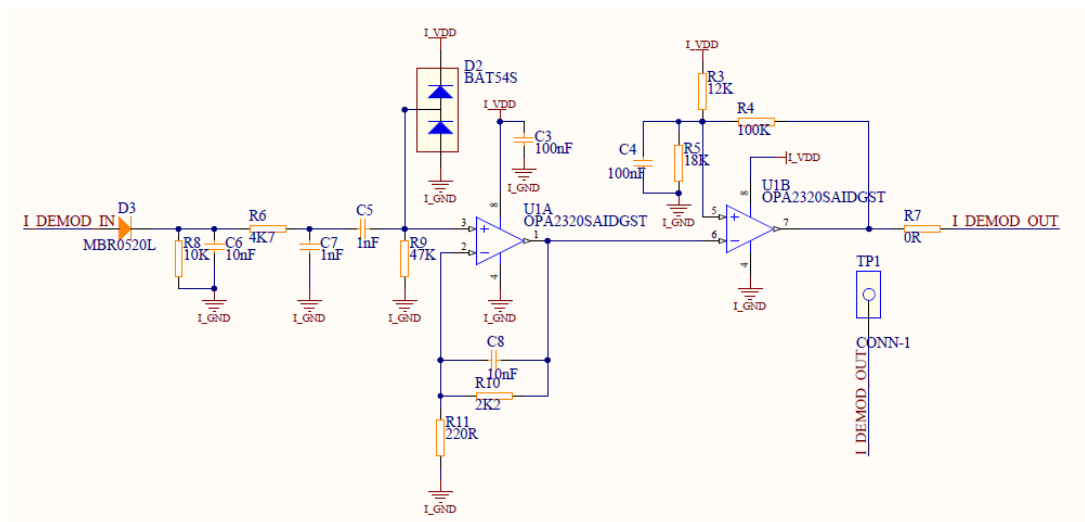


Figure D.2: Implantable Medical Device: Schematic of Demodulator Circuit

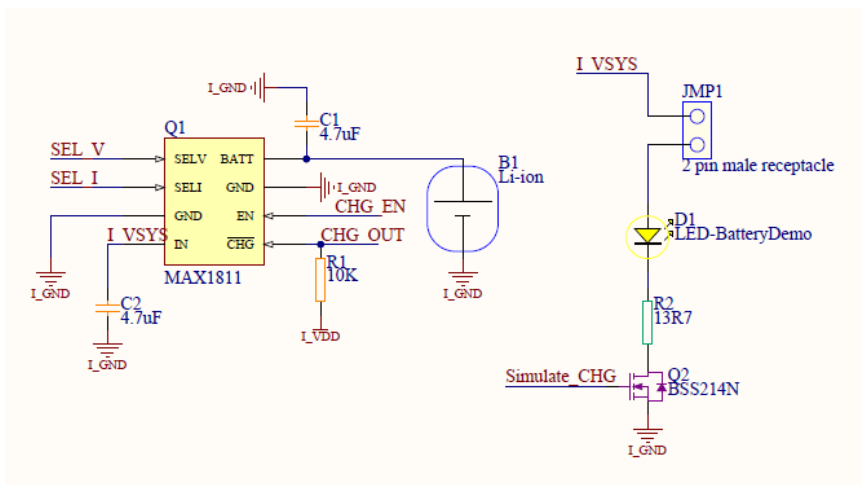


Figure D.3: Implantable Medical Device: Schematic of Battery Charger and LED Simulator

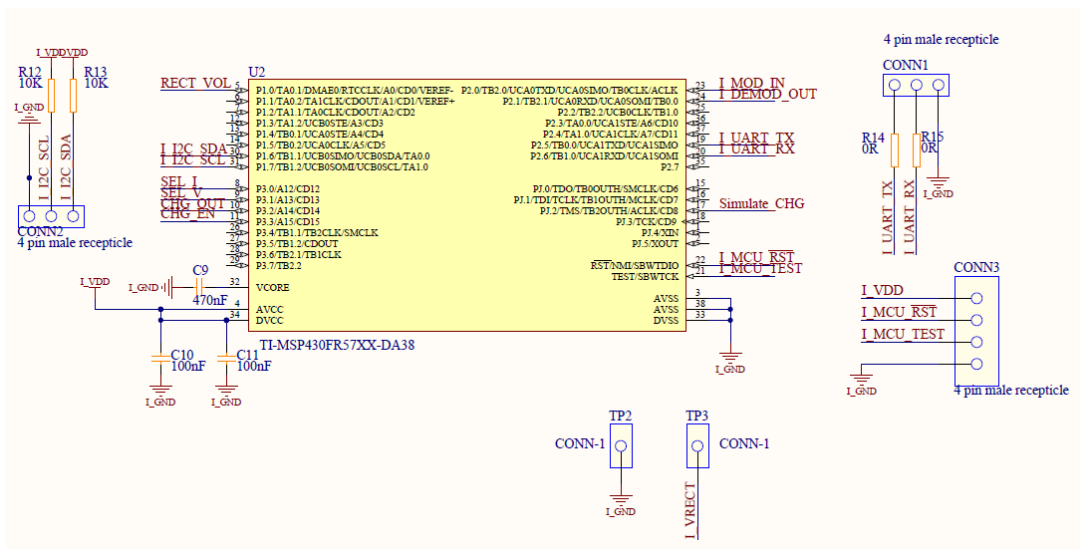


Figure D.4: Implantable Medical Device: Schematic of MCU

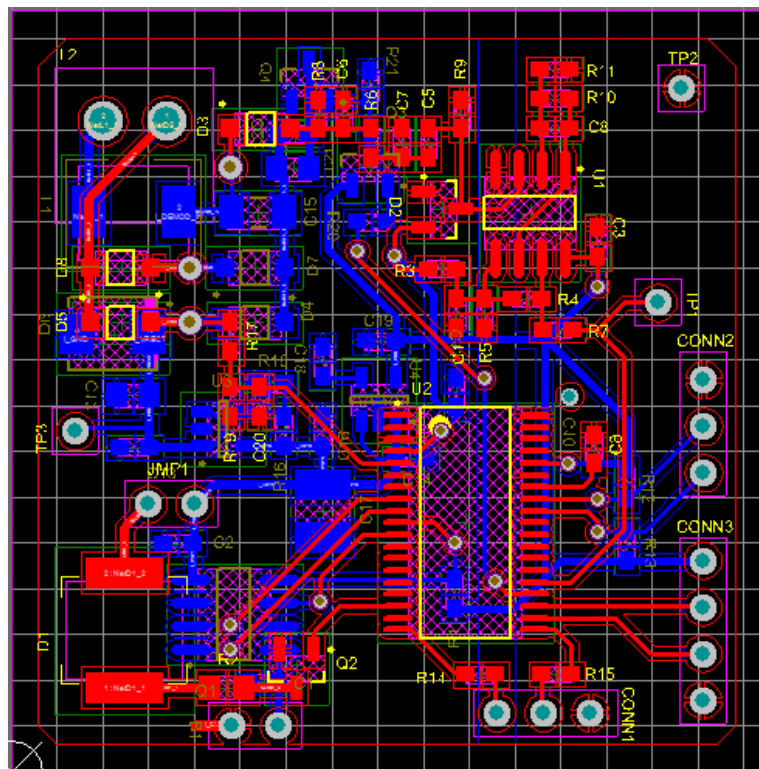


Figure D.5: PCB layout of implantable medical device